Stony Brook University

Stabilization and transformation of amorphous calcium carbonate: structural and kinetic studies

A Dissertation Presented

by

Millicent Promise Schmidt

to

The Graduate School

in Partial Fulfillment of the

Requirements

for the Degree of

Doctor of Philosophy

in

Geosciences

Stony Brook University

December 2014

Stony Brook University
The Graduate School

Millicent Promise Schmidt

We, the dissertation committee for the above candidate for the
Doctor of Philosophy degree, hereby recommend
acceptance of this dissertation.

Richard J. Reeder – Dissertation Advisor
Professor of Geosciences

Brian L. Phillips - Chairperson of Defense
Professor of Geosciences

John B. Parise
Distinguished Professor of Geosciences

E. Troy Rasbury
Associate Professor of Geosciences

Frederick Marc Michel
Assistant Professor of Geosciences at Virginia Tech

This dissertation is accepted by the Graduate School

Charles Taber
Dean of the Graduate School

Abstract of the Dissertation

Stabilization and transformation of amorphous calcium carbonate: structural and kinetic studies

by

Millicent Promise Schmidt
Doctor of Philosophy
in
Geosciences

Stony Brook University
2014

Amorphous calcium carbonate (ACC) is a common transient precursor in the formation of more stable crystalline calcium carbonate minerals, most notably calcite, vaterite, and aragonite. Formation of ACC from calcium carbonate rich aqueous solution rather than direct crystallization of crystalline polymorphs by organisms provides several advantages: control of morphology, grain size, orientation, hardness, and other bulk properties as well as reduction of energy costs during growth cycles. Despite decades of study, stabilization and transformation mechanisms of synthetic and biogenic ACC remain unclear. In particular, the roles of H_2O and inorganic phosphate in ACC structure and transformation, and the variables affecting transformation kinetics and polymorph selection are understudied.

In this research, we addressed structure and kinetic behavior of ACC through four complementary investigations: two studies focus on synthetic ACC stabilization and two focus on synthetic and biogenic ACC transformation behavior in solution at ambient temperatures. We explored ACC stabilization via compositional and thermal analyses, X-ray scattering, X-ray absorption spectroscopy, and nuclear magnetic resonance spectroscopy. Transformation experiments used a novel method of in situ structural analysis that provided quantitative kinetic and structural data and allowed us to visualize the ACC transformation pathway.

Results revealed the complexity of H_2O structure in ACC samples synthesized from three methods, indicating that the distinct hydrous populations produced define ACC behavior. Transformation kinetics and polymorph selection were strongly affected by the hydration state and type of synthetic ACC reacted. In situ transformation experiments also showed differences in kinetic behavior due to reaction medium. The structural role of hydrous components was again evident in in situ transformation experiments for ACC from a biogenic lobster gastrolith (LG) reacted with water. LG exhibited distinctly different behavior than synthetic ACC samples; LG transformation rates were significantly slower and a larger ACC fraction remained at comparable time points. Inorganic phosphate stabilizes ACC, increasing its resistance to crystallization. This research is underpinned by the relationship between microscopic structural features and macroscopic properties and behavior. Manipulation of molecular-scale variables for controlling macroscopic properties allows important applications in materials science and engineering, and a greater understanding of biominerals may guide our design of functional materials.

Dedication Page

This work is dedicated to my family: Peabean, Coffee Bean, and little Pumpkin Seed. Y'all make everything possible and worthwhile.

Table of Contents

List of Figures

List of Supporting Information Figures

List of Tables

List of Supporting Information Tables

List of Abbreviations

Amorphous calcium carbonate—ACC
Amorphous calcium phosphate—ACP
Aragonite—AR
Calcite—Cc
Differential scanning calorimetry—DSC
Hydroxyapatite—HAP
Infrared—IR
Linear Combination Fitting—LCF
Monohydrocalcite—MHC
Octacalcium phosphate—OCP
Pair distribution function—PDF
Phosphate-doped ACC and carbonate doped ACP—PACC series
Principal Component Analysis—PCA
Thermogravimetric analysis—TGA
Vaterite—Vat
X-ray absorption spectroscopy—XAS
X-ray diffraction—XRD

Acknowledgments

A special thanks to the beamline scientists that were fundamental to our experiments: Syed Khalid at X-19A at Brookhaven National Laboratory's National Synchrotron Light Source and Kevin Beyer, Karena Chapman, and Pete Chupas 11-ID-B at Argonne National Laboratory's Advanced Photon Source. Thanks also to the John Martin Group at the University of Florida for phosphate analysis.

Chapter 1: Introduction

1.1 The solid calcium carbonate system

The calcium carbonate system includes calcite, aragonite, and vaterite crystalline anhydrous varieties and monhohydrocalcite, ikaite, and amorphous calcium carbonate (ACC) hydrated varieties.[1] Ikaite is a rare occurrence crystalline hexahydrate, and monohydrocalcite is a crystalline monohydrate.[2] ACC is considered a single polymorph by some, but because ACC is formed in a variety of environments and organisms, it comprises a whole series of compositions from anhydrous to ~1.2 $H_2O/CaCO_3$ with an array of inorganic and organic constituents sometimes called polyamorphism. [1, 3, 4]

1.1.1 Biogenic ACC

Amorphous precursors to crystalline materials exist in other mineral systems as well.[5-8] Many organisms employ amorphous silica for structural purposes. Amorphous calcium phosphate (ACP) is a known precursor to hydroxyapatite in vitro, though its employment in the development of vertebrate bone is debated.[9, 10] Amorphous precursors provide a non-classical pathway to crystallization and serve to reduce energy costs to the organism, taking advantage of ACC metastability and properties that control the eventual crystalline character.[5, 6] ACC is commonly formed in a diverse array of organisms from plants to earthworms to marine invertebrates.[1, 11-17] In early studies, biogenic ACC was often categorized as either stable or transient referring to the persistence of ACC in the life of the organism. These names are misnomers, however; ACC is always metastable. The so-called "stable" ACC refers to occurrences that persist throughout the life of the organism while "transient" ACC refers to samples that serve a short-term purpose as either a precursor to crystalline polymorphs or as temporary calcium storage.[1, 5-7] Plant cystoliths are an example of ACC where the mineral phase is used to aid in light scatter within leaves and persists for relatively long periods.[18] Sea urchin larval spicules form precursor ACC before crystallization to calcite.[19, 20] Lobsters and crayfish construct calcium storage compartments called gastroliths as part of their molt cycles.[15, 21] The diversity of biogenic ACC function leads to a similar diversity in composition. ACC hydrous compositions range from 0 to 1.2 moles H_2O/mole $CaCO_3$.[20-24] As seen by Politi et al., ACC can coexist metastably with crystalline polymorphs, even directly adjacent at scales less than 10 nm.[19]

Reeder et al. analyzed biogenic ACC from lobster gastrolith (LG) using X-ray adsorption spectroscopy, X-ray scattering, nuclear magnetic resonance (NMR) spectroscopy, and thermal analysis techniques. Two hydrous components were identified via NMR spectroscopy, restrictedly mobile and rigid structural H_2O. Overall H_2O contents of LG ACC samples were lower than synthetic ACC samples, ranging from 1.0–1.2 $H_2O/CaCO_3$. Calculation of the pair distribution function from total scattering data revealed pair correlations up to a distance of ~10 Å, indicating LG ACC contains only short and some intermediate range structure. PDF structure for LG and synthetic ACC revealed no significant differences.[21]

1.1.2 Synthetic ACC

There are a number of techniques that can be used to synthesize ACC in vitro. The most common methods employ high concentration aqueous solutions (with sodium carbonate or dimethyl carbonate used as carbonate source) mixed at standard temperature and pressure.[25, 26] Syntheses at different pH values produce ACC samples with distinct thermal behaviors. Koga et al. synthesized ACC samples from pH 11.2 to 13.5 and found that crystallization temperatures increase with increasing pH.[25] Diffusion of CO_2 through calcium solutions is another method,

more common in the fabrication of ACC thin films.[27, 28] In an effort to mimic various aspects of biogenic ACC, in vitro experiments utilize synthetic ACC samples with a wide variety of compositions. H_2O contents for synthetic ACC generally vary from 0.3–1.6 $H_2O/CaCO_3$.[24, 29] Inorganic and organic additives in synthetic ACC are discussed in the next section.

Synthetic ACC structure has been examined with a wide array of X-ray, spectroscopic, and modeling techniques.[29-33] Michel et al. found that the structure of synthetic, undoped ACC lacks pair correlations beyond 15 Å, the hydrous component is dominated by rigid structural H_2O, and ACC is structurally distinct from crystalline calcium carbonate polymorphs. From the PDF experimental data of Michel et al., Goodwin et al. used reverse Monte Carlo simulations to propose that ACC contains a porous calcium rich framework with H_2O and carbonate containing channels.[30] Their results also suggest that calcium packing densities are similar to those of the crystalline calcium carbonates despite the lack of long range order.[30]

Some researchers have concluded that structural features within ACC samples are reminiscent of crystalline polymorphs, implying that ACC structural information could be used to predict polymorph selection. Gebauer et al. first identified stable prenucleation clusters of ACC in solution and used that to propose a non-classical model for ACC formation.[34] In a later study, Gebauer et al. used NMR to structurally distinguish proto-vaterite and proto-calcite ACC samples.[35] The calcium packing density results of Goodwin et al. could be interpreted in a similar light. However, proto-structural features are difficult to identify and are not evident in all ACC samples. Examining Sr-labeled sea urchin embryos from formation of ACC through crystallization, Tester et al. observed no evidence of proto-structural features, though the X-ray absorption spectroscopy methods they used would be ideal for identifying such short-range structures.[36] This dissertation does not delve into the ACC formation process, but we do use techniques to explore the short and intermediate range ACC structure for proto-crystalline features.

1.2 ACC stabilization

In the ACC literature, stabilization is often related to an ACC sample's resistance to crystallization, particularly compared to the relatively quick transformation of undoped ACC synthesized from aqueous solutions.[25, 26] [1] Identifying the stabilization mechanisms in biogenic ACC is complicated by compositional variation and the occasional use of substrates. In this discussion of stabilization, stabilization-promoting additives are generally grouped into four categories: inorganic additives (e.g., magnesium and phosphate), organic macromolecules (OMs), template/substrate directed ACC formation, and H_2O as structural component and transformation mediator.

1.2.1 Inorganic additives

Magnesium and phosphate are the two most commonly identified inorganic minor components of biogenic ACC[1, 11, 18, 21, 22, 37, 38] and the most common inorganic dopants in synthetic studies.[2, 39-44] Molecular dynamics (MD) study results suggest Mg promotes the formation of vaterite-like ACC local structure.[45] Using calorimetry and X-ray total scattering to look at the energetics and structure of a series of Mg-doped ACC samples, Radha et al. found that the samples were a continuous compositional series rather than mixtures of ACC and amorphous magnesium carbonate.[41] Despite its inclusion in a myriad of biogenic ACC samples,[1] phosphate is poorly studied. Examination of the distribution of amorphous, crystalline, and matrix materials in lobster cuticle at ambient and elevated temperatures led Al-Sawalmih et al. to

conclude that phosphorus rather than magnesium or OMs was the primary stabilizing agent in the amorphous components of lobster cuticle.[39] Sugiura et al. explored phosphate as both a dopant and a constituent of the transformation medium.[44] They concluded increasing phosphate concentration in synthesis solutions caused an exponential increase in the overall time to ACC nucleation (from solution mixing), but a variable affect on the phase transformation from ACC to vaterite.[44] In order to understand the mechanism(s) behind inorganic phosphate stabilization, we must first understand its affects on ACC structure, which is lacking.

1.2.2 Organic additives

Biogenic ACC samples contain a wide variety of OMs that are either structurally incorporated or used as matrix material. Some OMs utilized in organisms have been characterized, but full characterization is lacking.[46-50] The functions of each identified OM are also not well understood. Use of OMs as matrix material is often associated with orientational controls on ACC transformation products.[51, 52] There is also a large array of OMs explored in the synthetic ACC literature, which vary in size, functional groups, and effects on ACC.[53-66]

1.2.3 Substrates and templates

Though this dissertation does not investigate the use of substrates or templates, they are a common means of stabilizing ACC.[27, 28, 67-75]

1.2.4 H_2O

While H_2O is commonly characterized as a key component in ACC structure, experimental investigation of its roles is lacking. Hydrogen's small X-ray cross-section and low binding energy, make common structural techniques like X-ray scattering and absorption spectroscopy difficult to apply directly. Thermal analysis is the most widely used technique to provide information about H_2O content,[24, 76, 77]. However, TGA analysis alone cannot distinguish different types of hydrous components nor can it shed light on the crucial structural role of H_2O components. In situ Raman spectroscopy of thermally dehydrated calcium carbonates was used to distinguish ACC and ACP, but H_2O components were not resolved.[16] Other experimental evidence for anhydrous ACC intermediates in the transformation pathway of hydrous ACC have been proposed based on X-ray photoelectron emission spectromicroscopy and changes to ordering observed with X-ray scattering, but this is not conclusive.[78, 79]

After TGA, MD studies and NMR are the most common approaches to explore H_2O. In MD simulations exploring the combined effects of Mg^{2+} and H_2O, Tomono et al. determined that a small fraction of H_2O did not affect development of ACC local structure while Mg^{2+} hindered development.[45] Simulated higher fractions of H_2O correlated to promotion of monohydrocalcite-like local structure.[45] Saharay et al. conducted two MD studies on the effects of ACC dehydration finding that increased dehydration facilitated the formation of vaterite from orientational ordering within ACC.[80, 81] They concluded that these results supported experimental findings where vaterite appears as an intermediate phase before calcite or aragonite (this idea will be discussed further in the next section).[80] In their previous study, Saharay et al. investigated changes to local and intermediate structure with ACC dehydration and observed shifts in interatomic distances from loss of bonds between H_2O and Ca and C in the ACC structure.[81] Raiteri and Gale also used dynamical simulation to suggest that H_2O hydration spheres around forming ACC allow for a non-classical pathway to the crystalline calcium carbonates.[82] This indicates the other vital role of H_2O in ACC, as a formation and transformation medium. As

opposed to other solvents like ethanol, water tends to accelerate ACC transformation.[77, 83, 84] HNMR and ^{13}CNMR spectroscopy were used by Reeder et al. to identify the hydrous components in LG ACC.[21] These techniques also provide relative hydrous component fractions and their successful application in this study addresses a critical gap in our understanding of H_2O structure.

1.2.5 Roles of additives

Synergistic or competing effects of dopants are likely so naturally, there is some overlap of these four categories. For example, Xiao et al. and Wang et al. both showed organic macromolecules affect the uptake of inorganic magnesium and ultimately control crystalline polymorphism.[85-87] Similarly, in biogenic ACC, Raz et al. showed that Mg and organic macromolecules influence stabilization and transformation products in vivo.[20] There are also a few other methods known to stabilize ACC that defy categorization. Freeze drying has been shown to produce ACC that is stable in the atmosphere for up to 6 weeks.[76] Stephens et al. examined the role of volumetric confinement relevant for mineralization in vivo as a means of stabilizing ACC.[88] Synthesis methods using non-aqueous solutions have also been shown to produce relatively stable ACC samples.[89, 90]

Additives in ACC formation and transformation have multiple routes of action on ACC stabilization.[91] Xiao et al. categorized additive influence as acting on either the nucleation phase or the transformation phase. Synthesizing a series of ACC samples with Mg and OMs with various functional groups, they found that crystallization could be driven to selected polymorphs by addition of different OM functional groups in the nucleation rather than transformation phase.[85] Because biogenic environments containing ACC vary, the differences between additive effects in solution-mediated versus solid-state transformations must also be addressed in the discussion of stabilization mechanisms. Ihli et al. found that larger additives like poly(aspartic acid) correlate with accelerated crystallization in the solid state and retarded crystallization in solution. Whereas, smaller ions like magnesium and sulfate were shown to retard crystallization in both solid-state and solution-mediated transformations.[76] In this research, we explore the effects of dopants during the synthesis phase of ACC and the effects of the reaction medium composition on ACC transformation.

1.3 ACC transformation and kinetics

Likely related to its polyamorphism, ACC can transform to crystalline calcium carbonate via multiple pathways. Transformation kinetics vary significantly depending on environmental conditions, ACC properties, and transformation medium. ACC transformation is investigated either in the original synthesis solution[79, 92-94] or from a filtered/dried sample.[12, 78] The first method may have some biological relevance; the microenvironments in which ACC samples are formed may be maintained for transformation, but the exact fluid compositions and conditions in vivo are not well constrained. The second method isolates the effects of single variables on transformation, such as temperature[24, 83, 93, 95] or transformation environment/medium.[12, 79, 85, 96-100] ACC thin films have been investigated by both methods.[68, 94, 101, 102]

Several researchers have proposed that hydrated synthetic and biogenic ACC transforms to anhydrous ACC prior to crystallization.[19, 24, 79, 93] Radha et al. based this conclusion on calorimetric data of synthetic and biogenic ACC determining the energetic landscape for the calcium carbonate system with respect to calcite. Rodriguez-Blanco et al. conducted X-ray diffraction and electron microscopy experiments on ACC nucleated and transformed in the

synthesis solution and concluded that changes in ordering and the necessary dehydration step from hydrated ACC to anhydrous calcium carbonate indicated the presence of an anhydrous ACC intermediate.[93] However, conclusive physical evidence for an anhydrous intermediate is lacking. Rodriguez-Blanco et al. also determined that vaterite was a "fundamental" intermediate in the ACC transformation pathway to calcite.[93] Bots et al. came to similar conclusions based on small and wide angle X-ray scattering.[79] Using X-ray photoelectron emission spectromicroscopy, Politi et al. concluded that the sea urchin spicule followed a hydrated ACC → anhydrous ACC → calcite transformation pathway.[19] More exploration of possible anhydrous intermediates is necessary, but other ACC transformation studies (from the synthesis solution and dry ACC) have revealed direct transformation to crystalline calcium carbonates. Xu et al. identified two mechanisms of ACC transformation with no evidence of intermediate ACC components formed in the transformation to calcite. Using X-ray diffraction, IR spectroscopy, SEM, and atomic force microscopy, they found that they could select a solid-solid transformation or a dissolution/recrystallization mechanism by controlling the humidity of the transformation environment.[68] Using FTIR spectroscopy and X-ray diffraction, Shen et al. found ACC transformed to vaterite with subsequent transformation to calcite.[71] No single pathway appears to define ACC transformation. The key to understanding the transformation pathway is understanding the variables that manipulate it.

1.4 Applications and uses of ACC

The great variation in ACC transformation behavior and macroscopic properties that can be manipulated in the synthesis stage gives ACC enormous potential for use in materials science, geoscience, and medicine. The huge reservoir of geologic and marine carbonates belies their environmental importance, sequestering a large fraction of CO_2.[34] Some industrial interest in ACC stems from scale formations related to materials synthesis and production. Interest in CO_2 sequestration in saline aquifers has generated interest in the potential amorphous precipitates that could nucleate in pore spaces or on the mineral surfaces of reservoir rocks.[103] Comparing the solubility and bioavailability of ACC to crystalline calcite, Merion et al. found that ACC was both more soluble and correlated with a greater Ca^{2+} bioavailability and retention in an animal study.[104] ACP is widely used in medical and dental applications from coatings on implant surfaces that promote bone regeneration to additives in toothpaste to slow and prevent cavity formation.[105-110] All of these applications and the research presented here are underpinned by the relationship between microscopic structural features with macroscopic properties and behavior. Manipulation of variables on small scales for macroscopic property control holds important applications in materials science and biomedical engineering, and our understanding of biominerals may act as a guide for design.

1.5 Outline of this thesis

Each of these areas of ACC research raise new, intriguing questions. Though there is overlap, researchers tend to focus on three different aspects of ACC: (1) formation, (2) stabilization, and (3) transformation. In formation studies, researchers have focused on synthesis solution composition, pH, and pressure/temperature variables and their effects on the properties of the ACC produced. This is central to the discussion of ACC polyamorphism. At the edge of our understanding from a formational aspect is the role of proto-structural features like those proposed by Gebauer et al. and refuted by Tester et al. Can the ultimate ACC transformation product(s) be predicted from short range structural features in the ACC? In ACC stabilization

studies, researchers have focused primarily on composition by way of additives, and synthesis techniques such as variation of the carbonate source or solvent. Compositional variables like OM, inorganic Mg and P, and H_2O content have some known effects on a whole range of variables from morphology to resistance to transformation, but there are many unanswered questions. How are additives structurally incorporated, and what is their structural function? While many researchers agree that H_2O plays a key role in ACC stabilization and transformation, it is significantly understudied, partly due to some difficulty characterizing H_2O with common X-ray scattering and spectroscopic methods. What is the role of H_2O in ACC structure? ACC transformation experiments sometimes combine formation and transformation into single experiments like those of Radha et al., Bots et al., and Rodriguez-Blanco et al. where transformations occur in the original synthesis solution. But overall, transformation research focuses on questions relating to pathway. Does ACC change structurally before transformation occurs? What variables determine the pathways possible? And what variables play key roles in determining transformation kinetics and polymorph selection?

The purpose of this research is to explore the stabilization and transformation mechanisms of both synthetic and biogenic ACC samples using quantitative structural and kinetic techniques. This dissertation consists of 5 chapters (including this introduction) with chapters 2 through 5 each written as an article for publication. Chapter 2 was published in *Crystal Growth & Design* in 2014. The chapters address either synthetic or biogenic ACC and focus on structure/composition relationships or time-resolved analysis of structure over the course of ACC transformation.

Chapter 2 describes the structural role of H_2O in synthetic ACC using X-ray total scattering, nuclear magnetic resonance, and thermal analysis techniques. Combining local and intermediate structural information with dehydration behavior allowed us to characterize the hydrous components in three synthetic ACC samples with varying starting hydration states. Partially dehydrated ACC samples were also analyzed and results showed that synthetic ACC samples contain 4 hydrous components that are lost at different rates upon dehydration by heating. Structural analyses of vacuum dehydrated ACC samples reveal the same trends, implying that these results are also relevant to ambient temperature transformations.

Chapter 3 investigates the transformation pathway of hydrated and partially dehydrated synthetic ACC samples reacted with DI water and calcite-equilibrated solution. In situ structural analysis of transforming ACC allowed us to examine ACC crystallization in real time. Transformation of the three ACC types revealed variations in both polymorph selection and kinetics. In experiments with crystallization of calcite and vaterite products, both phases formed simultaneously. Partial dehydration and substitution of calcite-equilibrated solution for the DI water reacting fluid slightly slowed overall transformation rates and preserved a larger fraction of the amorphous phase at comparable time points.

Chapter 4 explores the transformation of fresh and partially dehydrated lobster gastrolith ACC in DI water at ambient temperature. Similar to synthetic transformation experiments, in situ structural analyses provide a quantitative look at transformation kinetics and polymorph selection. Partial dehydration of LG ACC prior to transformation resulted in differing results depending on the degree of partial dehydration, indicating that hydration state alone has a strong influence on transformation pathway. Similar to the three synthetic ACC types analyzed in chapter 2, LG ACC also exhibits kinetic hindrance to H_2O loss, though LG ACC is know to have only two hydrous components.

Finally, this thesis concludes with Chapter 5, which addresses the structural incorporation of phosphate into a series of ACC samples by combining compositional analysis with X-ray total scattering and thermal analysis techniques. Results show that phosphate is incorporated into the ACC structure (and conversely, carbonate is incorporated into ACP structure) rather than the syntheses producing a series of ACC/ACP mixtures. Phosphate incorporation affects transformation behavior at ambient and elevated temperature conditions. Increasing phosphate content is correlated with increased crystallization temperatures and a resistance to transformation under high humidity, ambient temperature conditions (compared to un-doped ACC). There is also evidence that some differences in H_2O incorporation occur in conjunction with changing phosphate content, reemphasizing the key role of H_2O in ACC.

In summary, this thesis sheds light on the key roles of H_2O in the stabilization of synthetic and biogenic ACC structure as well as a transformation medium. Further analysis of ACC stabilization in vitro is explored through phosphorus incorporation into ACC structure, and the exploration of carbonate incorporation into ACP structure. Structural analysis of the in situ transformation of synthetic and biogenic ACC with varying hydration state and transformation mediums allowed us to quantify transformation kinetics and variables controlling polymorph selection.

Naturally, these investigations spawned a series of new questions and pathways to explore. The dehydration studies here combined with the in situ methods of the transformation experiments broach the possibility of in situ structural analysis of dehydrating ACC. The short collection times of total scattering techniques might make it possible to observe structural changes due to dehydration in real time. Paired with thermal analyses under identical heating conditions, we could reach new understanding of dehydration behavior. The relationship between synthesis conditions and H_2O populations could be further explored with parallel thermal and NMR spectroscopic analyses of a series of ^{13}C-doped ACC samples synthesized at different pH values. The phosphate-doped ACC study leads directly to further transformation studies with samples at higher phosphate content and with other environmental conditions like higher temperatures or a water reacting medium. NMR analysis of the same phosphate-doped ACC series could also flesh out the relationship between the phosphate, carbonate, and H_2O incorporation.

Chapter 2: Structural changes upon dehydration of amorphous calcium carbonate

ABSTRACT: Amorphous calcium carbonate (ACC) is a common transient precursor to biogenic crystalline calcium carbonate, but factors controlling the amorphous to crystalline transformation remain unclear. We present a structural analysis and comparison of hydrated and partially dehydrated, synthetic ACC samples. Thermogravimetric analysis showed total H_2O losses of 46% with heating to 115 °C and 75% for heating to 150 °C. The ^1H NMR spectra of hydrous ACC, obtained both directly and indirectly, via ^{13}C-detection, contain signals from four principal hydrogen environments: translationally rigid structural H_2O, a restrictedly mobile H_2O environment, fluid-like mobile H_2O that is decoupled from rigid H and C, and hydroxyl. The retention of some restrictedly mobile H_2O and lack of change in X-ray total scattering and absorption spectroscopy data for dehydrated ACC suggest that thermal dehydration does not significantly disrupt the calcium-rich ACC framework. NMR results and thermal analysis of samples dehydrated isothermally for extended periods indicate that the H_2O loss mechanism is kinetically hindered and occurs in three stages: simultaneous loss of fluid-like mobile, restrictedly mobile, and rigid H_2O → loss of restrictedly mobile and rigid H_2O → loss of hydroxyl and trapped rigid and mobile components that cannot be removed without transformation to crystalline calcium carbonate.

1. Introduction

Amorphous calcium carbonate (ACC) is a common biomineral occurring as a transient precursor to crystalline calcium carbonate polymorphs, functioning as temporary calcium storage or as a metastable structural component persistent throughout the life of the organism. The function and composition of ACC varies among organisms and structures.[1] Studies suggest that organisms incorporate phosphate,[62] magnesium,[111] organic macromolecules,[11, 47] and structural H_2O[82] to stabilize the ACC for short and long-term use. Organisms govern ACC-derived biomineral particle morphology, grain size, orientation, composition, polymorph selection, and transformation kinetics by controlling composition and synthesis environment.[112] A better understanding of these properties and the mechanisms by which organisms control them *in vivo* is vital to manipulation of these materials for industrially useful applications.

Like biogenic ACC, synthetic ACC is metastable and known to transform into any of the three anhydrous crystalline calcium carbonate polymorphs (calcite, aragonite, and vaterite) under various *in vitro* conditions.[29, 93] H_2O plays key roles in ACC transformation both as external mediator/inducer and as part of the structure.[82,93] Compositions of 0 to 1 mole H_2O per mole $CaCO_3$ are reported for a wide range of biogenic ACC samples.[3, 16, 20, 22, 78] Reported compositions for synthetic ACC vary from 0.5 to 1.4 moles H_2O/mole $CaCO_3$.[29, 31, 113] H_2O incorporated into ACC structure has been shown to affect ACC formation, mineral stability, and the crystallization mechanism.[82] Raiteri and Gale proposed that H_2O is responsible for the non-classical mineralization pathway followed by calcium carbonates, forming an intermediate metastable hydrous ACC phase despite the greater stability of anhydrous crystalline phases. Conducting crystallization experiments in a water-dominated system has been shown to affect the transformation products and perhaps mechanism.[79, 93] Rodriguez-Blanco *et al.* and Bots *et al.* found that hydrated ACC transformed to an intermediate anhydrous ACC before forming vaterite and finally calcite.[79, 93] Radha *et al.* and Politi *et al.* concluded that the calcium carbonate transformation pathway for two different biogenic ACC samples follows the progression of hydrated ACC → anhydrous ACC → crystalline calcium carbonate polymorph(s) under different environmental conditions.[24,19] Radha *et al.* concluded that the structural changes due to

dehydration are irreversible and exothermic and that the crystallization energetics for synthetic and biogenic ACC samples are similar.

In the present study we examine the role of hydration on the behavior and properties of synthetic ACC. In order to achieve different hydration states, we employ heating of initially hydrated ACC under varied conditions. This approach is not intended to mimic biomineralization conditions, since different mechanisms may operate at elevated temperatures. Several previous studies have also used heat-treatment to induce dehydration and transformation of ACC.[2, 24, 25, 39, 43, 55, 57, 68, 70, 82, 83, 90, 95, 100] It has been noted that the temperature at transformation may have an effect on the crystallization mechanism and polymorph selection.[68, 95, 100] Ogino *et al.*, for example, investigated the properties of the crystalline transformation products of ACC to determine how polymorph selection varies with temperature and found that calcite is produced over the whole temperature range of ACC transformations while crystallization of vaterite and aragonite is limited to the low and high temperature regions, respectively.[95] Biogenic ACC that has been dehydrated via heat-treatment remains metastable, but a corresponding structural analysis of dehydrated synthetic ACC is needed for comparison.[19, 24]

The novel sample treatment techniques that we use in this study provide a unique pathway to examine the effects of hydration state on ACC structure and transformation behavior. Thermogravimetric analysis and NMR experiments provide information about the role of H_2O in the amorphous to crystalline transformation of ACC. X-ray scattering and spectroscopic techniques provide information on the short- and medium-range structure of ACC before and after dehydration. The combined information on ACC structure and transformation behavior sheds light on the ACC transformation pathway and may be applied to studies of biomineralization and industrial applications of calcium carbonates.

2. Methods

2.1 Sample Synthesis and Preparation

2.1.1 ACC Samples

Three different synthesis methods were employed to generate hydrated ACC samples for characterization. The procedures of Koga *et al.* were adapted for synthesis methods 1a and 1b.[25] For method 1a, we added 5 mL 0.5 N sodium hydroxide to 20 mL 0.02 M sodium carbonate to obtain a pH of 12.8 before adding 20 mL 0.02 M calcium chloride. For method 1b, the sodium hydroxide was omitted for a pH of 9.8, before addition of the calcium chloride solution. Both method 1 syntheses result in precipitation immediately upon addition of the Ca-bearing solution. For method 2, we followed the procedure of Faatz *et al.* and mixed 80 mL of a 0.0624 M dimethyl carbonate, 0.0125 M calcium chloride solution with 20 mL 0.5 N NaOH, yielding a pH of 12.9.[26] Upon addition of the base, precipitation of hydrated ACC occurred in 3–5 min. ACC from all synthesis methods were vacuum filtered through a 0.45 μm Nylon membrane filter, rinsed with fresh acetone to remove excess water, and allowed to dry. Filter-dried samples were ground gently and dried further under soft vacuum in the presence of desiccant for 10–20 min. Traditional Bragg X-ray diffraction (XRD; Scintag diffractometer with a Cu-Kα source, $\lambda = 1.54$ Å) was used to check phase purity and identify crystalline calcium carbonate polymorphs. ACC samples from all syntheses appear as aggregates of spheres (2–6% eccentricity) with mean diameters in the range of 75-100 nm, as determined by scanning electron microscopy (SEM).

2.1.2 Heating Procedures

Different hydration states were achieved by pre-treatment of ACC samples by heating to temperatures ranging from 85 °C to 200 °C, which fall below the crystallization temperatures of samples generated from all synthesis methods. ACC samples synthesized for total scattering experiments were heated in a convection oven under flowing air. Spectroscopy samples were heated in a muffle furnace with no flowing gasses or by using a small volume muffle furnace with flowing nitrogen; there were no observable differences amongst replicate samples dehydrated to the same temperature in different furnaces. When heated to 115 °C, ACC samples exhibited no change in grain size or eccentricity. Comparison of SEM images of hydrated versus partially dehydrated ACC samples (Figure **1**) showed no visual differences. SEM images of products from the three different ACC synthesis methods also showed no visual differences, which corroborates the SEM comparison by Koga *et al.* of synthesis methods 1a and 1b (see supporting information Figure S **1**).[25]

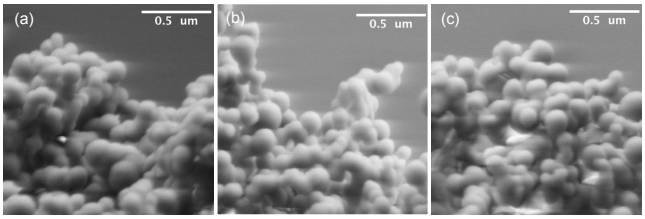

Figure 1. SEM images of ACC synthesized by method 1b: (a) fresh, hydrous form, (b) heated to 115 °C, and (c) heated to 134 °C.

2.1.3 Reference Samples

Reagent grade calcite (Spectrum Chemicals Corp.) was rinsed and dried before analysis. Vaterite was synthesized by adapting the procedures of Gebauer *et al.*.[34,35] We added 10 mL 0.4 M sodium carbonate solution to 10 mL 0.4 M calcium chloride solution and stirred for 5 min before filtering, rinsing with acetone, and drying as described in Section 2.1.1. Phase purity was confirmed with XRD.

2.2 Analytical Methods

2.2.1 NMR Methods

Two different sets of NMR experiments were performed: *ex situ* $^{13}C\{^{1}H\}$ heteronuclear correlation (HETCOR) experiments were used to obtain ^{1}H spectra indirectly through ^{13}C, and quantitative single pulse ^{1}H spectra were obtained *in situ* during sample heating. Both types of NMR experiments were performed on ACC samples prepared by synthesis method 1a whereas only directly detected single pulse ^{1}H spectra could be obtained for ACC synthesized by method 2 owing to the low natural ^{13}C abundance.

ACC 1a samples for the *ex situ* NMR experiments were partially dehydrated by heating to 85, 115, 150 or 200 °C using TGA-DSC or by storage in a vacuum (held at 3.8×10^{-2} mbar for 17 hr), and then packed into a 3.2 mm o.d. rotor and placed under a soft vacuum for 30 min before being sealed. The $^{13}C\{^{1}H\}$ HETCOR experiments were performed on a Varian Inova spectrometer with a 9.4 T magnet, operating at frequencies of 100.57 MHz and 399.89 MHz for ^{13}C and ^{1}H, respectively. A Varian/Chemagnetics T3 probe built for 3.2 mm o.d. rotors was used, with a spinning rate of 10 kHz. Pulse powers on the ^{1}H channel were set to 50 kHz for both the

initial 5 μs π/2 pulse and the 2.5 ms cross polarization (CP) pulse, with a matched, ramped B_1 field on the ^{13}C channel. A 1 s delay was used between consecutive acquisitions, with a 50 ms mixing time inserted prior to the CP pulse in the HETCOR sequence to ensure quantitative spectra were obtained (see Michel *et al.*).[29] Directly acquired ^{13}C single pulse spectra were recorded before and after each HETCOR experiment, which showed samples remained amorphous.

For *in situ* experiments on ACC 1a, fresh sample was packed in a 5 mm o.d. rotor and placed under a soft vacuum for 30 min before being capped with a vented plug. An 11.7 T Varian Infinity Plus spectrometer was used, operating at 499.8 MHz for ^1H, with a T3 Chemagnetics probe. All of the spectra were obtained at a spinning rate of 7 kHz using nitrogen gas for the bearing, drive, purge and VT gas flows into the probe. The heating profile consisted of stepped, 20 °C increases in temperature from 20 to 140 °C, and a final step to 150 °C. At each temperature, an equilibration period of 30 min passed prior to the acquisition of a ^1H single pulse spectrum with a 1 s pulse delay between acquisitions and a 4.25 μs π/2 pulse (71 kHz RF field). Scans lasting a total of 2 min (120 acquisitions) were sufficient to obtain good quality spectra.

2.2.2 Thermal Analysis

Simultaneous thermo-gravimetric analysis and differential scanning calorimetry (TGA-DSC) measurements were completed on a Netzsch STA 449C Jupiter instrument. To determine the intermediate transformation products during heating, a series of identical fresh ACC samples were analyzed using the following procedure. First, a fresh ACC sample (3 replicates total) was heated from 30–900 °C at 10 °C/min under flowing nitrogen gas in an Al_2O_3 crucible. Temperatures of interest were selected based on mass losses and reaction features in the TGA-DSC traces. After the TGA-DSC furnace cooled, a fresh sample was started using the same heating program. The program was aborted at the temperature of interest (e.g., 115 °C); the sample was removed and immediately analyzed with XRD to determine the phase(s) present. Subsequent fresh samples were heated to 150, 200, 400, 600, and 900 °C before removal and immediate XRD analysis. This procedure of interrupting the heating program for phase analysis was repeated with all synthesis methods.

To analyze the thermal behavior of partially dehydrated ACC samples in parallel to the *ex situ* NMR experiments described above, TGA-DSC experiments were designed to replicate the conditions. Here, the synthesis method 1a samples were heated to the pre-treatment temperature of interest (85, 115, 150, 185, or 200 °C) on the TGA-DSC, stored under soft vacuum in the presence of desiccant while the TGA-DSC furnace cooled (20–60 min), then placed in the TGA-DSC again and analyzed over the full temperature range (30–900 °C). The same procedure was followed for each temperature of interest with a replicate for each temperature.

Starting and intermediate H_2O compositions were determined from TGA-DSC measurements. H_2O loss was assumed to be complete by 400 °C (in the stable weight range after calcite crystallization for ACC samples from all synthesis methods). Initial H_2O compositions were calculated on a per mole basis relative to $CaCO_3$ from the measured mass loss data. Average values shown in Table **1** were calculated from N = 5, 7, and 4 replicates for synthesis methods 1a, 1b, and 2, respectively. The average relative error for mass loss is ± 8 %. Extended isothermal TGA-DSC experiments involved three heating regimes all under flowing dry nitrogen: (A) dynamic heating from 30 to the isothermal temperature (150 or 200 °C) at 10 °C/min, (B) isothermal heating at 150 or 200 °C for 10, 24, or 48 hr, and (C) a second dynamic heating from the isothermal temperature to 900 °C at 10 °C/min.

Table 1. Measured mass losses on heating and calculated average total H_2O compositions of all ACC samples before and after heating.

Synthesis Method	Crystallization Temperature, °C	Average total mass loss on heating, %						
		Temperature (°C)						
		85	115	135	150	185	200	400
1a	341	3.5	9.7	13.7	15.6	17.7	18.3	21.2
1b	202	3.1	10.2	15.1	17.2	19.3	20.8	22.5
2	376	1.9	6.2	9.5	11.0	12.8	13.5	17.7
Synthesis Method	Crystallization Temperature, °C	Average mole(s) H_2O/mole $CaCO_3$ remaining						
		Temperature (°C)						
		Initial	85	115	135	150	185	200
1a	341	1.49	1.2	0.8	0.5	0.4	0.2	0.2
1b	202	1.61	1.4	0.9	0.5	0.4	0.2	--
2	376	1.19	1.1	0.8	0.6	0.4	0.3	0.3

2.2.3 Synchrotron X-ray Total Scattering and Pair Distribution Function Analysis

High-energy X-ray total scattering data were used to obtain the pair distribution function (PDF or G(r)), which describes the average distance between atom pairs in the bulk material weighted by the atomic number of the scattering atoms.[114] Inter-atomic distances can be determined from G(r) fitting. This method is insensitive to H atoms owing to their low scattering amplitude for X-rays.

Total scattering data were collected on hydrated and partially dehydrated method 1a, 1b, and 2 ACC samples at the undulator beamline 11-ID-B at Argonne National Laboratory's Advanced Photon Source. Fresh, hydrated ACC samples were divided into two aliquots, A and B. Aliquot A was analyzed immediately while aliquot B was heated to 115 °C in a Lindberg/BlueM Mechanical Oven with flowing air. Aliquot B was then analyzed while aliquot A was heated to 150 °C. After heating, aliquot A was analyzed again. Incident X-ray energy (58 keV, λ = 0.2127 Å) was selected with a Si(311) monochromator, and scattered X-rays were detected with a Perkin Elmer amorphous silicon area detector. Sample–detector distance and detector non-orthogonality were calibrated using NIST CeO_2 standard (diffraction intensity set: 674a). The program Fit-2D was used to convert collected data from 2D to 1D, applying a polarization correction with integration.[115]

Intensity data were transformed into the experimental total scattering structure function, S(Q), the reduced experimental structure function, F(Q), and the pair distribution function, G(r), with the program PDFgetX2, where beamline-specific and standard corrections were applied.[116,117] Sample compositions used to constrain scattering data were calculated from TGA-DSC measurements (see Table **1**). The F(Q) data were truncated at 22-23 $Å^{-1}$ before Fourier transformation to obtain G(r).

2.2.4 X-ray Absorption Spectroscopy

Ca K-edge (4038 eV) X-ray absorption fine structure (XAFS) spectra were collected at the bending magnet beamline X-19A at Brookhaven National Laboratory's National Synchrotron Light Source. The first peak in the first derivative of the K-edge of a Ti metal foil was set to

4966 eV for calibration of the Si(111) double-crystal monochromator. The calibration foil was mounted between I_t and I_{ref} for calibration checks throughout beamtime. All data were collected in transmission mode with 50% detuning for harmonic rejection. Hydrated and partially dehydrated ACC samples made from synthesis methods 1a, 1b, and 2 were kept in a vacuum desiccator and analyzed <3 hr from the time of synthesis.

3. Results

3.1 Thermal Analysis

3.1.1 Thermal analysis of ACC from synthesis methods 1a, 1b, and 2 (30–900 °C)

The TGA-DSC results for ACC samples prepared by synthesis methods 1a, 1b, and 2 reveal the transformation behavior of hydrated ACC on heating to 900 °C (Figure **2**). The DSC curves show a broad endotherm in the range 50–150 °C for all three samples, a sharp exotherm at 341, 202, and 376 °C (for synthesis methods 1a, 1b, and 2, respectively), and a second broad endotherm starting at 700 °C for all samples. The TGA curves show mass loss steps associated with each of these three DSC features. The endotherm and corresponding multi-step mass loss near 100 °C are commonly identified as loss of weakly bound H_2O.[90] For samples 1a and 2, TG mass loss curves show a shallow slope until approximately 80 °C, a steep slope to 120 °C, and a second shallow slope to 260 °C, where mass loss transitions to a steady-state, nearly horizontal slope until 600 °C (well-past the reactions at 341/376 °C). The 1b TG curve exhibits the same features but on a compressed temperature scale. The two-step mass loss process before crystallization has been observed in previous studies and attributed to loss of two distinct types of H_2O: mobile and structural.[90,68] XRD analysis of all three samples was completed at four points in the experiments: (1) before TGA-DSC analysis, (2) before the sharp exotherm, (3) between the exotherm and the broad, high-temperature endotherm, and (4) after 900 °C (all XRD results shown in supporting information Figure S **2**, Figure S **3**, and Figure S **4**). All three samples were amorphous before analysis and after heating to 115 °C. Samples analyzed after the sharp exotherm were identified as calcite indicating the exothermic reaction is a crystallization process. Analysis of the final transformation products at 900 °C indicates that the endotherms centered at 800 °C result from a decarbonation reaction producing calcium oxide.

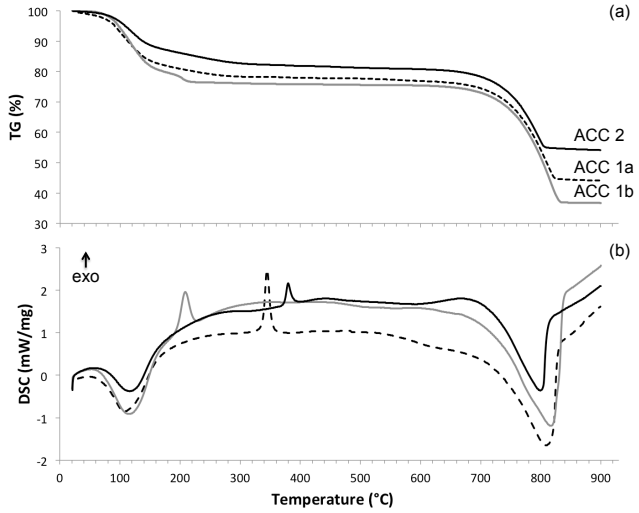

Figure 2. Comparison of synthesis method 1a, 1b, and 2 ACC samples showing (a) TGA and (b) DSC results obtained at a heating rate of 10 °C/min.

Synthesis methods 1a and 1b span the pH range of a series of ACC samples synthesized from starting solutions with different pH values. As described in Section 2.1.1, method 1a includes addition of 5 mL 0.5 N NaOH for a pH of 12.8 and method 1b involves no NaOH addition for a pH of 9.8. A series of ACC samples synthesized over a range of pH (9.8–12.8)—determined by addition of 0 to 5 mL 0.5 N NaOH—revealed a linear correlation between crystallization temperature and pH of the starting synthesis solution (Figure **3**). This trend is consistent with the findings of Koga *et al.*, who also reported that increasing the synthesis pH results in an increasingly exothermic crystallization reaction.[25] The DSC transformation peaks for intermediate pH ACC samples differ from end-member crystallization reaction peaks: ACC synthesized from pH 12.2 shows a shoulder on the high temperature side of the transformation peak, and ACC from pH 12.4 solution shows a well-defined doublet crystallization reaction. For ACC prepared by synthesis methods 1a and 1b, we observe increasingly exothermic net reactions as pH increases: 1a (pH 12.8, -8.6 kJ (mole $CaCO_3$)$^{-1}$) and 1b (pH 9.8, -5.8 kJ (mole $CaCO_3$)$^{-1}$). Calculation of the enthalpy change of crystallization is complicated by the overlap of the endothermic final dehydration step with the exothermic crystallization reaction at the heating rate studied.

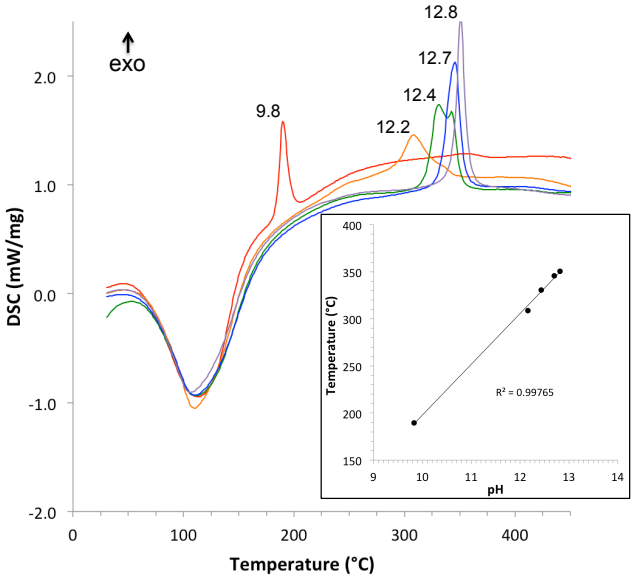

Figure 3. DSC traces of ACC samples synthesized with a range of starting pH values with end-member pH values representing synthesis method 1a (pH of 12.8) to 1b (pH of 9.8).

3.1.2 Thermal Analysis of partially dehydrated ACC from synthesis methods 1a and 2

Synthesis method 1a ACC samples were partially dehydrated by heating to different pre-treatment temperatures below the crystallization temperature (341 °C) and then analyzed for weight loss through the full heating program from 30 to 900 °C (Figure **4**). Pre-treatment temperatures, corresponding remaining H_2O contents, and total mass losses are listed in Table **1**. DSC curves show a systematically diminishing first endothermic peak with increasing pre-treatment temperature, and an endotherm minimum that shifts to higher temperature. The apparent lack of any appreciable endotherm for the three highest pre-treatment temperatures is

consistent with the absence of any observable mass loss in the corresponding TG curve over this region. With increasing pre-treatment temperature, there is an overall decrease in the measured DSC reaction enthalpy (which includes crystallization and H_2O evolution), from -8.5 to -10.5 ± 3 % kJ (mole $CaCO_3$)$^{-1}$, which may be caused by the diminishing endothermic contribution of H_2O evolution to the net exothermic crystallization reaction.

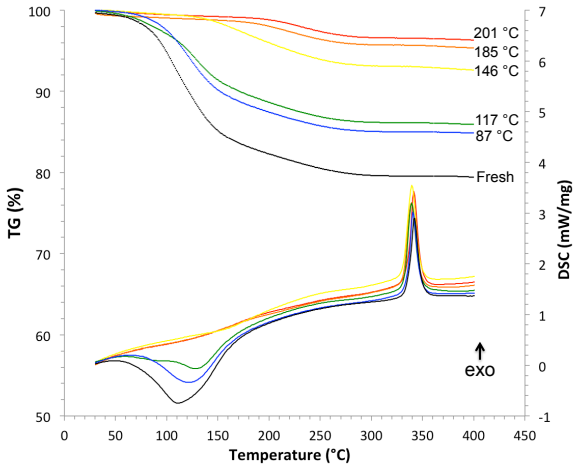

Figure 4. TGA (labeled curves, left axis) and DSC (right axis, colors match labeled TGA curves) results of synthesis method 1a samples dehydrated to a range of pre-treatment temperatures and then analyzed with a full 30–900 °C heating program at 10 °C/min.

To quantify differences in the mass loss behavior between samples (Figure **5**), three regimes were defined on the basis of their distinct mass loss slopes (see example in Figure **5**a). All samples show two distinct H_2O loss steps distinguished by different slopes of weight loss versus temperature at a constant heating rate. Several researchers have observed multi-step mass loss in both biogenic and synthetic ACC.[20,90,85,16,31] Mass losses by regime are shown in Figure **5**b; regime boundary temperatures and crystallization temperatures are plotted in Figure S **5**.

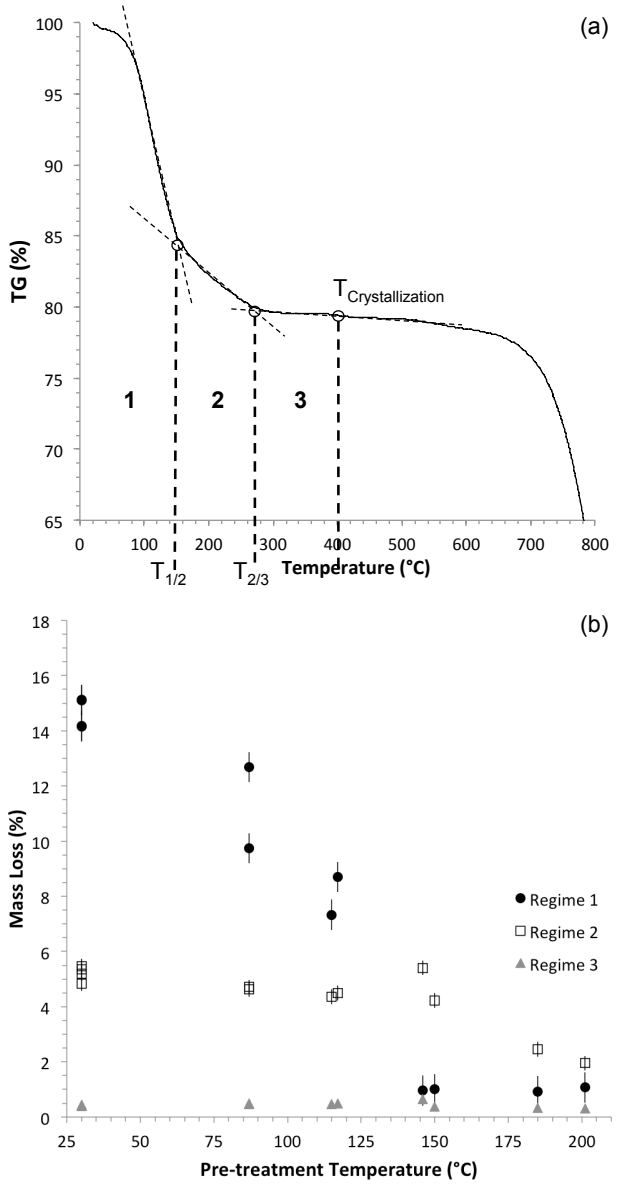

Figure 5. TGA-DSC of a series of heated ACC 1a samples showing (a) the three mass loss regimes, and (b) the regime mass loss %. Mass loss error bars represent one standard deviation of replicates, N = 4, with average relative errors of 5%.

Crystallization temperature exhibits less variation than regime boundary temperatures for replicates both of fresh, hydrated ACC samples and dehydrated samples. This suggests that the heat-induced transformation temperature is unaffected by pre-treatment heating. The regime 1/2 boundary temperature is elevated for the two highest pre-treatment temperatures, which correspond to 14–21 % mass loss or 0.4 moles of remaining H_2O/mole $CaCO_3$. Previous studies report structural and mobile H_2O species and hydroxyl groups in synthetic ACC samples.[68,29] The components that dominate the mass loss for each regime cannot be determined from TGA-DSC results alone, and we return to this point in the NMR results. Mass loss in regime 1 shows significant decreases with increasing pre-treatment temperature up to 150 °C, above which no change is observed (Figure **5**b), indicating that the bulk of regime 1 H_2O loss is complete by

150 °C. Mass losses in regime 2 are less sensitive to pre-treatment temperature (6–2 % mass loss from 30–200 °C pre-treatment temperature). Regime 3 mass loss is insensitive to pre-treatment temperature, indicating that the components(s) driven off in this regime are largely unaffected by pre-treatment.

This partial dehydration TGA-DSC experiment was repeated for synthesis method 2 ACC (Figure S **6**) revealing important differences between the two ACC samples. The DSC signature of the H_2O-loss reaction for fresh, hydrated method 2 ACC is a broad, well-defined endotherm with a minimum located at 119 °C (increasing to 162 °C for a sample heated to 150 °C). The shift is associated with a significant loss in peak area with increasing dehydration leading to a complete lack of endotherm for the sample pre-treated at 176 °C. These trends are similar to those observed for synthesis method 1a ACC except that the mass loss slopes and thermal positions of DSC features are different; for example, the H_2O-loss endotherm is absent at a lower pre-treatment temperature, 150 °C. The regime boundary temperatures for the ACC 2 experiment remain unchanged for all but the highest pre-treatment temperature in regime 2 (Figure S **5**). The TG curve for the fresh sample shows a multi-step mass loss similar to 1a ACC results, and increasing pre-treatment heating causes a progressive decrease in regime 1 mass losses and mass loss rates, again similar to the trends observed for 1a ACC. While the exact hydrous components cannot be assigned to the defined mass loss regimes as discussed for the 1a ACC experiment, the relative proportions of H_2O lost in each regime show marked differences amongst ACC samples prepared from the three synthesis methods (Table **2**).

Table 2. Relative proportions of H_2O lost in partial dehydration TGA-DSC experiments for synthesis method 1a and 2 ACC samples.

Pre-treatment Temperature (°C)	Mass Loss Fraction (% of total)					
	Regime 1		Regime 2		Regime 3	
	1a ACC	2 ACC	1a ACC	2 ACC	1a ACC	2 ACC
25	61	72	34	26	6	2
117	56	64	36	33	8	4
150	21	18	65	76	14	7
176 (1a) | 185 (2)	18	25	64	66	18	9

3.1.3 Thermal analysis of ACC samples isothermally dehydrated

To test the possibility that dehydration of ACC causes crystallization, synthetic ACC samples were dehydrated isothermally in a series of TGA-DSC experiments at 150 or 200 °C, where isothermal periods ranged from 10 to 48 hr, followed immediately by dynamic heating to 900 °C at 10 °C/min (Figure **6**). For discussion purposes, we assume all the mass change up to the crystallization reaction observed in the DSC profile is due to loss of H_2O. The TG curves were divided into three regimes, based on the temperature program and behavior of the first derivative, as follows: (A) dynamic heating from 30 ^{o}C to the isothermal temperature at 10 ^{o}C/min, (B) isothermal heating maintained at 150 or 200 ^{o}C for 10–48 hr, and (C) dynamic heating from the isothermal temperature to 900 ^{o}C at 10 ^{o}C/min. Regime A is characterized by the rapid loss of mass, including the maximum rate of mass loss (minimum in the first derivative). The division between regimes A and B represents the point at which the first derivative of the mass loss curve becomes linear and coincides with the maximum furnace temperature in the first dynamic heating segment. Regime B, characterized by isothermal

heating, extends for 10, 24, or 48 hr. Regime C, the second dynamic heating segment, immediately follows isothermal heating and extends through crystallization and eventual breakdown. TGA-DSC results from all isothermal experiments (Figure **6**) reveal differences in dehydration behavior related both to isothermal dehydration and the temperature of isothermal heating. The H_2O loss fractions by regime for each experiment are summarized in Figure **7**, showing significant differences in H_2O component release amongst the three ACC types.

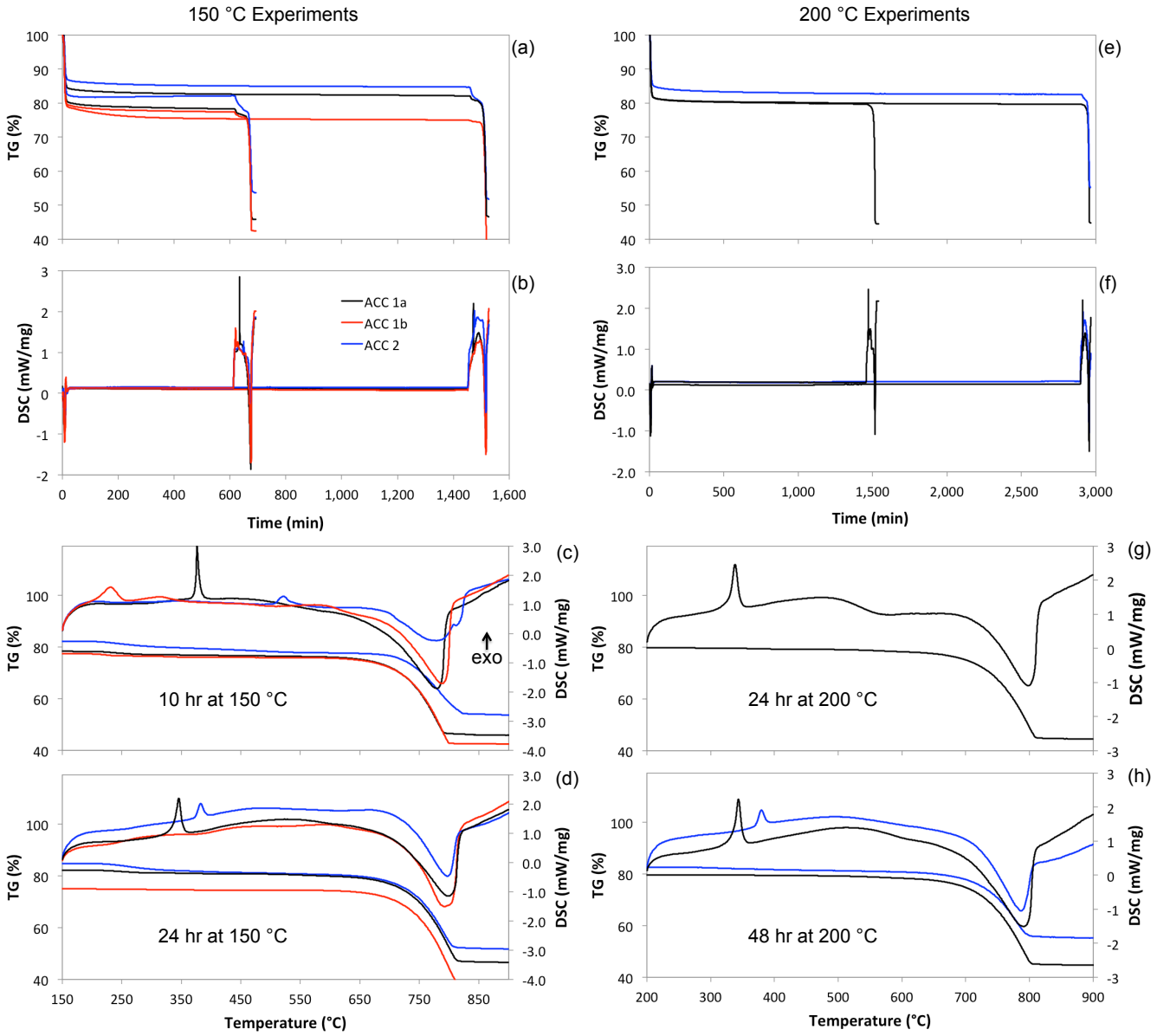

Figure 6. (a, e) TGA and (b, f) DSC results from extended isothermal experiments are shown as a function of time for isothermal heating at 150 °C (left) and 200 °C (right). Expanded views are shown as a function of temperature in (c-d) and (g-h) for specified isothermal heating durations. The inflection in all DSC curves at 12 min is an artifact caused by briefly overshooting the isothermal temperature (by 14 °C), and does not represent a transformation reaction, as determined by interrupting several experiments in the isothermal regime for XRD analysis.

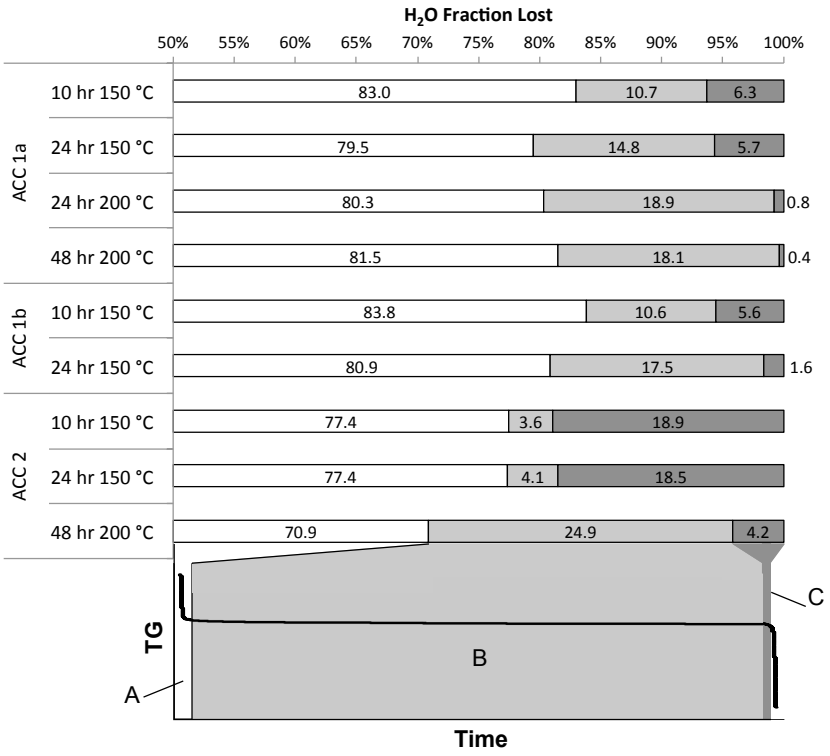

Figure 7. Comparison of the H_2O fraction lost in each heating regime, calculated for all isothermal experiments. Regime A represents the first dynamic heating segment and extends from time 0 to 15 min, when the temperature reached the isothermal set point. Regime B represents the isothermal heating segment, and regime C represents the second dynamic heating and extends from the end of the isothermal heating regime to the crystallization temperature. Note that regimes A, B, and C are different than mass loss regimes 1, 2, and 3 defined for the thermal analysis of partially dehydrated ACC experiments. Data are grouped by experiment and ACC synthesis method.

For all experiments, the mass losses in the first dynamic heating regime (A) are characterized by steep TG slopes and corresponding H_2O loss endotherms in the DSC (Fig. 6). Continuous mass loss occurs in the isothermal regime (B) of all experiments and ACC types. There are no distinctive DSC features in the isothermal heating regime. The (partially) dehydrated samples remain amorphous throughout the long-term isothermal heating as observed by XRD. Mass loss and DSC behaviors vary by sample and experiment in the second dynamic heating regime (C). It should be noted that the mass loss regimes defined for the isothermal experiments are defined differently than mass loss regimes 1, 2, and 3 for the *ex situ* heat pre-treatment experiments (Section 3.1.2). For 10 hr isothermal experiments at 150 ^{o}C, the DSC curve in the second dynamic heating regime (>612 min; Figure **6**c) shows sharp crystallization exotherms (at 376, 231, and 521 °C for ACC samples from synthesis method 1a, 1b, and 2, respectively), which are elevated with respect to crystallization temperatures of non-isothermally heated experiments. These crystallization exotherms coincide with small but distinctive mass losses (Figure **6**c). DSC data from 10 hr isothermal experiments show more positive net reaction enthalpies compared to the TGA-DSC experiments with dynamic heating only (Section 3.1.1): -8.6 vs. -6.7, -5.8 vs. -4.4, and -3.0 vs. -2.1 kJ mole^{-1} for synthesis methods 1a, 1b, and 2,

respectively, with net enthalpy values from basic DSC experiments listed first followed by extended isothermal data. Radha *et al.* found the same enthalpy trend in a comparison of fresh, hydrated and dehydrated synthetic and biogenic ACC samples.[24] Experiments for 24 hr isothermal heating at 150 ^{o}C and 24 and 48 hr experiments at 200 ^{o}C, exhibit crystallization temperatures similar to the dynamic heating experiments described in section 3.1.1.

For all ACC samples, H_2O loss fractions (summarized in Figure **7**) vary significantly by regime with regimes B and C exhibiting more variation than A (A 71–84%, B 4–25%, and C 0.4–19%). Regime A H_2O loss is unaffected by either the temperature or duration of isothermal heating for all three ACC types. For ACC 1a and 1b samples, increasing the duration of the isothermal heating from 10 to 24 hr is correlated with an increase in the H_2O fraction lost in regime B and a decrease in Regime C (there is minimal change from 24 to 48 hr for sample 1a indicating dehydration is at or near maximum for the 24 hr 200 ^{o}C experiment). The same trend is evident for an increase in the isothermal heating temperatures for type 1a and 1b ACC samples, though the magnitudes of the changes differ when increasing temperature versus duration. For ACC 2, an increase in the isothermal duration from 10 to 24 hr heating at 150 ^{o}C causes no change to the H_2O loss fractions. ACC 2 shows significant changes in the regime losses when the isothermal temperature and duration are increased to 200 ^{o}C for 48 hr. Similar to the trends observed for 1a and 1b ACC samples, the fraction in regime B increases for ACC 2 and decreases in regime C with increased isothermal heating temperature.

3.2 X-ray Absorption Fine Structure Spectroscopy

Comparison of the XAFS for the freshly prepared samples of the three synthesis methods reveals no distinguishable differences (supporting information Figure S **7**). XAFS χ-curves and Fourier transform (FT) magnitudes of fresh, hydrated ACC samples from all three synthesis methods were further compared with partially dehydrated ACC samples revealing only minor differences despite significant change in H_2O content (Figure **8** for 1a ACC; Figure S **8** and Figure S **9** for 1b and 2 ACC). After heating to 115 °C, ACC samples have lost 54–64 % of the initial H_2O content (0.4–0.7 moles H_2O/mole $CaCO_3$ lost) depending on synthesis method. The near-edge regions of the absorption spectrum, μ(E), show the pre-edge feature and singlet white line characteristic of ACC (Figure S **8**a for 1a ACC).[29] The k^2-weighted χ(k) curve shows oscillations dominated by a single beat pattern with the expected multi-electron excitations at 2.7, 3.7, and 10.3 Å^{-1}.[118,29] A persistent glitch at 11 Å^{-1} appears in all calcium K-edge data collected at this beamline. The FT magnitude shows a dominant first-shell Ca–O peak; longer backscatter paths are less obvious.[29] Partial dehydration produced a consistent, slight decrease in μ(E), χ(k), and FT amplitudes for 1a and 1b ACC samples. First shell fits of the fresh versus partially dehydrated ACC samples revealed no differences in the Ca–O distance within error (Table S **1** and Figure S **10**).

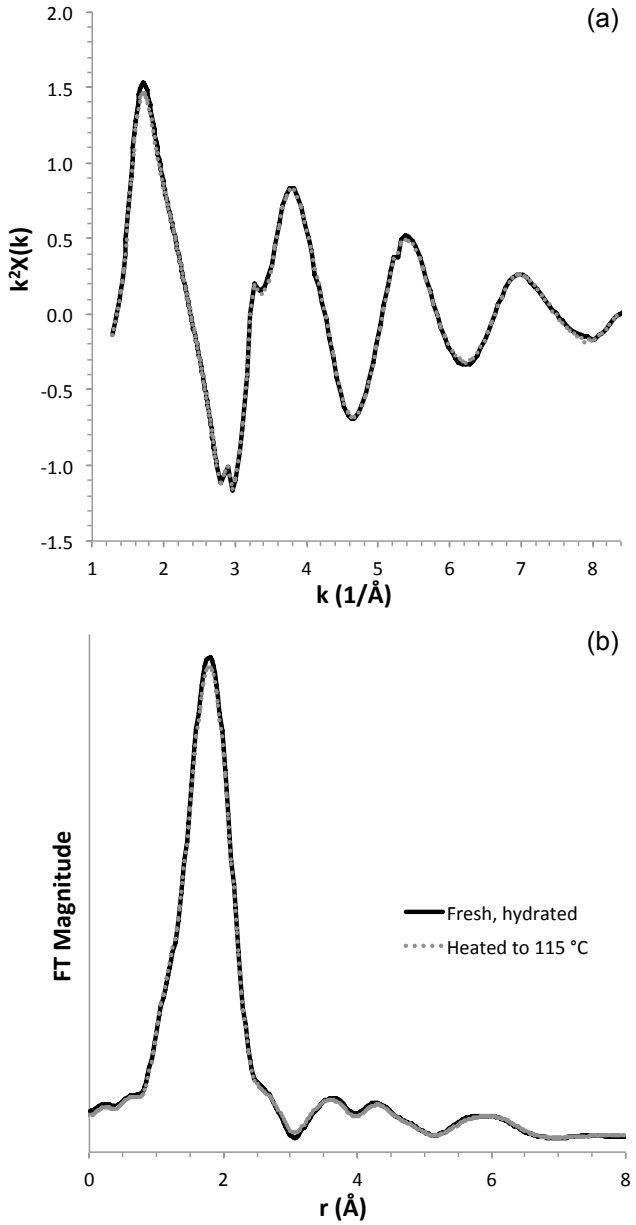

Figure 8. XAFS (a) χ-curves and (b) FT magnitudes of synthesis method 1a ACC where solid black is hydrated and dashed grey is ACC partially dehydrated at 115 °C.

3.3 Synchrotron X-ray Total Scattering

A comparison of the experimental reduced structure functions, F(Q), and pair distribution functions, G(r) or PDF, of ACC 1b, calcite, and vaterite reveals important differences in local, medium, and long-range average structure (Figure **9**; comparison of all ACC patterns in Figure S **11**, 1a ACC is used here for example). The ACC sample shows broad peaks in F(Q), typical of amorphous materials and contrasting with the sharp peaks of the crystalline samples.[29, 41] The F(Q) amplitudes of all three calcium carbonates dampen with increasing Q, which is mainly a consequence of the Q-dependence of the atomic scattering factors. The PDF comparison (Figure **9**b) highlights significant real-space differences amongst the calcium carbonates. ACC exhibits

no observable atom pair correlations beyond 12–13 Å, which is indicative of an amorphous material with only short and medium-range order, and is consistent with previous studies.[119] The first peak of all three PDFs, corresponding to the average C–O bond length, is found at 1.28 Å. The most intense peak, at 2.4 Å, corresponds to the first shell Ca coordination by O with a small contribution from O–O correlations.[29] For ACC, multiple pair correlations contribute to the peaks at 2.9, 4 and 6 Å (see Michel *et al.* for an in-depth discussion of pair contributions from calculated G(r) functions).[29] Features in the ACC PDF dampen quickly after the two broad peaks at approximately 4 and 6 Å with weak correlations visible to 12 Å. These observations are consistent with the findings of Michel *et al.* who reported no pair correlations beyond 15 Å.[29] Comparison of total scattering results of ACC samples from the three synthesis methods shows no discernible differences (Figure S **11**).

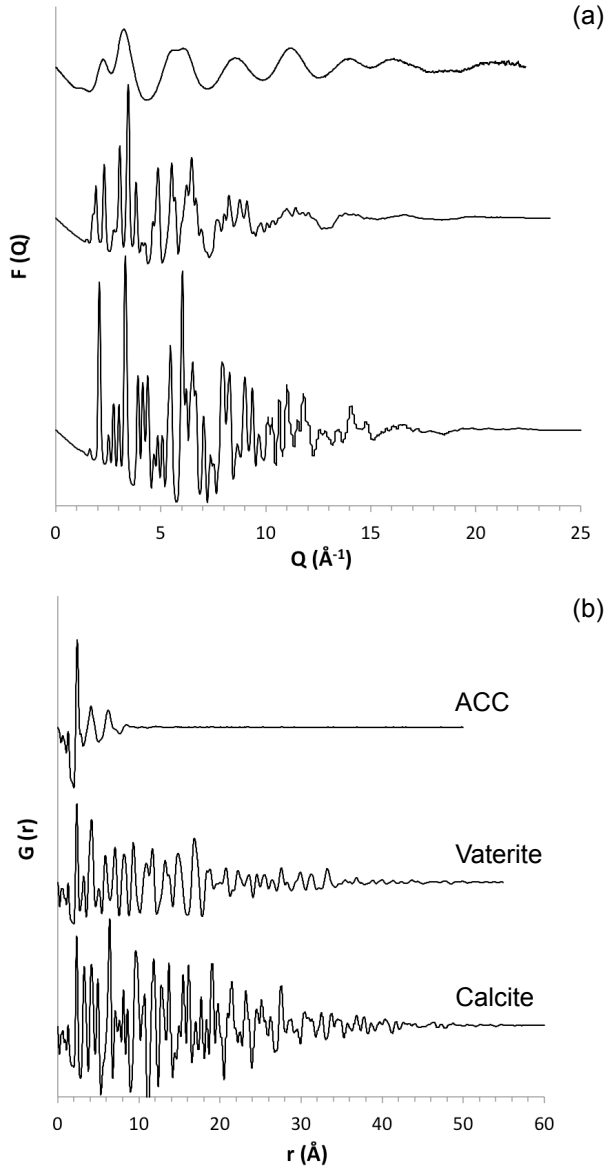

Figure 9. Reduced structure function, F(Q) (a) and pair distribution function, G(r),(b) for synthesis method 1a ACC, vaterite, and calcite.

Changes in F(Q) and G(r) after *ex situ* heating of the 1a ACC samples (to 115 and 150 °C) are subtle despite significant changes to the H_2O content (loss of 46 and 74 % total H_2O, respectively). Figure **10** compares results for fresh, hydrated and partially dehydrated 1a ACC. Corresponding results for ACC samples 1b and 2 are shown in Figure S **12**. However, these latter samples were heated only to 115 °C, corresponding to loss of 46 % H_2O.). The peak at 2.40 Å exhibits a small but progressive shift to lower r (2.38 Å) with increased heating, accompanied by a small but progressive loss in amplitude (Figure S **13**). The 2.40 Å peak shows no observable change in width with heating. The slight shift to lower r is also found for dehydrated ACC samples 1b and 2, although to a lesser extent owing to the smaller H_2O loss 46 %, signaling that these changes, although small, are meaningful (Figure S **13**). The weaker, broad features at 4 and 6 Å show only subtle changes with heating. The most likely explanation for the shift of the 2.40 Å peak to lower r and the corresponding decrease in amplitude is a small decrease in the average coordination number of Ca by O atoms. This would be consistent with the loss of H_2O, but the negligible scattering contribution from H hinders further characterization.[81, 120]

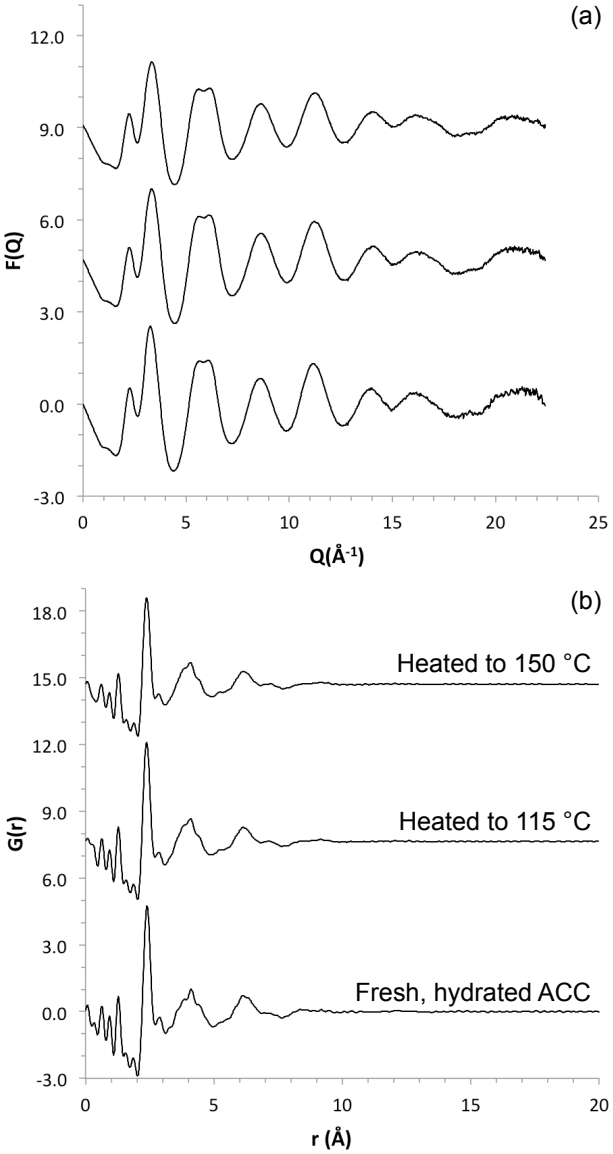

Figure 10. Reduced structure functions (a) and pair distribution functions (b) for fresh and heated synthesis method 1a ACC samples.

3.4 NMR

Two types of ^{1}H NMR experiments were performed that give different but complementary information about the dehydration behavior of ACC. The *ex situ* ^{1}H spectra were acquired indirectly through ^{13}C{^{1}H} HETCOR experiments and show only H environments that are close in proximity to ^{13}C and so incorporated into the ACC structure. The *in situ* experiments used direct ^{1}H excitation (single-pulse) to acquire the spectra, which contain quantitative signal for all proton environments in the sample. It should be noted that it was not feasible to perform the HETCOR experiments for the *in situ* experiments because of the long spectral acquisition times (approximately 10 hr) for a satisfactory spectrum.

3.4.1 *Ex situ* NMR results

The ^{1}H spectra were obtained from each two-dimensional HETCOR spectrum by summing slices of the indirect ^{1}H dimension over the region corresponding to the ^{13}C centerband (164 to 174 ppm in the ^{13}C dimension). The HETCOR experiments included a 50 ms mixing period to allow ^{1}H spin diffusion among all H in proximity to C atoms.[8] These spectra, shown in Figure **11**a, match those obtained previously[29] and illustrate the ^{1}H resonances corresponding to three H environments: a broad spinning sideband envelope from translationally rigid structural H_2O, a narrow peak near +5.3 ppm from restrictedly mobile H_2O, and a less intense, narrow peak at +1.8 ppm from hydroxyl groups (Table **3**). Their presence in the HETCOR spectra indicates that all of these environments must be incorporated into the ACC structure.

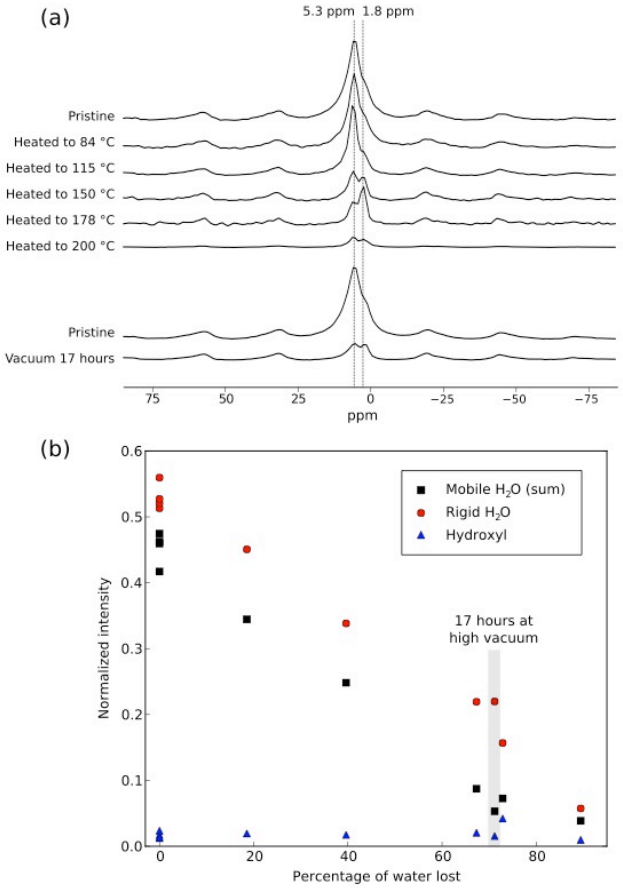

Figure 11. Results from the *ex situ* NMR dehydration experiments: (a) ^{1}H NMR spectra obtained from summed projections of 164 to 174 ppm slices of the ^{13}C{^{1}H} HETCOR spectra. The spectra are normalized such that the integrated intensities are proportional to the total amount of H_2O left in the samples. (b) Trends in the relative fractions of each of the H environments, with absolute intensities taken from least-squares fits of the spectra in (a), and given as a function of the total H_2O lost compared to the pristine sample.

Table 3. Assignment of ^{1}H NMR resonances, ^{1}H chemical shifts (δ_H, ppm) and relative intensities (I) observed for fully hydrated (pristine) ACC.

	In situ directly detected		*Ex situ* indirectly (^{13}C) detected		
Assigned H environment	$d_{H\ (ppm)}$	I	$d_{H\ (ppm)}$	I	Notes
translationally rigid H_2O	6.2(2)	0.39(2)	5.9(2)	0.53(3)	spinning sideband manifold
restrictedly mobile H_2O	4.9(2)	0.61(2)	5.2(2)	0.45(2)	dipolar-coupled; multicomponent centerband[b]
fluid-like mobile H_2O			n.d.[a]	n.d.[a]	self-decoupled; centerband[b]
hydroxyl	1.3(2)	0.014(1)	1.8(2)	0.016(1)	narrow

[a] n.d. indicates not detected; [b]mobile water components not resolved in directly detected spectra

The spectra in Figure **10**a reveal that following dehydration by heating or under high vacuum the number and type of H environments in the sample do not change, but their overall and relative populations do. To quantify these changes, the spectra were first fit with peaks corresponding to the three different environments using the program dmfit.[121] Because of the overlap of the peaks in the isotropic region of the spectra (+20 to -10 ppm), the intensity of the centerband of the rigid H_2O environment was constrained to equal that of its first spinning sideband, thus reducing the number of fitted parameters. This appears to be a good approximation to the overall shape of the spinning sideband manifold, which we can confirm using the spectra obtained without the mixing period, where signals from this environment are more pronounced relative to the other peaks. The shape of the spinning sideband manifold, dominated by the intramolecular ^{1}H–^{1}H dipole coupling, does not change upon dehydration. It was also found that the restrictedly mobile H_2O resonance could not be fit by a single lineshape, requiring a sum of two peaks to account for its intensity. No physical meaning is otherwise attributed to these two fitting components.

To compare the integrated intensities of the fitted peaks for each of the different spectra in Figure **11**a, a normalization scheme was required because the efficiency of the ^{13}C-^{1}H cross polarization changes with the proton concentration in the samples. The total integrated peak intensities were normalized to be proportional to the remaining H_2O content of each of the samples, as estimated from the change in mass of the sample upon dehydration (see Table S **2**).

The normalized, integrated peak intensities, plotted in Figure **11**b, show that both the mobile and rigid H_2O environments decrease in similar proportion with sample dehydration, while the absolute amount of the hydroxyl environment stays approximately constant throughout the series. The sample dehydrated by high vacuum for 17 hr fits with approximately the same trends as the thermally dehydrated samples.

3.4.2 *In situ* NMR results

The directly acquired ^{1}H spectra of ACC obtained during the *in situ* heating profile on a sample of ACC, plotted in Figure **12**a, appear to display the same three proton environments observed in the ^{13}C-detected HETCOR spectra. The trends in the integrated intensities of each of the peaks for the *in situ* measurements are shown in Figure **12**b, where, to allow a direct

comparison with the *ex situ* results in Figure **11**b, the intensities are plotted as a function of the percentage of the total H_2O lost from the sample, as estimated by comparing their total integrated intensity to that of the pristine sample (corresponding to 0 % H_2O loss). The results in Figure **12**b show somewhat similar trends to the behavior of the *ex situ* samples. Both mobile and rigid H_2O environments are reduced with dehydration. Above ~65 % H_2O loss, mobile and rigid populations remain in approximately constant proportion, similar to the *ex situ* results. As for the *ex situ* experiments, the amount of hydroxyl appears to remain constant with increasing thermal dehydration. The mobile H_2O environment appears to account for a much larger fraction of the total proton concentration in the pristine sample for the *in situ* results. In addition, the initial rate of signal loss from the mobile H_2O is greater in the *in situ* results than for the *ex situ* experiments, with 65% of the mobile H_2O lost by 50% dehydration *in situ* compared with 50% in the *ex situ* experiments. These differences can be attributed to the presence of isotropically re-orienting, mobile H_2O (denoted fluid-like, mobile H_2O) that is observed by the directly acquired *in situ* ^1H experiments but not the indirectly acquired CP/HETCOR spectra from the *ex situ* experiments (see Table **3** summary of hydrous ACC components). This fluid-like, mobile H_2O might include weakly bound surface H_2O, isotropically re-orienting H_2O molecules that are de-coupled or physically isolated from the more rigid H environments, or fluid inclusions.

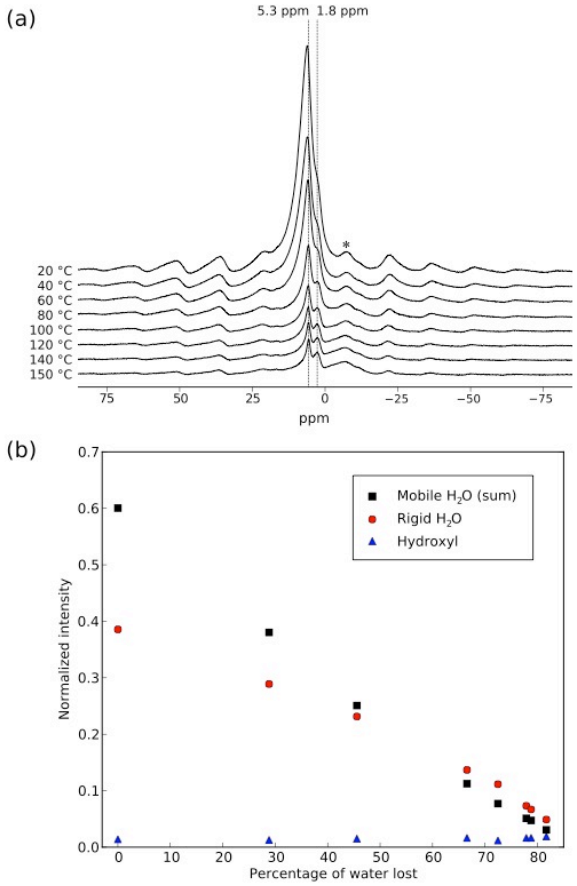

Figure 12. NMR results from the in situ dehydration experiments: (a) directly acquired ^1H NMR spectra acquired at each temperature during heating. The asterisk marks the first spinning sideband, where artifacts from the background subtraction are evident, particularly at higher

temperatures. (b) Trends in the intensities of the signals for each H_2O environment as a function of the total H_2O lost compared to the pristine sample. Integrals are normalized so that the total integral of the pristine, room temperature spectrum is equal to 1.0.

To observe the kinetics involved in the dehydration process, the sample was held at 60 °C for an extra 30 min after temperature equilibration during the *in situ* heating profile. ^{1}H spectra collected at 10-min intervals during this period are displayed in Figure **13**, and show that the sample continues to lose H_2O even after thermal equilibration. The centerband signal, dominated by the mobile H_2O components, shows the most significant intensity decrease, while that in the sidebands is less apparent. The simultaneous loss of signal amplitude across the full centerband region correlates well with a loss of H_2O predominantly from a broad peak associated with the mobile H_2O component.

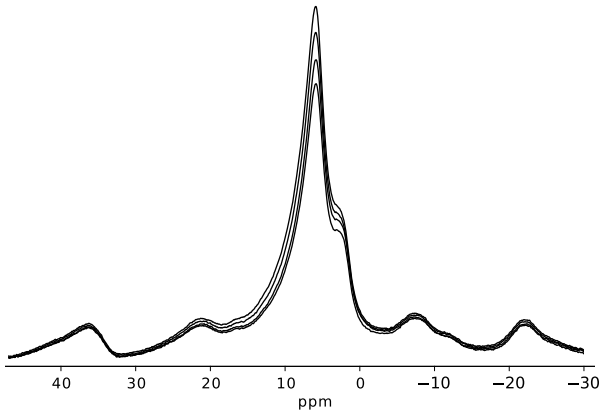

Figure 13. ^{1}H spectra collected *in situ* at 60 °C. The most intense spectrum was taken immediately after the temperature had equilibrated (30 min after the temperature was reached) and the other three, in order of decreasing intensity, at consecutive 10 min intervals. Each spectrum took 2 min to acquire and has the rotor background subtracted. While the sideband intensity remains approximately constant in each spectrum, there is a significant reduction in intensity around the isotropic region.

4. Discussion

4.1 Thermal dehydration of ACC

By combining H_2O mass loss data from TGA with NMR measurements, we can determine how the different H_2O components behave during thermal dehydration of ACC. The NMR results in Figure **11** and Figure **13** show that the H_2O losses in any of the three TGA-defined regimes are not uniquely attributable to individual components, and in fact loss of both the rigid and restrictedly mobile H_2O components occurs throughout all temperature regimes, while loss of fluid-like, mobile H_2O occurs only at lower temperatures. Perhaps more surprisingly, some restrictedly mobile H_2O persists even in the most dehydrated ACC examined by NMR experiments by both *ex situ* and *in situ* heating. The *ex situ* results indicate that the rigid and restrictedly mobile H_2O components, which are almost equally populated in the fresh, fully hydrated samples, are removed simultaneously at nearly constant proportion with increasing

dehydration temperature. The *in situ* experiments reveal that the fluid-like, mobile H_2O component (which cannot be observed indirectly via the ^{13}C CP signal) is lost at a higher rate than the less mobile components (restrictedly mobile and rigid H_2O) up to ~50% dehydration. This fluid-like, mobile H_2O continues to be evolved even when ACC is maintained isothermally at 60 °C (described in Section 3.4.2). The significant change in slope between regimes in the TGA profiles in Figure **5** corresponds to a change from the simultaneous loss of all three H_2O components in regime 1, to the dominant loss of just the rigid and restrictedly mobile components in regime 2. The NMR data show that the hydroxyl content remains approximately constant over the temperature range studied and that its removal contributes to the final weight loss step. However, hydroxyl is unlikely to be the sole source of the small mass loss in regime 3 inasmuch as a similar mass loss was observed in identical experiments on biogenic, hydroxyl-free ACC (unpublished data). Regime 3 mass loss is likely composed of a trapped H_2O component that is inaccessible to the atmosphere, in addition to the hydroxyl. While our results cannot provide a complete structural picture linking hydrous components and the $CaCO_3$ framework, the observed H_2O components must play distinct structural roles in ACC that cause the variations in dehydration and crystallization behavior amongst the three ACC samples (discussed further in Section 4.2).

The TGA and NMR experiments also provide clues about the kinetics of the H_2O loss mechanism with heating. Figure **6** shows that ACC samples held isothermally at 150 °C in the TGA continue to lose appreciable mass (16% of the total H_2O mass over a duration of ~600 min), demonstrating that the dehydration process is kinetically hindered under these conditions. Comparing the regime B and C mass losses of the different isothermal experiments further supports this conclusion. For each ACC type, the isothermal heating temperature and duration affect the fractional H_2O loss (Figure **7**). The most significant differences can be noted in the H_2O losses of the second dynamic heating regime, where the H_2O loss for ACC 1a decreases from 6.3% for 10 hr isothermal heating at 150 °C to 0.4% for 48 hr at 200 °C. This contrast in H_2O loss in regime C is most dramatic for ACC 2 between the 150 and 200 °C experiments.

Thermal analysis of *ex situ* partially dehydrated 1a and 2 ACC samples also shows that loss of hydrous components is impeded in regime 3. Despite being heated to 200 °C (which can generate near anhydrous ACC under extended isothermal conditions), regime 3 mass loss is identical to that for samples pre-treated at much lower temperatures. This indicates that the loss of component(s) in regime 3 is hindered. The mass losses measured in TGA experiments reflect the combined influences of heating rate, duration, temperature, and the inherent kinetic hindrance of H_2O loss. In the relatively fast dynamic heating experiments (including the shorter isothermal heating experiments), not all of the H_2O that could leave the structure had the time to do so.

Further evidence of kinetic hindrance of the evolution of H_2O is seen in the consecutive *in situ* NMR spectra shown in Figure **13**, where the sample continues to lose the mobile H_2O component as long as 30 min after reaching 60 °C. In this instance, however, the rigid H_2O evolves at a much slower rate, which may be due to the lower temperature. Based on these data, we do not consider that the hydration states attained during dynamic or isothermal heating represent metastable equilibrium states. Dehydration appears to be an irreversible process, in agreement with the conclusions of Radha *et al*., [18] and it does not reach completion within the duration of the NMR experiments.

Radha *et al*. proposed that ACC undergoes some structural reorganization during dehydration.[24] Clearly, structural changes are expected to accompany loss of hydrous

components, according to their structural roles. Indeed, our PDF results do show subtle changes in the Ca environment with heating, most likely indicating a small decrease in the average coordination number. This change could reflect partial loss of H_2O from the first coordination sphere of Ca. Such changes with heat-induced dehydration would also be consistent with the molecular dynamics simulations of Saharay *et al.*, who investigated the structural differences in ACC associated with variable hydration states. Partial (Ca–O) radial distribution functions (RDFs) calculated from their structures show a decrease in peak amplitude as well as a shift to smaller radial distance as H_2O content decreases. [81] The changes reported by Saharary *et al.* are greater in magnitude than those indicated by our experimental PDFs, but qualitatively similar. [81] Saharay *et al*. also observed different types of bonds in distinct coordination shells of the ACC structure and preferential loss of H_2O from certain Ca shells as dehydration progressed, supporting our NMR and TGA-DSC observations of discrete H_2O populations.[81] We note, however, that structural changes resulting from (partial) loss of H_2O are not expected to be fully evident in the PDF results owing to the insensitivity of H with X-rays. Moreover, our PDF results are limited to samples that have lost up to 76% of their H_2O. More significant structural changes might be evident in samples with greater H_2O loss. More extreme states of dehydration might also produce discernible changes to the XAFS, which were not observed for the partially dehydrated samples analyzed.

It is clear that the dehydration of ACC proceeds via the simultaneous loss of both mobile and rigid H_2O components, while the hydroxyl component persists until higher temperatures and longer dehydration durations. Significant loss of the fluid-like mobile component early in the dehydration process is consistent with the findings of Radha *et al*., who attributed initial weight loss in their heating experiments to loss of physisorbed H_2O.[24] The rigid H_2O component exhibits interesting behavior in that it is lost from the ACC structure at temperatures as low as 40 °C and over a temperature range in excess of 250 °C, raising the question of its structural role(s) in ACC. This raises the question of how the H_2O loss is kinetically hindered? An equally important question is the mechanism of the kinetic hindrance for H_2O loss, which is presumably linked to the specific structural role of each hydrous component.

4.2 Effects of synthesis method on H_2O content, structure, and transformation behavior of ACC

No obvious structural differences between the freshly prepared three ACC types were evident based on the XAFS and PDF results, yet thermal analysis revealed clear differences in dehydration and crystallization behaviors upon heating. However, these techniques, lacking sensitivity to H, provide little insight to hydrous components of ACC. NMR showed that ACC has four distinct hydrous components. TGA experiments that included an extended isothermal segment showed that the H_2O fractions lost varied significantly depending on the synthesis method. Combining the NMR and extended isothermal TGA results with the absence of obvious differences in the PDF and XAFS results of freshly prepared ACC samples leads us to conclude that the three ACC samples have differing populations of hydrous components, which, in turn, govern the dehydration and crystallization behaviors.

Our findings demonstrate that the H_2O loss and crystallization behavior of ACC are strongly dependent on the synthesis method. We have shown that the release of hydrous components differs significantly between the three ACC types studied (Figure **7**), while overall H_2O contents show some differences but fall in or near the range reported in the literature (1.5, 1.6, and 1.2 moles H_2O/mole $CaCO_3$ for methods 1a, 1b, and 2, respectively). Total H_2O content does not correlate with crystallization temperature (341, 202, and 376 °C for methods 1a, 1b, and

2, respectively),[24] consistent with the conclusions of Radha *et al*., implying that initial H_2O content is not the sole determinant of ACC dehydration behavior. We note that Radha *et al*. found important differences in enthalpy among a series of hydrated ACC samples, confirming that the properties of synthetic samples vary significantly.

We also find that partial dehydration of ACC under isothermal heating for 10 hr at 150 °C elevates the crystallization temperatures above the value recorded for the simple dynamic heating program (no isothermal step). We speculate that this could be caused by exchange among the different hydrous components, accompanying dehydration, and resulting in different distributions and populations of H_2O environments. The near anhydrous ACC samples produced in the 24 and 48 hr isothermal heating experiments have crystallization temperatures that fall within a much narrower range.

5. Conclusions

The complementary techniques employed here provide insight into the role of H_2O in the ACC structure, as well as its dehydration and crystallization behavior. Several studies have proposed anhydrous intermediates in the ACC transformation pathway to crystalline calcium carbonate polymorphs,[19, 24, 79, 93] which serves to emphasize the importance of understanding the ACC dehydration process. NMR analysis of fresh and partially dehydrated ACC samples revealed four distinct hydrous components and showed that dehydration of ACC is characterized by simultaneous losses of both the mobile and rigid H_2O components, while the hydroxyl component is unchanged until crystallization. PDF analysis of similarly dehydrated samples showed subtle but consistent trends reflecting changes in the first coordination sphere of Ca associated with H_2O loss. These findings shed new light on the role that the synthesis method plays in dehydration and crystallization behavior. It is possible that ACC produced using synthesis methods different than in this study would exhibit differences in the types and properties of its hydrous components, thereby resulting in different dehydration and crystallization behaviors. Further studies on near anhydrous ACC using NMR and neutron PDF have the potential to uncover the specific roles of each hydrous component as well as the source of kinetic hindrance of their loss under thermal dehydration conditions. An important question for future study is how these results from thermal experiments relate to dehydration and transformation of ACC at ambient conditions, both *in vivo* and *in vitro*, as applied to biomineralization and biomimetic synthesis. NMR results from experiments at low temperature (60 °C) and vacuum dehydration at ambient temperature show good correspondence with the high temperature results, supporting the relevance of these conclusions to ACC transformations occurring at ambient conditions.

Supporting Information

S1. SEM

SEM comparison of ACC types 1a, 1b, and 2 reveals no visual differences (Figure S **1**). Grain diameter measurements also show no significant differences amongst the three synthesis methods ($\boldsymbol{N \cong 100}$ for each ACC type).

S2. TGA-DSC

S2.1 Combined TGA-DSC and XRD of initial ACC and intermediate and final transformation products are shown in Figure S **2**, Figure S **3**, and Figure S **4**. All XRD patterns were collected with Cu Kα radiation, λ = 1.54 Å.

S2.2 Partial dehydration experiments

Comparisons of crystallization and boundary temperatures from TGA-DSC results for thermally treated samples are shown in Figure S **5** revealing slightly different behaviors. Crystallization and $T_{2/3}$ boundary temperatures remain unchanged with increasing pre-treatment temperature for both 1a and 2 ACC experiments. Regime boundaries, $T_{1/2}$, become elevated (to similar temperatures) above ~175 °C pre-treatment for both experiments. The TGA-DSC traces and the mass loss measurements by regime for the ACC 2 partial dehydration experiment (Figure S **6**) exhibit similar behaviors to those described for sample 1a (Figure **4**). The greatest difference between the two experiments is observed in the mass loss percentages, where synthesis method 2 ACC shows less regime 2 mass loss in the fresh and low pre-treatment temperature samples compared to synthesis method 1a ACC. This is expected from the lower overall H_2O content observed for method 2 compared to 1a ACC (1.2 vs. 1.5 moles H_2O/mole $CaCO_3$, respectively).

S3. XAFS

A comparison of XAFS results for different ACC synthesis methods exhibits minimal differences in local structure (Figure S **7**). ACC and calcite are easily distinguishable by the presence of a characteristic doublet in μ(E) of calcite and by distinct peaks beyond the first oxygen shell in the FT magnitude of calcite. Comparisons of hydrated and partially dehydrated ACC samples 1a, 1b, and 2 show only minor differences for dehydrated samples in μ(E) (Figure S **8**), and in χ(k) and FT magnitude spectra (Figure S **9**). Single shell fits were performed in R-space using the Ca-O path amplitude and phase calculated using FEFF7, based on the calcite structure. The S_0^2 value was fixed at 0.9 and the coordination number fixed at 6. Values for R, σ^2, and E_0 shift were allowed to float during fits. Fit results are listed in Table S **1** with sample fits for ACC 2 shown in Figure S **10**. Most of the Ca K-edge XAFS spectra were strongly impacted by several large glitches that resulted in the use of a limited range of k-space (typically 1.16 to 10.1 $Å^{-1}$). This had the effect of broadening the main peak and limiting the resolution of the fits.

S4. X-ray total scattering

Comparisons of reduced structure functions, F(Q), and PDFs, G(r), yielded no discernible structural differences among synthesis method samples 1a, 1b, and 2 (Figure S **11**). Figure **10** (main article) showed the effects of heating to 115 and 150 ^oC on F(Q) and the PED for ACC sample 1a. Only small changes were evident, as described below. Figure S **12** shows the corresponding F(Q) and PDFs for ACC samples 1b and 2 after heating to 115 ^oC, with similarly small differences. Ex situ heating to 150 ^oC resulted in the onset of crystallization, likely due to flowing air (dry nitrogen was used as the purge gas in the TGA-DSC).

Figure S **13** shows an expanded view of the region containing the main peak at 2.40 Å, corresponding to the Ca-O distance, with a small contribution from O-O distances in the carbonate unit. With heating to 115 ^{o}C, and to 150 ^{o}C for ACC sample 1a, there is a shift of the 2.40 Å peak to lower r (2.38 Å) and a small decrease in amplitude, consistent with a small decrease in the average coordination of Ca.

S5. NMR

Table S **2** lists the mass loss percentages used to normalize NMR results shown in Figure **11**. The mass loss is calculated directly from the TGA weight loss data for each sample dehydrated by heating, and by a measurement of sample weight before and after dehydration in the case of the vacuum-treated sample. An estimate of the total proportion of H_2O lost by each sample during the dehydration process is also shown. The conversion assumes the change in mass to be solely due to the loss of H_2O, and gives an estimate of the total fraction of H_2O in the pristine material to be 22%.

S6. FT-IR

S6.1 Methods

Attenuated total reflectance (ATR) Fourier transform infrared (FT-IR) spectra (4000–400 cm^{-1}) were collected for hydrated and partially dehydrated ACC samples synthesized via methods 1a, 1b, and 2 using a Nicolet 6700 FTIR Spectrometer. Samples were analyzed within 15 min of synthesis, and spectra are presented with the baseline subtracted.

S6.2 Results

Figure S **14** shows a comparison of ATR FT-IR spectra collected for hydrated and partially dehydrated (6–10 % total mass loss or 0.8 moles H_2O/mole $CaCO_3$ remaining) ACC from synthesis method 1b. Bending vibrations of O–H produce the small peak at 1630 cm^{-1}, and the asymmetric stretch of H_2O contributes to the broad peak centered at 3300 cm^{-1}.[68] Both H_2O-related peaks are diminished after sample heating. The internal CO_3 vibrational modes ν_2, ν_3, and ν_4 are located at 862/872, split peaks at 1390 and 1450, and 712 cm^{-1}, respectively.[31] The position of the ν_2 mode (862 cm^{-1} for ACC shifting to 872 cm^{-1} for calcite), the H_2O vibrations, attenuation of the ν_4 mode for ACC samples, and the shoulder at 1450 cm^{-1} distinguish ACC from crystalline calcium carbonate.[68] Peak broadening is also an indication of amorphous character.[68] Dehydration causes no shift in the ν_2 mode peak position, confirming XRD and total scattering observations that partially dehydrated samples remain amorphous.

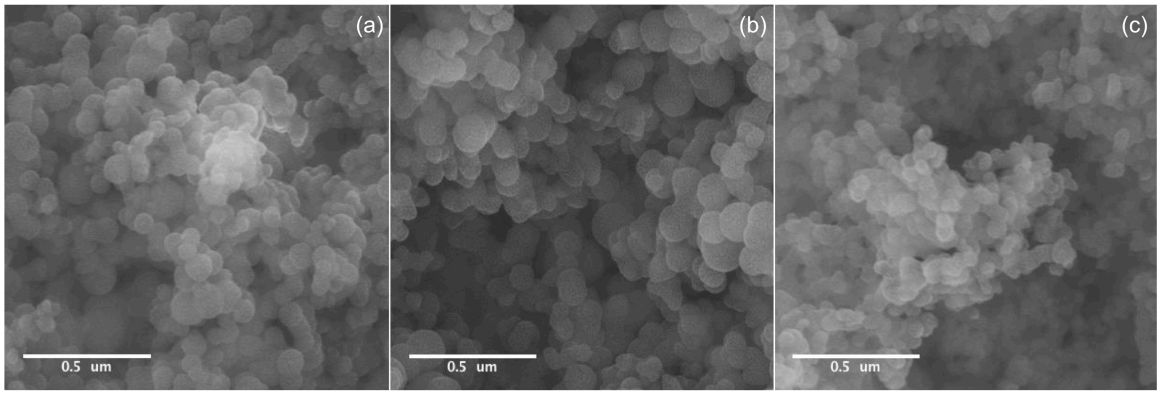

Figure S 1. SEM comparison of ACC from synthesis methods (a) 1a, (b) 1b, and (c) 2.

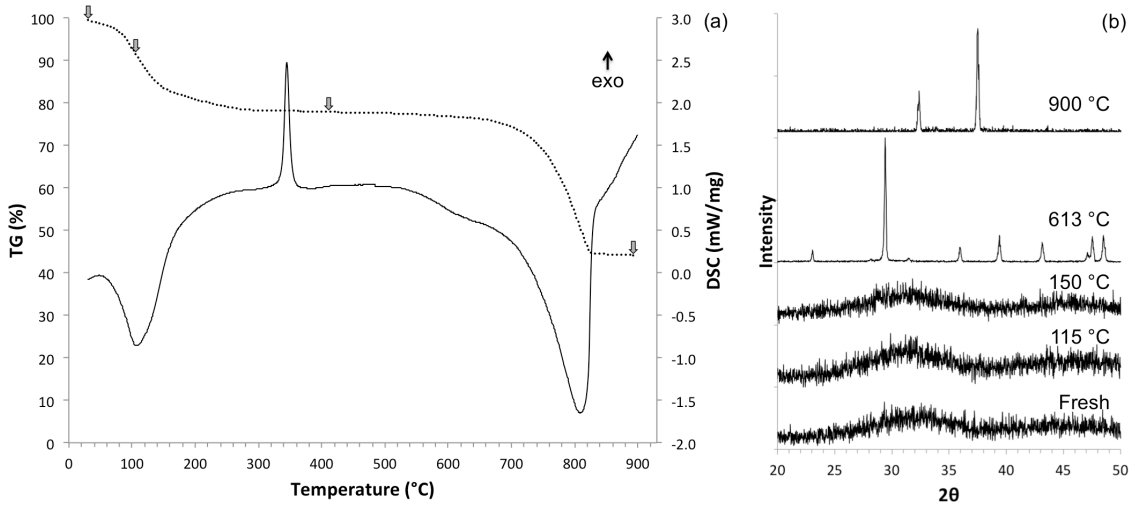

Figure S 2. Weight loss and heat flow data for (a) ACC synthesized by method 1a and associated XRD patterns of (b) ACC (fresh, 115 °C, 150 °C), calcite (613 °C), and calcium oxide (900 °C) noted with arrows on the TG curve. XRD patterns were collected with Cu Kα radiation, λ = 1.54 Å. Vertical XRD intensity scales for the crystalline materials are different than those for the amorphous patterns. The indicated temperatures are the temperatures at which the TGA-DSC heating program was interrupted.

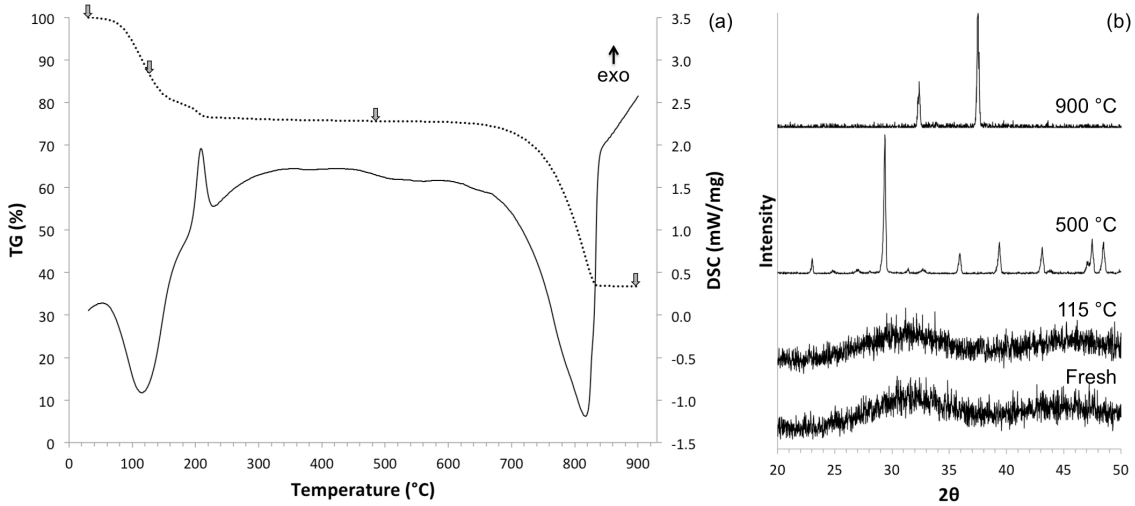

Figure S 3. TGA-DSC results for synthesis method 1b ACC (a) with corresponding XRD patterns of fresh ACC and ACC heated to 115 °C), calcite and a small amount of vaterite (500 °C), and (c) calcium oxide (900 °C). XRD patterns were collected with Cu Kα radiation, λ = 1.54 Å. Vertical XRD intensity scales for the crystalline materials are different than those for the amorphous patterns. The arrows in (a) indicate the temperatures at which the TGA-DSC heating program was interrupted.

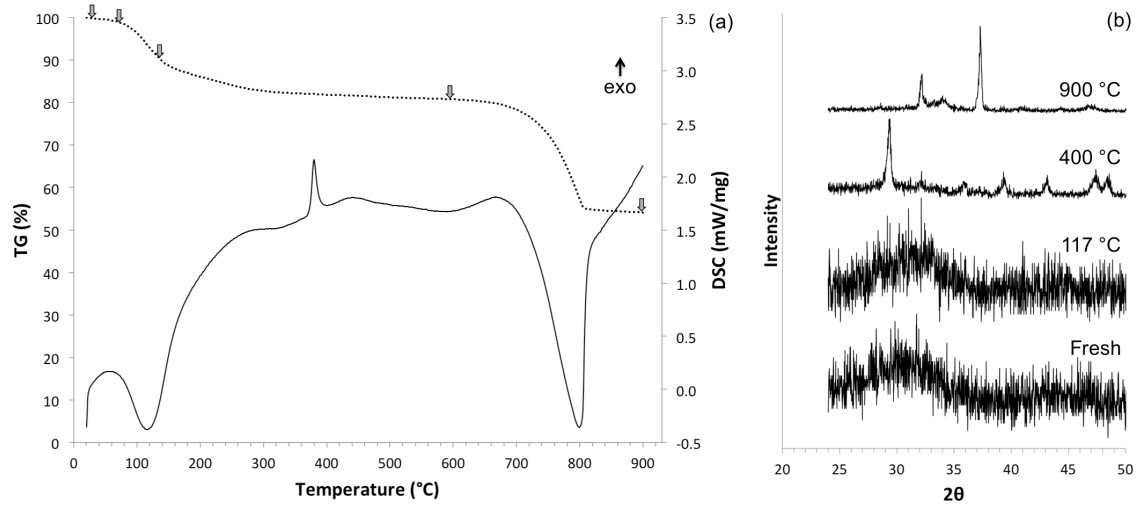

Figure S 4. TGA-DSC of synthesis method 2 ACC (a) with corresponding XRD patterns of ACC (fresh and heated to 117 °C), calcite (400 °C), and calcium oxide and a weak peak of unknown origin at ~34 °2θ (900 °C). XRD patterns were collected with Cu Kα radiation, λ = 1.54 Å. Vertical XRD intensity scales for the crystalline materials are different than those for the amorphous patterns. The arrows indicate the temperatures at which the TGA-DSC heating program was interrupted.

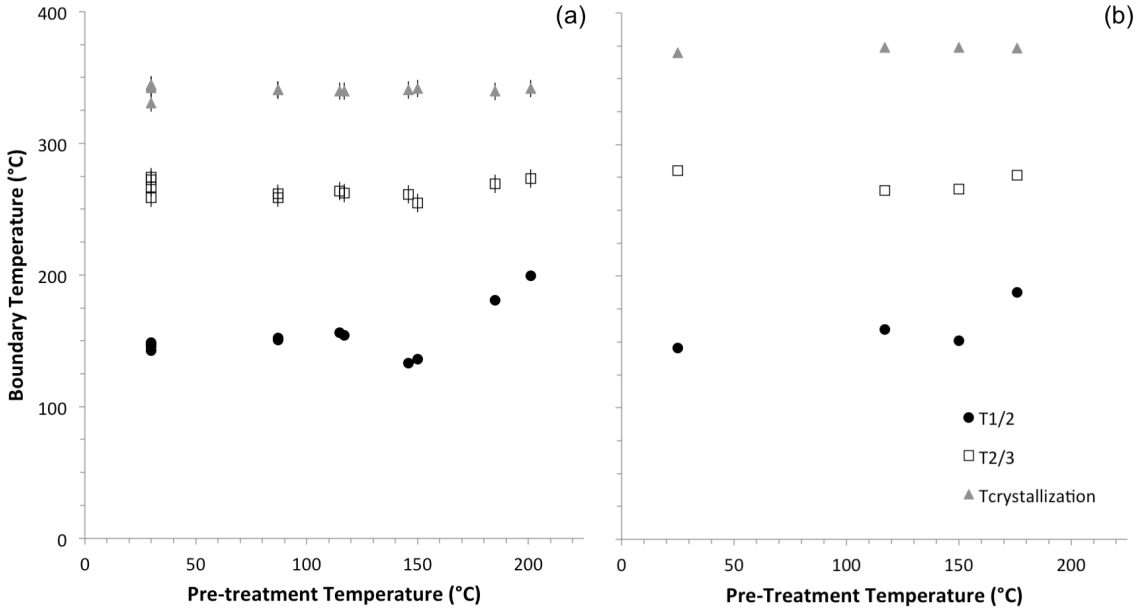

Figure S 5. Regime boundary and crystallization temperatures with increasing pre-treatment temperatures for TGA-DSC partial dehydration experiments on synthesis methods (a) 1a and (b) 2 ACC samples.

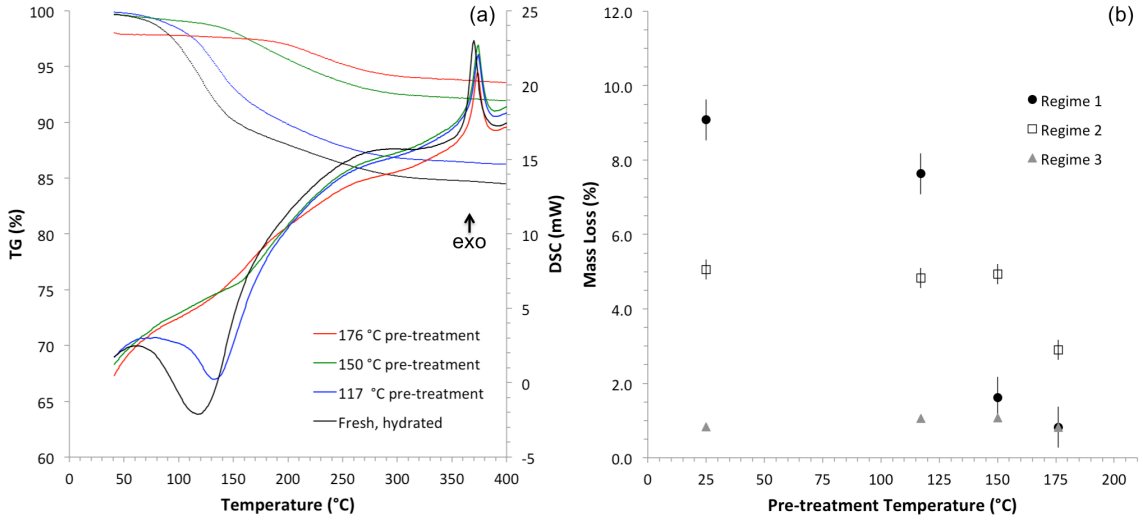

Figure S 6. Results for partial dehydration experiments on ACC 2 showing (a) TGA-DSC of samples with increasing pre-treatment temperatures and (b) regime mass losses with increasing pre-treatment temperature.

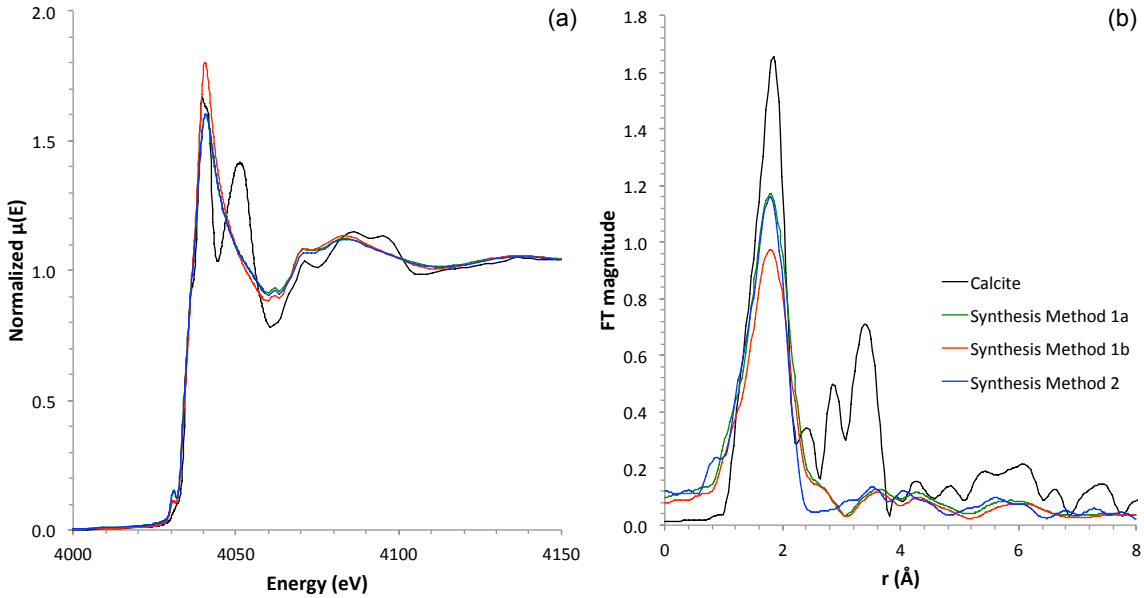

Figure S 7. Comparison of Ca K-edge XAFS data for calcite and fresh, hydrated ACC samples showing (a) the near-edge region and (b) the Fourier transform magnitude.

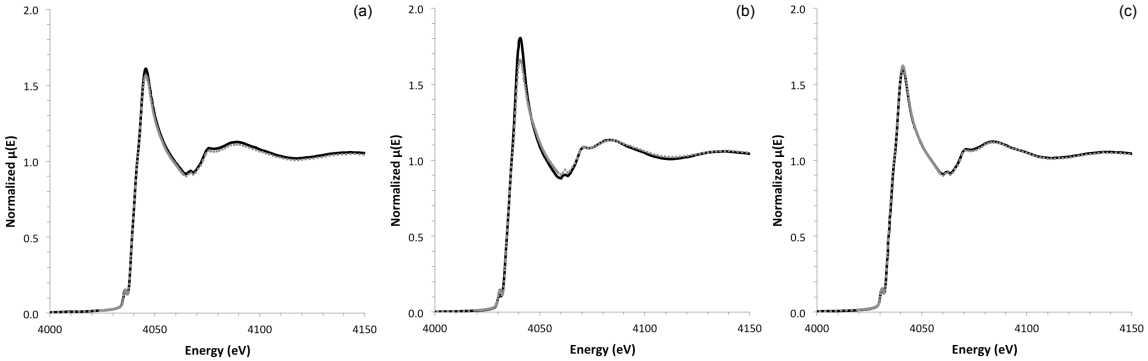

Figure S 8. XAFS of hydrated (solid black) and partially dehydrated to 115 °C (dashed grey) of ACC type (a) 1a, (b) 1b, and (c) 2 samples showing the near-edge region of the normalized adsorption spectrum.

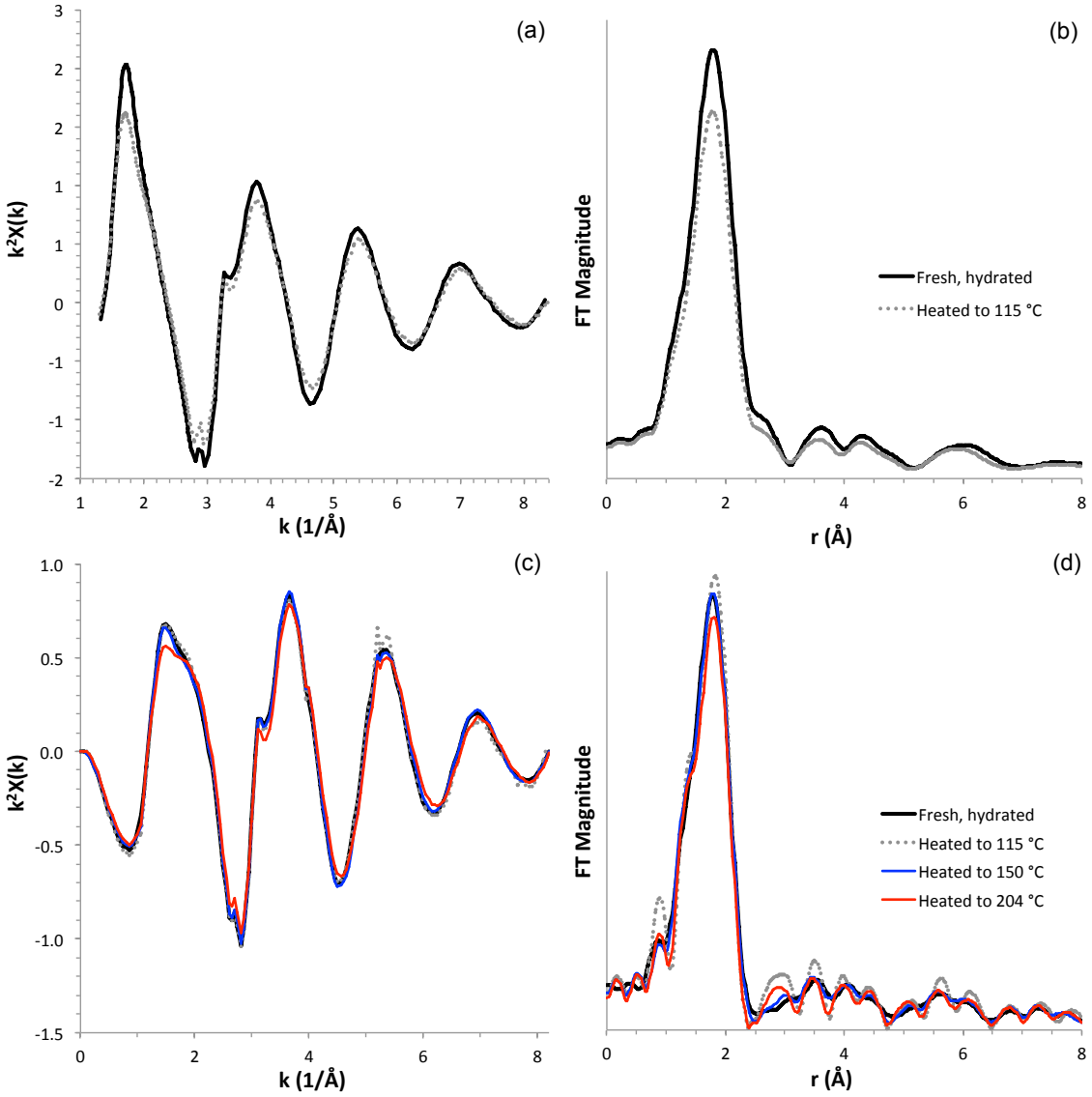

Figure S 9. XAFS results for ACC 1b (top) and 2 (bottom) showing (a, c) the $k^2\chi(k)$ and (b, d) the Fourier transform magnitude.

Table S 1. XAFS fit results for fresh and partially dehydrated ACC 2 samples with S_0^2 fixed at 0.9 and CN fixed at 6.

ACC	Dehydration	Ca—O distance (Å)*	σ^2 (Å^2)**	E_0 shift
1a	none	2.38	0.013	2.4
1a	115 °C	2.38	0.014	2.5
1a	150 °C	2.38	0.016	2.4
1a	200 °C	2.37	0.017	2.4
2	none	2.38	0.013	2.4
2	115 °C	2.38	0.012	2.6
2	150 °C	2.37	0.013	2.4
2	204 °C	2.37	0.014	2.5

* Distance error is ± 0.01-0.02 Å.

** σ^2 error is ± 0.005.

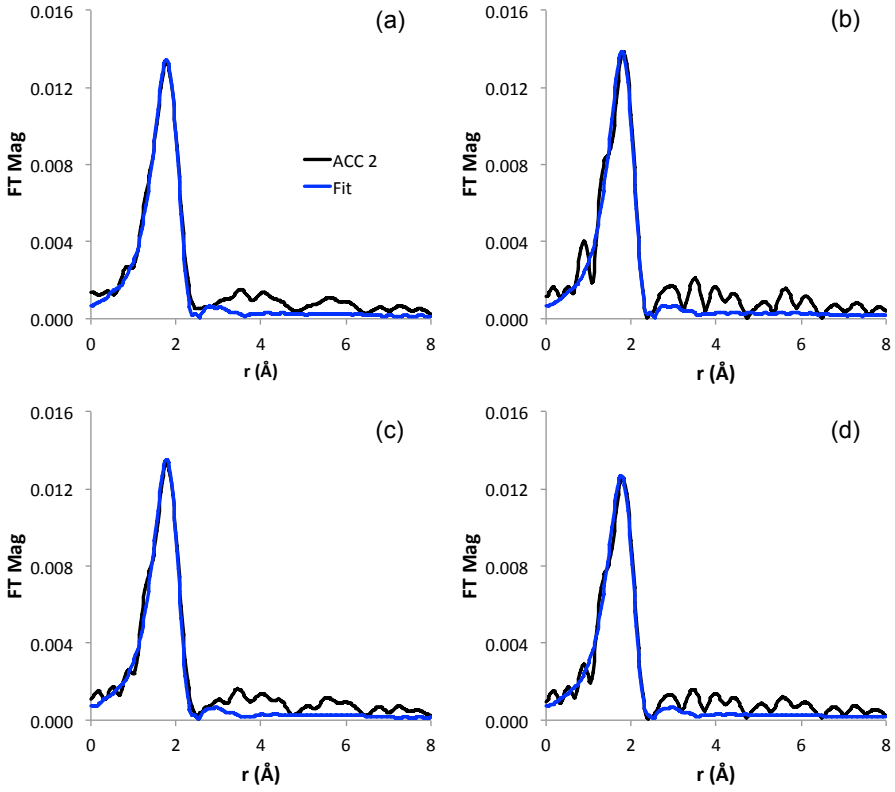

Figure S 10. XAFS first shell fits for synthesis method 2 ACC where black lines represent the experimental data and blue lines represent the fits for (a) fresh, (b) heated to 115 °C, (c) heated to 150 °C, and (b) heated to 204 °C.

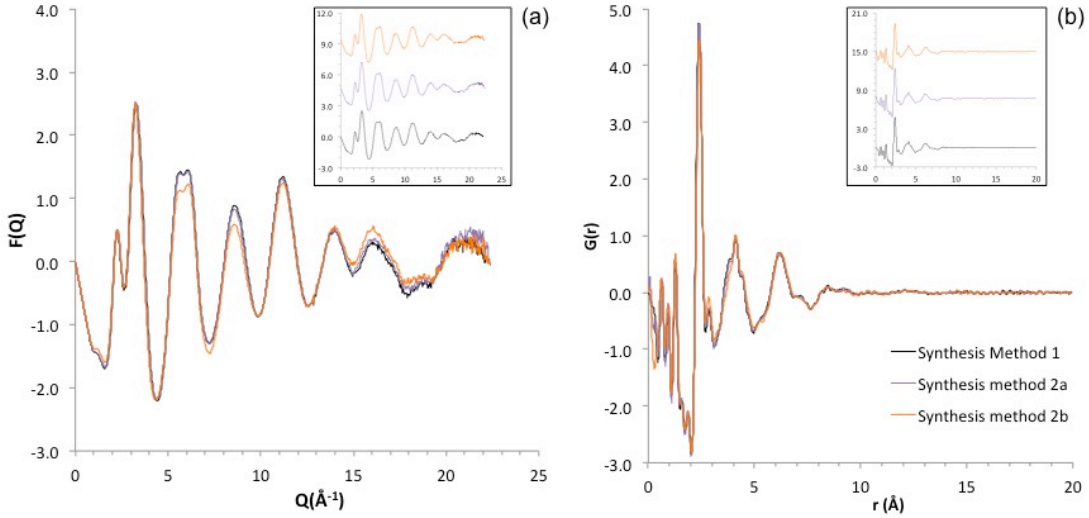

Figure S 11. Comparison of total scattering data for ACC from different synthesis methods: (a) reduced structure function, F(Q), and (b) pair distribution function, G(r).

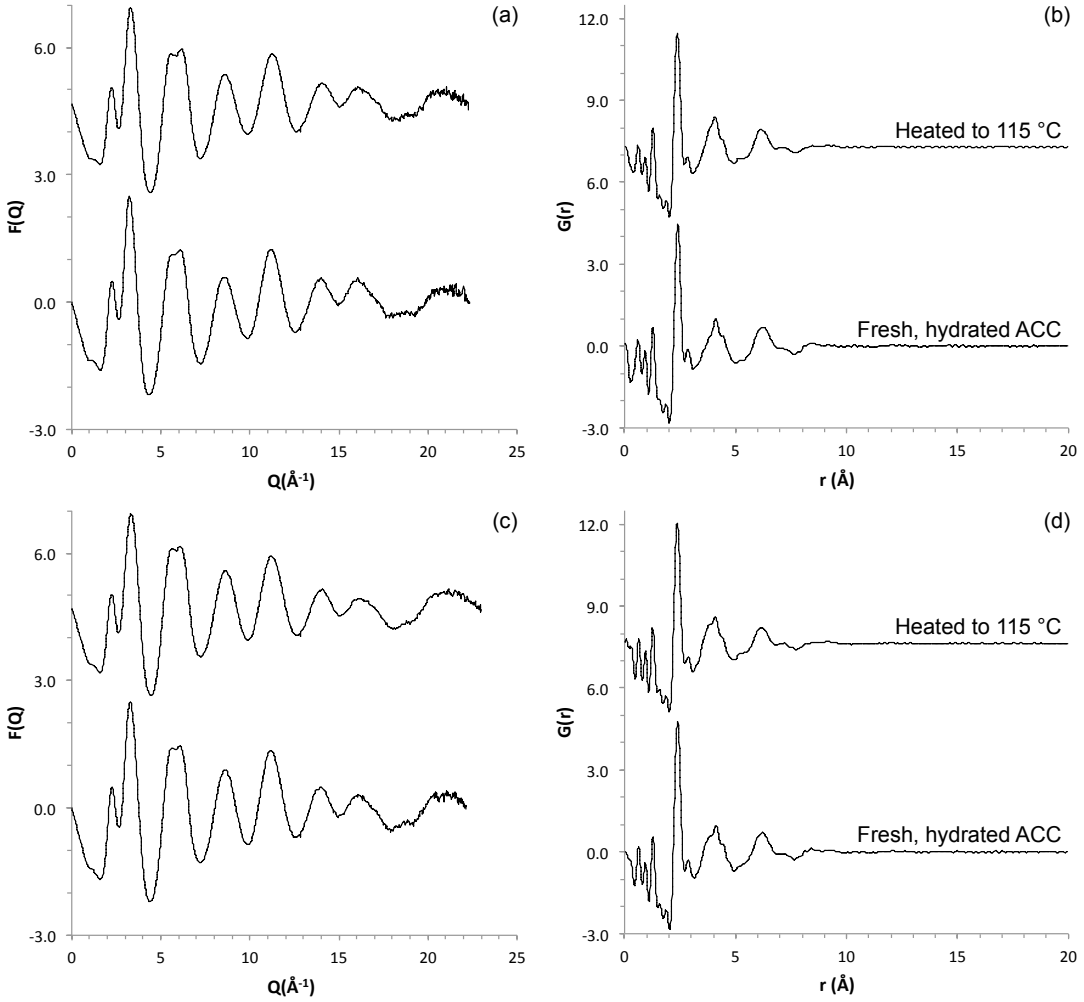

Figure S 12. Comparison of F(Q) and PDFs, G(r), for hydrated and partially dehydrated synthesis method (a/b) 1b and (c/d) 2 ACC.

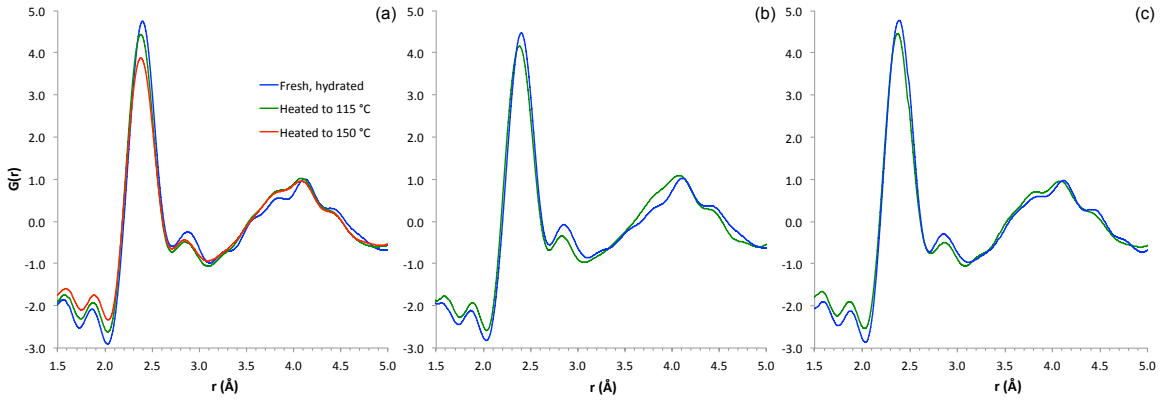

Figure S 13. Expanded view of the PDFs shown in Figures 10 and S12, showing the effects of heating: (a) ACC 1a (b) ACC 1b, and (c) ACC 2. Dehydrated samples were heated in a mechanical oven in flowing air at a rate of 10 °C/min.

Table S 2. Mass loss data for the 1a ACC samples used in the NMR experiments, and the corresponding H_2O loss during dehydration.

Sample treatment	Total mass loss (%)	H_2O lost (%)
Unheated	0.0	0.0
Heated to 84 °C	4.0	18.6
Heated to 115 °C	8.6	39.6
Heated to 150 °C	14.7	67.3
Heated to 178 °C	15.9	72.9
Heated to 200 °C	19.5	89.4
Vacuum for 17 hr*	15.5	71.2

* At 20 °C

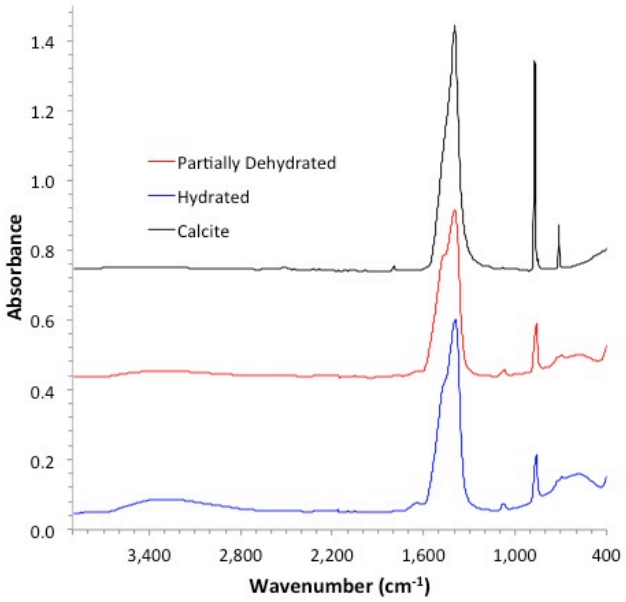

Figure S 14. ATR FT-IR spectra of fresh and partially dehydrated ACC 1b (heated to 115 ^{o}C) and calcite reference. Background subtracted and arbitrary vertical offsets of 0.4 and 0.7 of dehydrated ACC and calcite, respectively.

Chapter 3: Transformation of synthetic amorphous calcium carbonate: *In situ* X-ray total scattering study

ABSTRACT: Despite much interest in the industrial, environmental, and biological applications of amorphous calcium carbonate (ACC), few studies have been able to examine the amorphous to crystalline transformation in situ. We used synchrotron X-ray total scattering and pair distribution function analysis to characterize the in situ transformation of ACC, examining samples prepared by different synthesis methods and at different hydration states. ACC samples were allowed to react in capillaries at ambient P and T with deionized water or a calcite-equilibrated solution. Reaction progress could be followed using multiple regressions of in situ I(Q) data, with calcite, vaterite, and fresh ACC end-members.

The different ACC samples exhibited a range of results in terms of both transformation rate and pathway. Transformation kinetics varied according to ACC synthesis method, and in turn transformation pathway was affected strongly by kinetics. Experiments with slower transformation kinetics showed ACC transforming directly to calcite, while experiments with the fastest transformation rates yielded a mixture of calcite and vaterite. In experiments where transformation produced a mixture of phases, the initial crystallization of vaterite and calcite was simultaneous. Transformation of ACC directly to calcite and the simultaneous formation of vaterite and calcite both indicate that vaterite is not an essential precursor phase in the formation of calcite. However, ex situ analysis of capillaries long after in situ analysis did show a secondary transformation from vaterite to calcite, with slower reaction kinetics than either of the initial crystallization reactions from the amorphous phase.

Reactions involving calcite-equilibrated solution and partially dehydrated ACC both correlated with an overall decrease in the transformation kinetics. We attribute these effects to a decreased departure from equilibrium and the distinct structural roles of the various hydrous components of the partially dehydrated ACC. The in situ structural analyses used in this study shed light on the possible controls manipulated by organisms to direct transformation in vivo with potential applications for biomimetic synthesis.

1. Introduction

Amorphous calcium carbonate (ACC) is well known as a metastable precursor in the formation of crystalline forms of calcium carbonate in both biological and inorganic systems.[1, 3, 5, 122] Directed assembly of ACC during biomineralization, with subsequent crystallization, allows organisms to produce calcium carbonate skeletal components with specific shapes and functions, features that are difficult to achieve via direct crystallization from solution.[51, 52, 123] In some organisms, ACC remains in an amorphous state while in others ACC is used as calcium storage; Addadi, Wiener, and others have described and categorized these different types of biological and inorganic ACC.[1, 3, 18] This amorphous precursor strategy has been adopted for biomimetic synthesis of functional materials, including thin films.[27, 49, 57, 67, 68, 70, 71, 75, 102, 124] The ACC produced during inorganic synthesis from highly supersaturated solutions is typically hydrated, with approximate composition $CaCO_3 \cdot H_2O$.[29, 31, 90] Heating over the temperature range 80–180 ^{o}C has produced nearly anhydrous ACC.[125] Both hydrated and anhydrous ACC are far less stable than any of the crystalline forms, such as calcite, aragonite, vaterite, or monohydrocalcite.[24, 93, 95] Consequently, transformation of ACC to crystalline $CaCO_3$ is strongly favored. Much effort has been focused on temporary stabilization of ACC and on controls that direct its crystallization, including the use of additives and templates.[18, 40, 41, 44, 54, 57, 64, 76, 85, 91, 112, 126]

Several previous studies have characterized the transformation of additive-free ACC under different environmental conditions, including in solution and in air at various humidity conditions. A significant observation from these studies is that the first crystalline phase to form

may be a metastable phase (e.g., vaterite) or a mixture of phases. For example, Ogino et al. followed the sequence of ACC formation and transformation in solution at various temperatures.[95] Over the temperature range 14–30 ^{o}C, the initial transformation product of ACC was observed to be a mixture of vaterite and calcite, with the relative proportions dependent on temperature. Aragonite and calcite were formed at higher temperatures. Pontoni et al. and Bots et al. both used in situ small- and wide-angle X-ray scattering to follow the formation and transformation of ACC in solution.[79, 92] Pontoni et al. noted formation of vaterite, aragonite, and calcite in the same experiment, with evidence for the appearance of crystallites within several minutes of ACC formation. Bots et al. observed that ACC began to crystallize vaterite in a matter of seconds, and subsequently to calcite at longer time scales.[79] Shen et al. also examined ACC transformation in solution, finding that the transformation product, appearing within the first few minutes, was either calcite or a mixture of calcite and vaterite.[71] Rodriguez-Blanco et al. studied the transformation of ACC in solution, in situ and ex situ, using both scattering and spectroscopic techniques to characterize the formation of crystalline products. They found that vaterite was the initial crystalline phase to form, with diffraction peaks appearing after 14 min at 7.5 ^{o}C and complete transformation of the ACC to vaterite in 12 min at 25 ^{o}C. Formation of calcite followed and was observed to be concurrent with the disappearance of vaterite. These studies indicate that the transformation pathway is not unique, with different, and sometimes multiple, crystalline phases appearing as the stable phase (calcite) is reached. There appear to be many mechanistic controls on transformation kinetics and polymorph selection, but several areas are largely unexplored, such as the roles of ACC hydration state and composition of the reacting medium.

Despite the considerable interest in ACC transformation, there has been relatively little structural characterization of the ACC leading up to and during crystallization. A recent study of sea urchin larval spicules by Politi et al. (2008) concluded that initially hydrated ACC transforms to calcite via an intermediate anhydrous ACC. Support for this transformation sequence for synthetic and biogenic ACC comes from calorimetric, X-ray scatting, and spectroscopic results, though these are not conclusive.[24, 79, 93] These findings point to the importance of H_2O in the ACC transformation as well as the necessity to find methods that allow researchers to look at the ACC structure in situ.

Previously we demonstrated that high-energy X-ray total scattering and pair distribution function analysis, combined with nuclear magnetic resonance spectroscopy, offered new insight to both the calcium rich framework and the H_2O structure of synthetic and biogenic ACC.[21, 29, 125] We reported pair-distribution functions (PDF) that revealed the presence of intermediate-range structural order in hydrated synthetic ACC as well as subtle evidence for the structural effects of dehydration.[29, 125] Goodwin et al. used PDF results to develop a structure model for hydrated ACC using reverse Monte Carlo refinement methods. Atom pair correlations extending over the range 6-15 Å observed in the PDF are interpreted as a Ca-rich network involving CO_3 and H_2O ligands, partially supported by hydrogen bonding.[30] ^{1}H and ^{13}C NMR results demonstrated the presence of four hydrous components indicating multiple roles for H atoms in the ACC structure.[29, 125] Our recent work on the heat-induced dehydration of synthetic ACC samples defined a multi-stage H_2O loss process with the possibility of dynamic exchange between hydrous components to maintain ACC structure to low H_2O contents. These studies have provided a new view of the roles of H_2O and short- and medium-range structure in ACC. In the present study, we extend these approaches to investigate the transformation of hydrated and partially dehydrated ACC to crystalline forms in deionized (DI) water and calcite-equilibrated

(Cc-eq) solution. Combining the in situ structural information with time-resolved plots of mineral fractions during transformation, we can provide insight into relative transformation kinetics and polymorph selection for three ACC types. Particular attention is given to the short- and medium-range structural changes that accompany transformation, as well as the effects of reacting fluid and ACC hydration state.

2. Methods

2.1 Synthesis of ACC samples

Three approaches were used for synthesizing ACC, broadly following those described by Michel et al. and Schmidt et al.[29] The first two synthesis methods (SM 1a and 1b) adapted the procedures described by Koga et al.,[25] wherein equimolar calcium chloride and sodium carbonate solutions were rapidly mixed. For SM 1a, 5 mL of 0.5 N NaOH solution was added to 20 mL of 0.02 M Na_2CO_3 solution. The resulting pH 12.7 solution was mixed with 20 mL of a 0.02 M $CaCl_2$ solution and stirred rapidly. For SM 1b, the NaOH solution was omitted, resulting in a pH 9.6 Na_2CO_3 solution mixed with equimolar and equivolume $CaCl_2$ solution. For methods 1a and 1b, a white precipitate formed immediately upon addition of the $CaCl_2$ solution.

The third ACC synthesis method (SM 2) is based on the procedure described by Faatz et al. (2004), using dimethyl carbonate as the carbonate source.[26] For this procedure, 147 mg of solid calcium chloride and 450 mg of dimethyl carbonate are added to 80 mL deionized water, followed by addition of 20 mL of 0.5 M sodium hydroxide solution. The ACC precipitate formed after 3–5 min of stirring.

For all three synthesis procedures, the precipitate was immediately vacuum-filtered and rinsed with fresh acetone to dry the solid, yielding a white, powdery material. The dry ACC was gently ground and placed under soft vacuum for 10–20 min before further experiments. Soft vacuum pumping produced no significant differences to ACC water composition on the 5–30 min time frame, as determined by thermal analysis experiments. All syntheses were conducted at room temperature in open air.

Koga et al. and Schmidt et al. observed that thermal properties of the ACC produced with the Na_2CO_3 carbonate source differed according to the amount of NaOH added, with an attendant effect on pH of the precipitating solution.[25, 125] With increasing pH, the exothermic peak corresponding to crystallization as observed in differential scanning calorimetry is shifted to higher temperatures. Schmidt et al. showed that the ACC samples produced with addition of NaOH (solution pH 12.7) exhibit a crystallization exotherm at 340 °C, whereas those produced without NaOH addition (solution pH 9.6) exhibit the crystallization exotherm at 200 °C.[125] While the ACC 2 does not fit perfectly on this linear trend, it does exhibit a higher crystallization temperature (376 °C) from a high pH starting solution (12.9).

2.2 Reference Samples

Reagent grade calcite was obtained from Spectrum Chemicals, rinsed, and dried prior to analysis. The procedures of Gebauer et al. were adapted for vaterite synthesis.[34, 35] High concentration equimolar calcium chloride and sodium carbonate solutions were mixed rapidly, stirred for 5 min, vacuum filtered, and rinsed with fresh acetone. Pure, synthetic aragonite was also used as a standard.

2.3 ACC dehydration procedures

ACC samples were partially dehydrated by heating in a Lindberg Blue Mechanical Oven flowing air. Fresh samples were heated from 30 to 115 °C. Typical mass losses from thermal analyses and the corresponding H_2O compositions calculated for the three ACC samples are listed in Table **4**.

Table 4. Partial dehydration mass loss and H_2O compositions for ACC 1a, 1b, and 2.

	Fresh ACC	Partially dehydrated ACC	
ACC	Initial (mol H_2O/mol $CaCO_3$)	Remaining (mol H_2O/mol $CaCO_3$)	Remaining H_2O fraction (%)
1a	1.5	0.8	54.2
1b	1.6	0.9	54.4
2	1.2	0.8	64.7

2.4 X-ray total scattering and the pair distribution function

X-ray total scattering data were collected at Argonne National Laboratory's Advanced Photon Source, beamline 11-ID-B. A Si(311) monochromator was used to select 58.8 keV X-rays (0.2127 A). A Perkin-Elmer amorphous silicon area detector was used to collect scattered intensities. Sample-detector distance and detector orthogonality were calibrated using a NIST CeO_2 reference standard. 2-D intensity data were converted to 1-D using the program Fit2D.[115] The 1-D intensity data were normalized, background subtracted, and transformed into *Q*-space (*I(Q)* function) using the PDFgetX2 program.[116, 117] Incident X-ray beam intensities were normalized (when necessary) to allow direct comparison of *I(Q)* data among samples. *I(Q)* data were further transformed into the structure function and the reduced structure function, *S(Q)* and *F(Q)*, which were Fourier transformed to obtain the pair distribution function, *G(r)* or PDF, using PDFgetX2 (Eqn. 1).[114, 116] Compositions used for PDF data processing are shown in Supporting Information (Table S **3**).

$$G(r) = \frac{2}{\pi}\int_0^\infty Q[S(Q) - 1]\sin(Qr)\,dQ \qquad \text{Equation 1}$$

2.5 *In situ* ACC transformation experiments

X-ray total scattering data were collected during reaction of ACC with low-conductivity deionized (DI) water or calcite-equilibrated solution (Cc-eq solution). To allow *in situ* data collection, the solution was introduced through small-diameter tubing into the Kapton capillary containing dry ACC (Figure **14**). A complete scattering spectrum was collected over 15 sec, but an overhead of approximately 9 sec occurs with all spectra after the first (obtained from metadata files associated with each spectrum). Detector times are used as the time stamps for the experiment. Data collection was initiated before the addition of reaction solution and continued for 10–30 min, depending on the transformation kinetics observed in preliminary experiments. Hence a complete time series might comprise 40–120 spectra. ACC 1a and 1b preliminary experiments were performed to determine the approximate time to 50% completion (50% ACC loss). Durations of 20–30 and 10–15 min were chosen for ACC 1a and 1b experiments, respectively. Durations for ACC 2 experiments (20–30 min) were based on ACC 1a preliminary results due to other experimental similarities (thermal stability, higher pH synthesis, etc.). After data collection began, reaction solution was pushed into the capillary with a syringe to fully wet the sample. The wetting action of the reaction solution was observed with a video camera and quantitatively confirmed with changes in the total scattering pattern consistent with the influx of a fluid (an overall increase in the scattering intensity and change in absorption). A complete list

of experiments performed with reaction solutions and dehydration conditions is given in the Supporting Information Table S **4**.

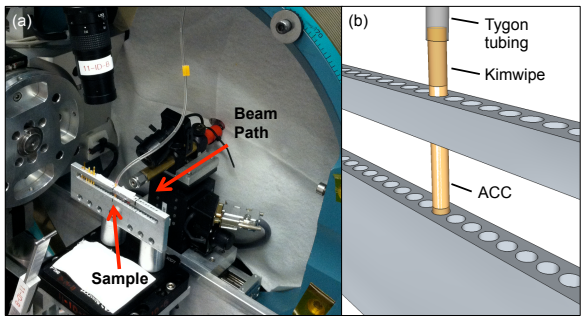

Figure 14. Experimental setup for in situ transformation experiments showing (a) the beam path and multi-sample changer and (b) a close-up schematic of the sample environment.

2.6 Linear combination fitting of time resolved series

Linear combination fitting (LCF) of time series X-ray total scattering data was performed to determine the relative proportion of ACC and different crystalline phases during transformation. The LCF was performed using the program JMP 10 on normalized *I(Q)* data from time-resolved total scattering experiments. Early files in each time series were examined successively for the appearance of scattering from the reaction solution. Initial LCF was performed using five reference samples as end-members: DI water, freshly synthesized ACC, calcite, vaterite, and aragonite. Aragonite contributions were found to be negligible for all experiments. All subsequent LCF analyses were performed with four end-members. The end-member fractions were plotted over the reaction time throughout the experiment. The mineral end-member fractions (excluding water) were also plotted for each experiment.

Reported LCF errors are the calculated root mean squared error (RMSE) for each predicted value. LCF results are shown with these error bars on one phase fraction for simplicity, though the RMSE is the same for all phases. Other errors due to reproducibility are reported for further analysis of transformation rates and phase fractions at given time points. Tests of the appropriateness of LCF methods to ACC transformation are detailed in the Supporting Information (Figure S **15**). Analysis of the goodness of fit is also presented in Supporting Information for experiments with the lowest and highest average calculated RMSE (Figure S **16**).

3. Results

Results are presented first by examining ACC structure and structural changes that occur with transformation followed by linear combination fitting results, which look at the time-resolved transformation. Analysis of the transformation as a whole allows us to compare experimental conditions and ACC type behavior from a kinetic standpoint.

3.1 ACC and crystalline polymorph structure

The primary use of total scattering data is to obtain the pair distribution function, which gives the distribution of interatomic distances weighted by the scattering power of the atom pairs. This requires corrections and normalization for sample composition, followed by Fourier transformation, which we described above. However, we use the normalized intensity data, *I(Q)*, for examining kinetics of ACC transformation, as *I(Q)* requires less data processing. Normalized scattering, *I(Q)* for ACC and DI water (Figure **15**a) show broad peaks that become strongly

damped with increasing *Q*, consistent with their non-crystalline character. ACC patterns exhibit a strong doublet at 2.1/3.0 $Å^{-1}$ and a broader low intensity feature at approximately 5 $Å^{-1}$. The DI pattern shows a broad peak with a shoulder at 1.9 and 2.6 $Å^{-1}$, respectively, with a broader low intensity feature at 4 $Å^{-1}$. While other features are observable in the amorphous *I(Q)* data, they show no distinct differences when comparing ACC samples. In contrast to the amorphous *I(Q)* data, the crystalline phases calcite and vaterite are dominated by sharp, narrow peaks extending beyond 10 $Å^{-1}$. Damping of scattering intensity results primarily from the decrease in X-ray scattering cross-sections with increasing scattering angle. The crystalline patterns exhibit little or no diffuse scattering with the minimum intensity between Bragg peaks near the baseline, as expected for crystalline solids.

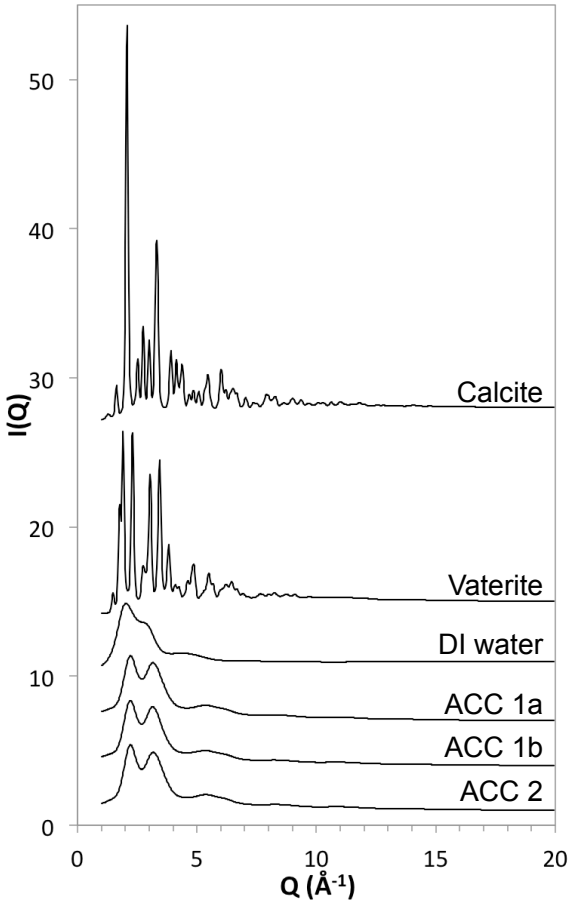

Figure 15. I(Q) function comparisons of ACC samples and standards.

The reduced structure functions, *F(Q)*, for ACC and DI are distinguished by broad, low intensity oscillations, typical of amorphous materials (Figure **16**). The broad, low intensity pair correlations in the pair distribution function (PDF) for DI water attenuate by ~8 Å, also a common observation for amorphous materials.[29] Dampening cutoff distances have been used previously to approximate size of molecular clusters.[9] For the DI water, this distance may represent the ephemeral arrangements formed due to hydrogen bonding. The PDF for DI water is dominated by the nearest neighbor O–O correlation at ~2.8 Å with subsequent broad peaks at 4.4 Å (O–O, O–H, and H–H correlation contributions) and 6.7 Å (O–O and O–H correlation contributions).[127] Pair correlations for ACC attenuate by ~12 Å. The first real correlation for the

ACC PDF is located at 1.3 Å and represents the C–O distance. The peak near 2.4 Å represents the first shell Ca–O distance, with a minor contribution from O–O, and the broader peaks centered at 4 and 6 Å represent a combination of next nearest neighbor pair correlations. A more extensive discussion of ACC structure determined from X-ray total scattering was presented by Michel et al. and further comparison of the three ACC types used here can be found in Schmidt et al. (also see Supporting Information Figure S **17**).[29, 125]

Compared to ACC and DI water, the F(Q) and PDFs for calcite and vaterite exhibit sharper peaks that extend to higher *Q* and *r*, though dampening is evident in PDFs. The *Q*-space resolution of the instrument limits the envelope of observable correlation distances.[128] The first two pair correlations (C–O and Ca–O) found in the ACC PDF are also found in the PDFs of the crystalline polymorphs (Figure **16**).

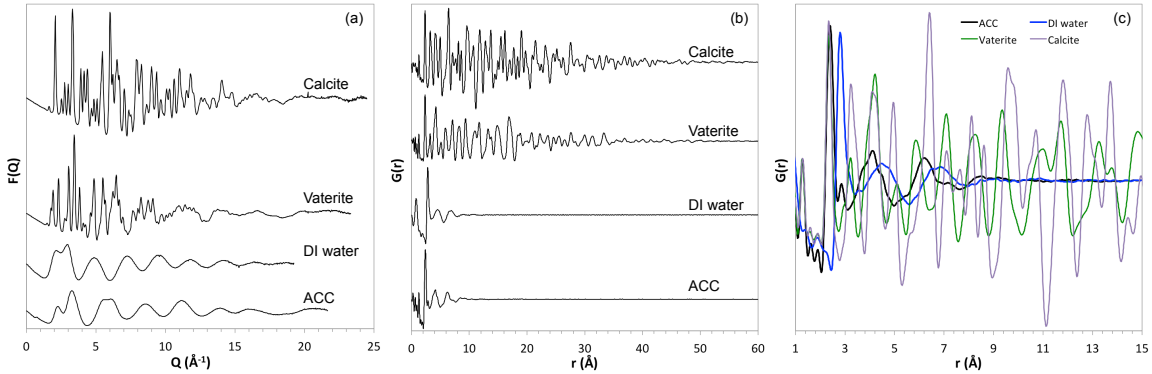

Figure 16. Total scattering results for ACC, DI water, calcite, and vaterite in (a) *F(Q)*, (b) full *G(r)*, and (c) a short *r* range *G(r)* comparison.

3.2 Structural changes during transformation

The rapid total scattering data acquisition allowed in situ characterization of structural changes during transformation, including reaction products, as well as transformation kinetics. Structural snapshots throughout transformation show progressive changes from amorphous dominant to crystalline dominant patterns (Figure **17**). To examine the structural changes that occur throughout the transformation, time points were selected from each time series for comparison of *I(Q)*, *F(Q)* and *G(r)* functions. For ACC 1a, the zero time point and spectra near the t_{25}, t_{50}, and t_{75} points were selected for analysis (representing the time points at which 25, 50, and 75% of the initial ACC has been lost; further discussed in Section 3.2). For ACC 1b, spectra closest to the t_{25}, t_{50}, and t_{75} time points were selected with additional points at 0, 0.8 and 14 min. Since none of the ACC 2 experiments neared completion and few reached the t_{50} or t_{75} time points, three intermediate points were selected. The three experiments shown for example here are the same DI water-reacted experiments shown in Figure **18**, Figure **19**, and Figure **20**.

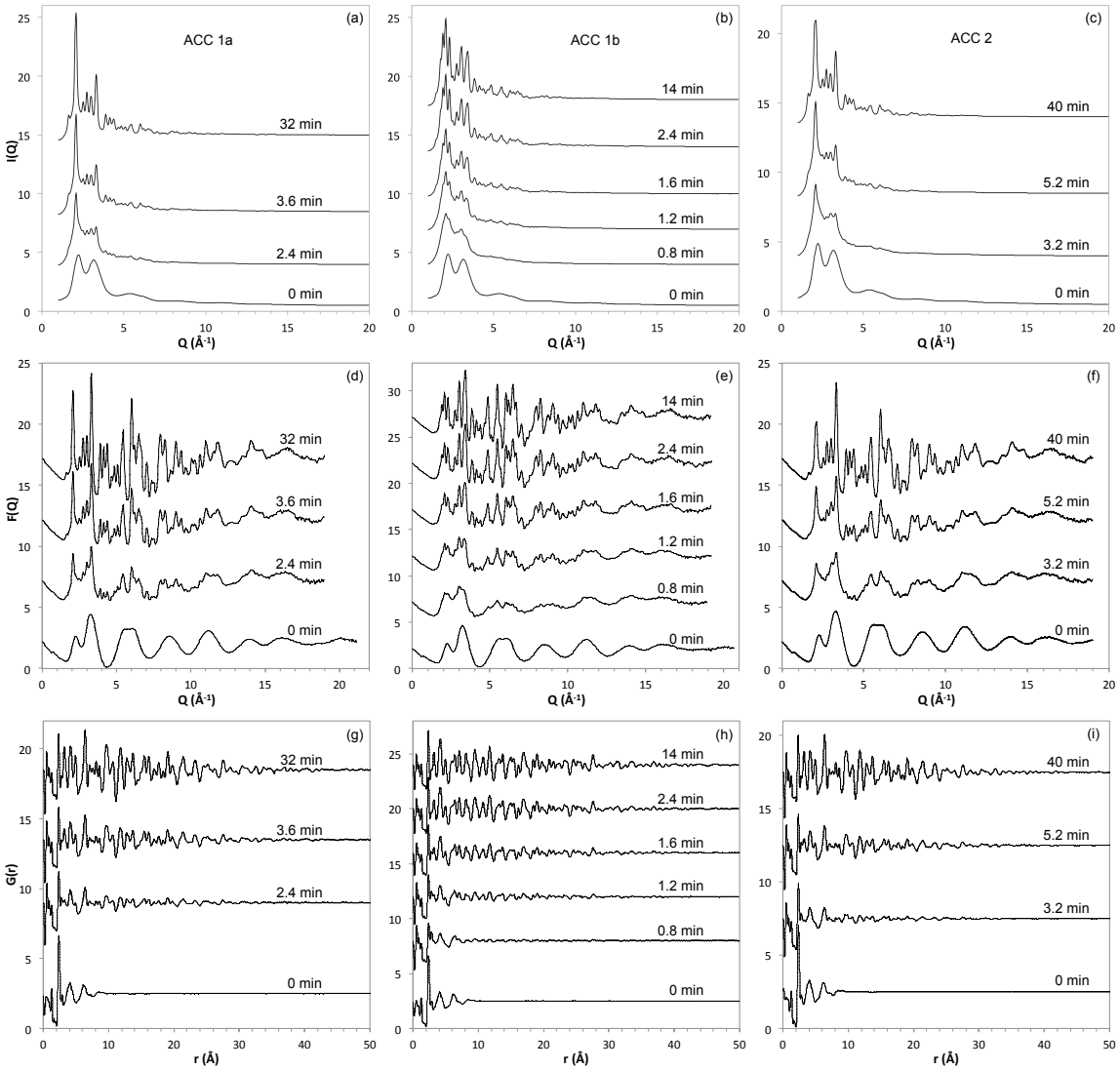

Figure 17. X-ray total scattering results showing I(Q) (top row) *F(Q)* (middle row), and PDF (bottom row) of select time points for (a, d, g) ACC 1a-1.DI, (b, e, h) ACC 1b-4.DI, and (c, f, i) ACC 2-2.DI

The series of *I(Q)* time points throughout the ACC 1a transformation in DI shows a progression from the smooth doublet of fresh ACC to a pattern dominated by sharp crystalline peaks. The smooth features of the zero time point are identical to those described in Section 3.1.The appearance of small, sharp peaks is evidence for the onset of crystallization. An elevated baseline from diffuse scattering remains throughout transformation. ACC 1b and 2 show similar trends, though the extent of crystallization varies at different time points. For example, the dominance by Bragg peaks occurs earlier in the ACC 1b time series compared to 1a and 2. ACC 2 *I(Q)* time points show the slowest development of Bragg peaks amongst the three ACC types.

All three zero time point ACC samples show the same *F(Q)* and *G(r)* features described in Section 3.1. As reaction proceeds, PDFs show an increase in both the number of sharp peaks as well as their appearance at higher *r*, both of which represent the development of long-range order associated with crystallization of calcite and/or vaterite. PDFs for all three synthesis

method ACC samples show a shift in the Ca–O pair distance at ~2.4 Å to lower values as reactions progress. Close inspection shows a shift from 2.39 to 2.35 Å for ACC 1a, 2.40 to 2.36 Å for ACC 1b, and 2.39 to 2.34 Å for ACC 2 (see Supporting Information Figure S **18**). The ACC peak centered at ~6 Å exhibits different trends over the course of the experiments for ACC 1b versus 1a and 2. The ACC, calcite, and vaterite peaks near 6 Å have maxima at 6.20, 6.41, and 5.88 Å, respectively. For the 1a and 2 ACC experiments, the 6.20 Å peaks shift towards the calcite peak distance as time progresses while the ACC 1b experiment peak splits into two peaks at both the calcite and vaterite correlation distances (see Supporting Information Figure S **18**).

3.3 ACC Transformation Kinetics

3.3.1 ACC 1a transformations

Three end-member LCF results plotted in a time sequence provide information on the changing fractions of mineral phases present throughout an experiment (analysis of four end-member fits, including DI water, to look at the behavior of the reacting fluid as it saturates the pore spaces is given in Supporting Information Figure S **19** and Figure S **20**). ACC 1a experiments show that the ACC fraction begins to decrease 0.8–1.2 min after introduction of the reacting fluid with simultaneous formation of calcite (experimental times are based on times recorded by the detector though individual spectra time were 15 sec each; Figure **18**). All time series exhibit an initial rapid loss of the ACC fraction (with simultaneous rapid formation of calcite with minimal to no vaterite formation), followed by a period of slower ACC loss that appears to reach an asymptote. None of the 1a experiments reaches completion, defined here as complete loss of ACC. Although data at long time points were not collected *in situ*, one ACC 1a experiment was set aside and reanalyzed 3 hr after introduction of the reacting fluid (1a-3.Cc; shown with other ACC 1a replicate experiments in Supporting Information Figure S **21**). The long time point showed further loss of ACC and formation of calcite without evidence that the reaction reached completion (22% ACC remaining).

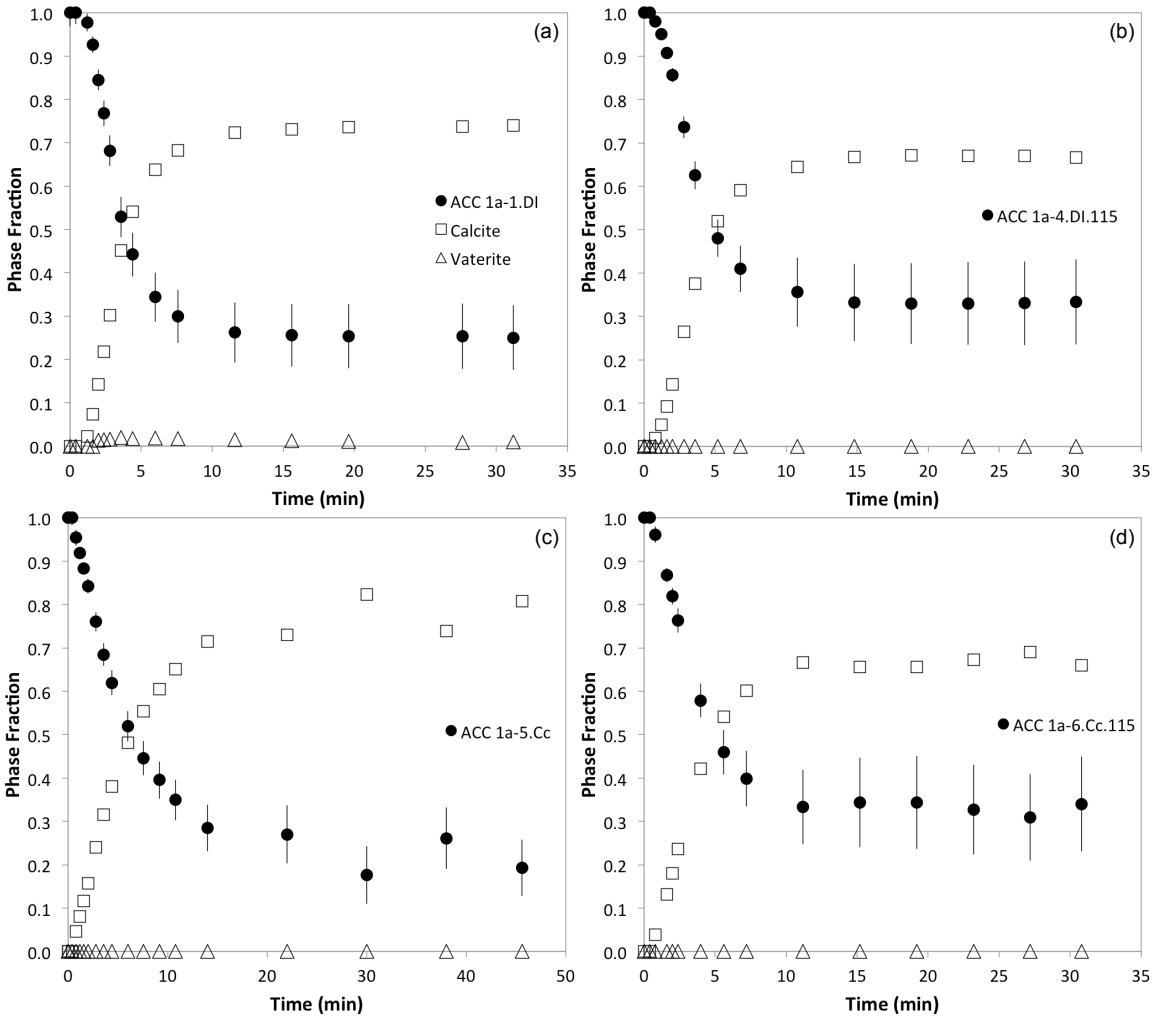

Figure 18. Time series LCF results showing the fractions of phases during in situ transformation of ACC 1a samples. The four time series plotted are (a) fresh ACC 1a reacted in DI water, (b) partially dehydrated ACC 1a (heated to 115 °C) reacted in DI water, (c) fresh ACC 1a reacted in Cc-eq solution, and (d) partially dehydrated ACC (heated to 115 °C) reacted in Cc-eq solution. Error bars, which represent the calculated root mean squared error from LCF fitting, apply to all three phases but are shown only on the ACC fraction for clarity.

Fractional error shown on the figures represents the calculated root mean squared fitting error and does not account for systematic errors. Looking only at fitting error, the vaterite fractions in all 1a experiments are zero. Uncertainty due to reproducibility for 1a experiments also varies with time; early time points in the initial loss of ACC and calcite formation vary from <1 to ~8% difference between replicates. Later time points are less reproducible with differences ranging from 9 to 17% between replicates. Overall, LCF analysis of time-resolved ACC 1a experiments reveals that ACC transforms to calcite with the rate of transformation affected most strongly by composition of the reacting fluid. LCF results for the three replicate 1a experiments are shown in the Supporting Information (Figure S **21**).

Initial transformation rates were calculated by fitting a straight line to the first period of ACC loss. The DI water reacting with fresh ACC experiments show the highest initial rates of ACC loss/calcite formation, approximately 16% change/min (Table **5**). The Cc-eq solution

reacted with fresh ACC produces initial transformation rates of 7% and 11% change/min (for fresh ACC and partially dehydrated ACC, respectively). For DI water experiments on fresh ACC, ACC and calcite fractions plateau at ~9 min. Fresh ACC 1a reacted with Cc-eq solution shows the ACC fraction plateaus at 29 min. For partially dehydrated ACC reacted in DI water or Cc-eq solution, the ACC fraction plateaus at 11–13 min (Table **5**).

Table 5. Transformation experiment summary for ACC 1a.

ACC	Reacting Fluid	Initial Transformation Rate (% change/min)	Time to ACC fraction plateau	ACC fraction at plateau
Fresh	DI water	16	9 min	34%
Fresh	Cc-eq	7	29 min	26%
Part. Dehyd.	DI water	11	13 min	38%
Part. Dehyd.	Cc-eq	11	11 min	34%

3.3.2 ACC 1b transformations

ACC 1b represents the ACC synthesis with the lowest pH and was found to have the greatest overall H_2O content compared to ACC 1a and 2 samples. *In situ* transformation experiment results for ACC 1b reveal behavior that is significantly different than observed for ACC 1a, as vaterite is found to form coevally with calcite. LCF results plotted over time for each set of experimental conditions are shown in Figure **19** (six replicate experiments shown in the Supporting Information, Figure S **22**). The ACC 1b fraction begins to decrease within 0.4–0.8 min after wetting, with simultaneous formation of crystalline polymorphs. In all ten 1b experiments, the first occurrences of vaterite and calcite are observed to be simultaneous within the resolution permitted by the 24-sec data collection intervals. ACC fraction curves first exhibit a steep decline followed by a period of slower ACC fraction loss. Even over the shorter durations of the ACC 1b experiments, many reach or near completion. Of fresh ACC 1b reacted with DI water, 75% of experiments go to completion in <15 min. For fresh ACC 1b reacted with Cc-eq solution and partially dehydrated ACC 1b reacted with DI, 50% of experiments go to completion in <15 min. And for partially dehydrated ACC 1b reacted in Cc-eq solution, no experiments reach completion in <15 min. These results indicate relatively faster kinetics than ACC 1a samples—none of which reached completion over much longer time frames. ACC 1b can also be distinguished by polymorph selection. All experiments show dominant formation of vaterite over calcite, but significant fractions of both persist.

Comparison of replicate experiments reveals high variability in the calcite and vaterite fractions, making further quantitative analysis of limited value (Supporting Information Figure S **23**). Initial transformation rates and vaterite to calcite ratios vary significantly. A qualitative comparison of ACC, calcite, and vaterite fractions over time (Figure S **23**) reveals that experiments reacting fresh ACC with DI water produce the greatest variability, while those reacting fresh ACC with Cc-eq solution are the most reproducible. Neither qualitative nor quantitative comparisons of ACC 1b experiment data reveal clear effects due to partial dehydration or difference in fluid composition; the majority of data are within reproducibility error of the same. Despite difficulties discerning the effects of individual experimental variables, the ACC 1b transformation is distinguishable by relatively fast transformation kinetics and simultaneous transformation to both calcite and vaterite, with dominant vaterite.

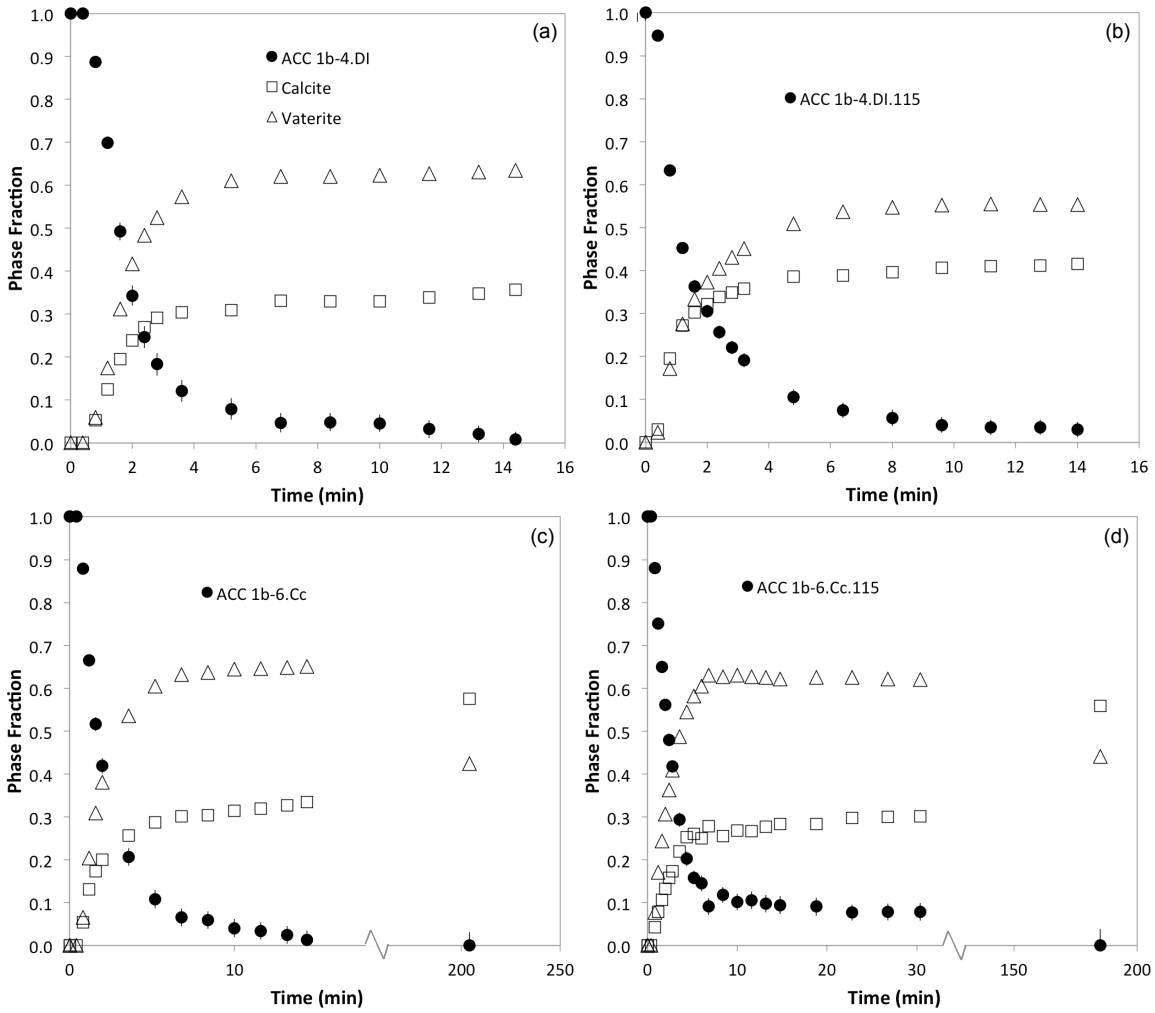

Figure 19. Time series LCF results showing the fractions of phases during in situ transformation of ACC 1b samples. The four time series plotted are (a) fresh ACC reacted in DI water, (b) partially dehydrated ACC (heated to 115 °C) reacted in DI water, (c) fresh ACC reacted in Cc-eq solution, and (d) partially dehydrated ACC (heated to 115 °C) reacted in Cc-eq solution. Error bars, which represent the calculated root mean squared error from LCF fitting, apply to all three phases but are shown only on the ACC fraction for clarity.

Although vaterite dominates in ACC 1b experiments, *ex situ* analyses of samples over extended durations (Figure **19**b and d) reveal a more complicated picture. Most transformations show that vaterite and calcite production appears to level out, as in Figure **19**a and b. Some experiments show a slight decrease in the fraction of vaterite compared to calcite, which is most prominent in experiments 1b-2.DI and 1b-6.Cc.115 though the decrease is only outside of error for 1b-2.DI. This subtle change is made more obvious in long time points where the dominant crystalline polymorph is switched. In 1b experiment long time points, calcite is the dominant crystalline component after ~3 hours of reacting.

3.3.3 ACC 2 transformation

Similar to ACC 1a, synthesis of ACC 2 occurs at high pH, but unlike 1a and 1b samples, the carbonate source for ACC 2 is dimethyl carbonate. LCF results plotted over time for ACC 2

show that the ACC fraction begins to decrease 0.8–1.6 min after the introduction of the reacting fluid with a corresponding simultaneous increase in the calcite fraction (Figure **20**). Initial transformation rates are the highest for fresh ACC 2 reacted with DI water and the slowest for samples reacted with Cc-eq solution (Table **6**). The time required for the ACC fraction to reach a plateau varies significantly from 15 to >44 min (fresh ACC in DI water and fresh ACC in Cc-eq solution, respectively). The range of ACC fractions in the plateau regions also varies, with partially dehydrated ACC reacted in DI water exhibiting the highest remaining ACC fraction, 65%. The Cc-eq solution reacted with fresh ACC may just begin to plateau at the end of the experiment with 35% ACC fraction remaining, but longer experiments are necessary to confirm.

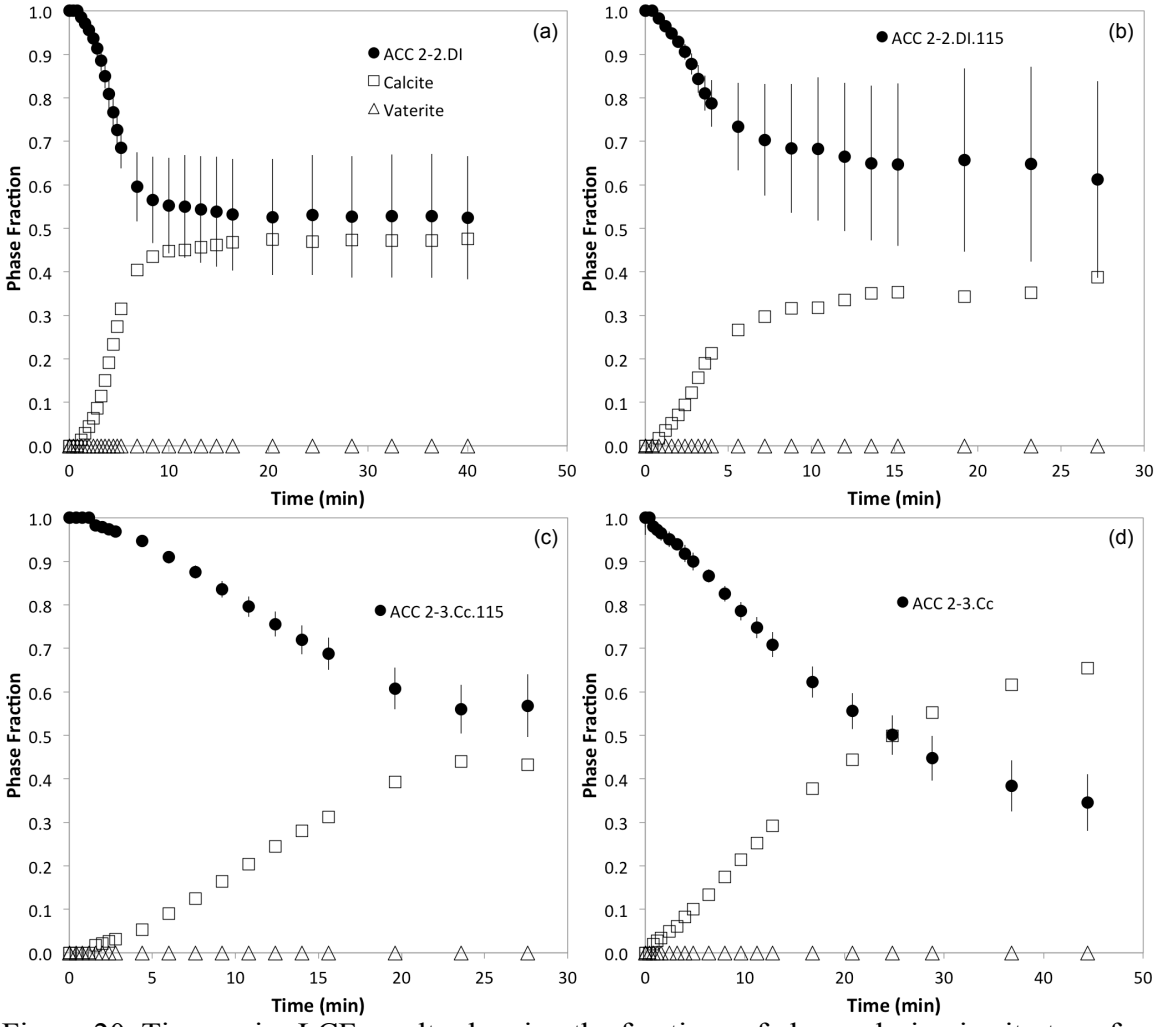

Figure 20. Time series LCF results showing the fractions of phases during in situ transformation of ACC 2 samples. The four times series plotted are (a) fresh ACC reacted in DI water, (b) partially dehydrated ACC (heated to 115 °C) reacted in DI water, (c) fresh ACC reacted in Cc-eq solution, and (d) partially dehydrated ACC (heated to 115 °C) reacted in Cc-eq solution. Error bars, which represent the calculated root mean squared error from LCF fitting, apply to all three phases but are shown only on the ACC fraction for clarity.

Table 6. Transformation experiment summary for ACC 2.

ACC	Reacting Fluid	Initial Transformation Rate (% change/min)	Time to ACC fraction plateau	ACC fraction at plateau
Fresh	DI water	8	15 min	50%
Fresh	Cc-eq	3	>44 min	—
Part. Dehyd.	DI water	6	15 min	65%
Part. Dehyd.	Cc-eq	2	24 min	56%

No ACC 2 experiments reach completion in the 6–44 min time frame. Long time points measured for experiments 2-4.DI, 2-4.Cc, and 2-4.Ccb (Figure S **24**) show that ACC 2 samples reacting for 3–4 hours still contain a comparatively large fraction of un-transformed amorphous phase. The Cc-eq reacted samples reach 18% ACC (3.7 h) and 15% ACC (4 h) while the DI water reacted sample reaches 26% ACC in 4.3 h. No ACC 2 experiments produce measurable vaterite. Time-resolved LCF results reveal slower transformation kinetics for ACC 2 than either 1a or 1b, with transformation exclusively to calcite (four replicate ACC 2 experiments shown in the Supporting Information Figure S **24**). Reaction with Cc-eq solution causes the greatest changes to early transformation kinetics (particularly the initial transformation rate), but the overall fraction of ACC that transforms is greater in the presence of Cc-eq solution than in DI water.

4. Discussion

The time-resolved average bulk structural information provided from *in situ* X-ray total scattering analysis of transforming ACC makes this method ideal for examining the effects of ACC type and reaction conditions on polymorph selection and relative transformation kinetics. Time resolution limits data collection time, making subtle structural analysis of the ACC phase alone impossible due to noise, but the time-resolved phase fraction information obtained through linear combination fitting gives new insights into ACC transformation.

4.1 Comparison of ACC type and relative kinetics

To further examine the reaction kinetics quantitatively, Table **7** summarizes the reaction time for three points in the ACC fractional loss for each experimental condition and ACC type (t_{25} represents the point in the reaction at which 25% of the ACC fraction has been lost, t_{50} when 50% has been lost, and t_{75} when 75% has been lost). The time point loss means corroborate the observed visual differences for ACC 1a and 2 experiments (Figure **21**a), though some changes are within reproducibility error. For ACC 1b experiments, comparison of the DI-aged/fresh ACC experiment means with the Cc-eq reacted/dehydrated ACC experiment means reveals the only distinct changes for the rapid 1b experiments, a slight shift to slower reaction kinetics for all three time points, t_{25}, t_{50}, and t_{75}, outside of error.

Table 7. Summary of variable effects on kinetics due to dehydration and reaction solution. The reported values represent the mean (in the case of multiple experiments), and the listed error is one standard deviation from the mean (0 is reported when multiple values are identical, — is listed if $N = 1$). No data is available for ACC 2 t_{75}.

	Aging Solution	Hydration State	N	t_{25}	t_{50}	t_{75}
ACC 1a	DI	Fresh	2	2.2 ± 0.5	4.0 ± 0.1	27.6 —
	DI	Dehyd.	2	2.9 ± 0.2	5.1 ± 0.1	>30 —
	Cc-eq	Fresh	1	2.8 —	6 —	23.7 —
	Cc-eq	Dehyd.	1	2.4 —	5.0 —	>31 —
ACC 1b	DI	Fresh	4	1.1 ± 0.1	1.9 ± 0.4	3.3 ± 0.8
	DI	Dehyd.	1	0.6 —	1.1 —	2.5 —
	Cc-eq	Fresh	2	1.1 ± 0.1	2.0 ± 0.4	3.5 ± 0.2
	Cc-eq	Dehyd.	3	1.3 ±0.1	2.3 ±0.1	4.1 ±0.2
ACC 2	DI	Fresh	3	4.3 ± 1.4	8.2 ± 1.4	<257 —
	DI	Dehyd.	1	5.1 —	>31 —	— —
	Cc-eq	Fresh	3	7.7 ± 4.9	24.8 —	<222 —
	Cc-eq	Dehyd.	1	12.4 —	>31 —	— —

To summarize the quantitative findings for each set of experimental conditions, use of Cc-eq solution in place of DI water correlates to a decrease in initial transformation rates (observed for fresh ACC 1a and 2, and partially dehydrated ACC2). Substituting Cc-eq solution for DI water also correlates to a decrease in ACC fraction remaining in the plateau period (observed for fresh and partially dehydrated ACC 1a). Partially dehydrated ACC correlates to a decrease in initial transformation rates (observed for ACC 1a in DI water and ACC 2 in Cc-eq solution experiments). However, partial dehydration is correlated with an increase in the remaining ACC fraction in the plateau (observed for ACC 2 reacted in DI water and Cc-eq solution).

As a proxy for reaction progress, ACC fractions versus time were plotted for four representative experiments for each ACC type (Figure **21**). Direct comparison of ACC loss on the same time scale reveals both subtle and dramatic changes resulting from differences in experimental conditions and ACC type (Figure **21**). The effects of the Cc-eq reaction solution and hydration state are subtle in the 1a experiments. Use of Cc-eq reaction solution causes an extension of the transformation progress along the time axis, with a shallower initial ACC loss slope in the Cc-eq solution reaction of fresh ACC 1a. Qualitatively, the kinetic effect is less obvious for the partially dehydrated ACC aged in DI water, but there is a decrease in the initial transformation rate for the partially dehydrated experiments performed in DI water (experiments in Cc-eq solution are within error; Figure **21**b). The Cc-eq solution reaction of partially dehydrated 1a ACC shows what appears to be a mixture of the two behaviors, a more subtle change in ACC loss line shape compared with the Cc-eq solution reaction alone. The fraction ACC remaining in the plateau (slow transformation period) are all within replicate error for ACC 1a experiments.

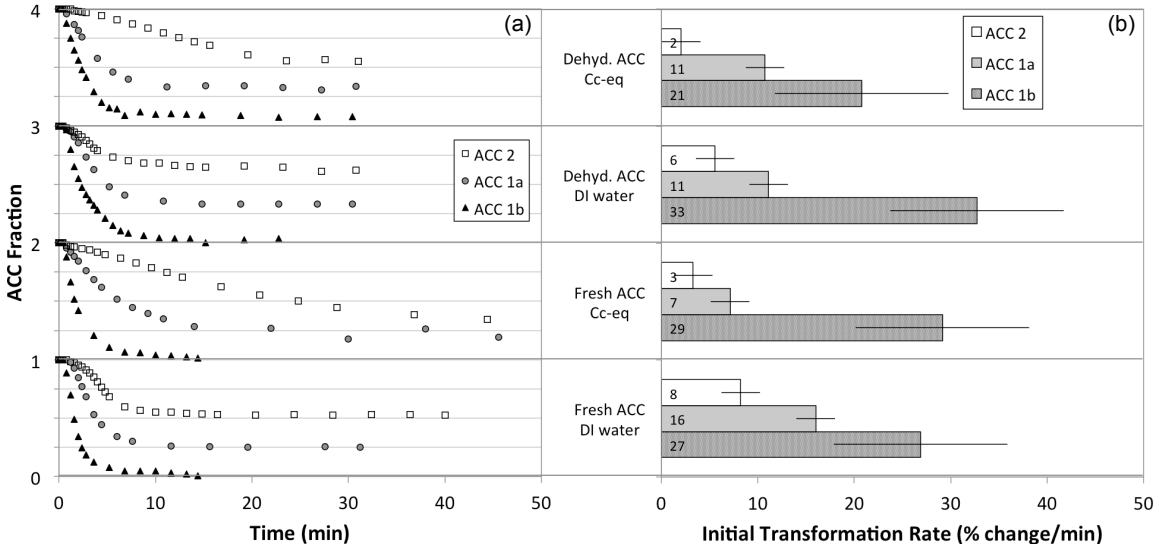

Figure 21. Comparisons of (a) LCF results for each ACC type grouped by experimental conditions with (b) corresponding initial transformation rates. The longest experiments were chosen for comparison. For each ACC type, error bars represent uncertainty due to reproducibility and is an average standard deviation calculated from the standard deviations of replicates for each set of experimental conditions.

ACC 1b experiments under all experimental conditions exhibit nearly identical behaviors, an initial fast decrease in ACC fraction (all within error of the same rate) to near zero ACC fractions followed by slow decrease. Partial dehydration of ACC 1b and/or reaction with Cc-eq solution have no discernable, qualitative effects.

The most dramatic differences are observed for ACC 2 experiments. These experiments show obvious changes to the line shape, decreased initial transformation rates and longer reaction time scales due to both partial dehydration of ACC and use of Cc-eq reaction instead of DI-reaction. Use of Cc-eq solution instead of DI water causes a decrease in initial transformation rates and a decrease in the ACC fraction remaining in the plateau period (though ACC fraction errors make this insignificant). The effects of ACC hydration state are less distinct. For ACC 2, the difference in initial transformation rates of fresh and partially dehydrated ACC in DI water solution are within error, but partially dehydrated ACC 2 reacted in Cc-eq solution exhibits a decrease in initial transformation rates compared to fresh ACC. Partially dehydrated ACC 2 reacted in either DI water or Cc-eq solution correlated to an increase in the ACC fraction remaining in the plateau period compared to fresh, hydrated ACC.

4.2 Polymorph Selection

In the ACC 1b experiments, ACC transforms simultaneously to a calcite and vaterite with dominant vaterite. Using the same synthesis method, Wei et al. also produced this mineral mixture, though their experiments were not designed to determine crystallization order.[58] ACC 1a and 2 samples all transform to calcite with no measurable vaterite. This implies that polymorph selection, in the absence of additives, is dependent on ACC type. Since no significant structural differences among the ACC samples are evident in the total scattering, we infer that polymorph selection is influenced by factors that do not relate solely to the Ca-rich framework of the ACC. Inasmuch as the H atoms are largely insensitive to X-rays, it is plausible that hydrous components, e.g., H_2O, play a role in polymorph selection.

If the H_2O content alone were related to polymorph selection, we could conclude from our experiments that higher H_2O content (similar to ACC 1b, ≥1.6 moles H_2O/mole $CaCO_3$) would lead to formation of calcite/vaterite mixtures, while lower H_2O contents (similar to ACC 1a and 2, ≤1.5 moles H_2O/mole $CaCO_3$) would lead to formation of calcite alone. Yet transformation experiments conducted on partially dehydrated ACC 1b samples (0.8 moles H_2O/mole $CaCO_3$) still yield a mixture of crystalline minerals. Lower hydration states generated by heating do not exhibit any unique correlation with polymorph selection. Although Yoshino et al. were primarily examining the effects of pressure on crystallization, they found an interesting correlation between ACC H_2O content and crystallization products.[97] As H_2O content increased from 10 to 21 wt%, they observed a decrease in the calcite to vaterite ratio.[97] While their synthesis methods and crystallization environments differed from ours, the reported trend corresponds to our observed trend: the sample having the highest H_2O content (ACC1b) transforms to yield the lowest calcite/vaterite ratio.

An alternative explanation could be posited surrounding the relative populations of hydrous components in ACC. In previous work, we have shown that synthetic ACC contains different hydrous components, as determined by NMR spectroscopy.[125] NMR analysis of ACC dehydrated *in situ* was shown to decrease the ACC hydrous populations at slightly different rates (rate of loss of mobile H_2O was slightly greater than rigid H_2O).[125] Since the different hydrous populations likely have distinct structural roles, changes to their relative proportions as well as changes in bond strength of the remaining hydrous components (see section 4.4 discussion of Saharay et al. conclusions[81]) could influence polymorph selection, although a mechanism remains unclear. Other analytical and experimental techniques might prove more useful for determining the mechanism of dehydration-induced polymorph selection.

Several studies have proposed that characteristics reminiscent of the final crystalline transformation products are pre-imprinted on the ACC short-range order as observed by NMR, X-ray absorption spectroscopy, and X-ray total scattering analyses.[35, 96, 112] This idea is disputed by Tester et al. who saw no changes in short-range order in their X-ray absorption spectroscopic analysis of forming and transforming Sr-labeled ACC in sea urchin embryos.[36] Despite the differences in polymorph selection for ACC 1b versus 1a and 2, there are no discernable differences in the short or medium range order in the PDF and spectroscopy data of the three samples (shown in Schmidt et al.).[125] These results, coupled with those presented here, do not support proto-crystalline imprints (Supporting Information Figure S **17**). However, the design of these experiments is not ideally suited to address this contentious issue.

One of the most striking results of the experiments presented here is the simultaneous crystallization of calcite and vaterite in the ACC 1b experiments. Rodriguez-Blanco et al. and Bots et al. found that vaterite formed as the first transformation product when ACC was allowed to react in the synthesis solution. Vaterite subsequently transformed to the more stable calcite over a time frame of minutes to an hour. They concluded that vaterite is a "fundamental" intermediate reaction product in the overall ACC transformation pathway.[24, 79, 129] These in situ transformation studies differ from those in the present study by allowing ACC to react in the same solutions used for their synthesis, whereas we reacted previously formed ACC with two separate solutions.

While the same transformation mechanism(s) are likely at work due to the solution-mediated transformations, the different disequilibrium states for all of these experiments have a strong influence on the transformation. Radha et al. determined the magnitudes of the energetic differences driving crystallization in their experiments.[24] Rodriguez-Blanco et al. concluded that

the relative solubilities of the system ($Log[K_{sp}(Vat)] = -7.913$ and $Log[K_{sp}(Cc)] = -8.480$) govern polymorph selection.[93] In the case of multiple simultaneous transformations, the relative solubilities can only be one factor driving polymorph selection. Combine solubilities and energetic differences in polymorphs with the unclear effects of different hydrous component populations and we begin to see the full complexity of polymorph selection.

4.3 Relative ACC transformation rates

It is necessary to note that there are multiple possible reactions in an ACC transformation: (1) reactions within the ACC, changing its properties (*e.g.* dehydration), (2) the amorphous to crystalline transformation, which includes both ACC dissolution and crystalline nucleation and growth, and (3) the crystalline/crystalline transformation from vaterite to calcite. Any dehydration reactions within ACC (reaction 1) that may occur have no observable affect on LCF results (Supporting Information, Figure S **15**). The short durations of total scattering data collection necessary for kinetic resolution limit identification of possible differences due to dehydration. Reaction 2 represents the bulk of the kinetics discussion in section 4.1, and the crystalline/crystalline reaction (3) is primarily evident in long time point LCF results.[125]

The crystalline/crystalline transformation, reaction (3), has been extensively studied and is understood to be a dissolution/re-precipitation mechanism in solution.[58, 93, 95, 130, 131] The vaterite→calcite transformation occurs on a much slower time scale than the amorphous transformation (25% of ACC contribution lost in 45 sec and 23% of vaterite contribution lost in over 3 hr for ACC 1b), which is comparable to rates reported by other studies .[58, 130] Vaterite dissolution rates, commonly defined as the rate-limiting step in the vaterite to calcite transformation, are strongly affected by the composition of the reaction solutions, pH, temperature, and other factors.[58, 130, 131] The vaterite→calcite transformation observed in the ACC 1b extended time points occurs mainly after complete or near complete loss of the ACC fraction. At earlier stages of the experiment, there are competing mechanisms that contribute to the overall transformation rates (further discussion in Section 4.4).

4.4 Effects of reaction solution and hydration state on ACC transformation

Our findings provide the first evidence of the effects of ACC hydration state and a Cc-eq reacting solution on ACC transformation. These effects are not distinguishable for ACC 1b experiments due to poor reproducibility and relatively fast kinetics, but there are clear trends for both 1a and 2 ACC samples. The effects on both kinetics and the crystalline fraction correlated to partial dehydration of ACC (lower initial transformation rates, increased t_{25}, t_{50}, and t_{75} times, and increase of ACC fraction remaining in the plateau) would indicate a slight increase in resistance to transformation of the ACC with partial dehydration. As mentioned earlier, several studies have proposed that dehydration is a step in the ACC transformation to the anhydrous crystalline form(s).[19, 24, 79, 93]. Radha et al. found calorimetric evidence that anhydrous ACC was less disordered and more stable with respect to calcite than hydrated ACC.[24, 79] Increased stability of the anhydrous ACC could both slow reaction kinetics and preserve the amorphous phase. These changes in ACC stability could relate to changes in bond strength that occur with dehydration. In molecular dynamics studies of ACC dehydration, Saharay et al. found increasing dehydration correlated with an increase in H bond strengths.[81] Increasing dehydration caused an increase in H interactions with carbonate oxygens ($O_C \cdots H - O_W$) compared to water oxygens ($O_W \cdots H - O_W$), which have a weaker interaction.[81] The observed experimental effects might be magnified in future experiments by more significant dehydration prior to transformation.

Many groups have observed that reaction medium plays a significant role in transformation, but no studies have looked at the effects of a calcite-equilibrated solution. The effects of substituting the Cc-eq solution for DI water in experiments (decrease in initial transformation rates and ambiguous results for t_{25}, t_{50}, and t_{75} times and the ACC fraction in the plateau) are driven by disequilibrium conditions. The DI water is highly undersaturated with respect to calcite compared to the Cc-eq solution, which is saturated with respect to calcite and dominated by bicarbonate (at its relatively higher pH of 8.33). The decrease in initial transformation rates in the Cc-eq solution reactions can be explained by a slower dissolution of ACC. The saturated Cc-eq solution, and thus the smaller ion concentration gradient from the ACC surface to solution (compared to DI water), impedes ion diffusion away from the ACC surface (and thus ACC dissolution).[87, 100]

4.5 ACC transformation models

To model the changes in phase fractions for the different time series, the Johnson-Mehl-Avrami (JMA) equation (Eqn. 2) was applied. For ACC 1b, the JMA equation was only applied to the portion of the transformation from initial crystallization until vaterite reaches a maximum fraction, which corresponds to the portion of the experiment dominated by ACC transformation rather than the vaterite→calcite transformation (see Supporting Information Figure S **25** for further analysis of ACC 1b behavior). Log-log plots for ACC 1a, 1b, and 2 reveal non-linear behavior (Supporting Information Figure S **26**). ACC 1b shows the most linear line-shape producing exponent $n = 1.6$, which, assuming diffusion controlled growth, would indicate a decreasing nucleation rate.[132] The JMA model assumes that the growth rate of the crystalline phase is independent of time, which is possibly not the case for these experiments.[133] Looking at Figure **18** through Figure **20**, the transformation rates slow with time. The ACC 1b transformations also appears to slow with time, but the transformation is so quick and the contributions form ACC are so small, that the JMA model is not as sensitive to small changes in the argument.[134]

$$Ln(t) = Ln\left\{Ln\left[\frac{1}{1-\alpha}\right]\right\} \qquad \text{Equation 2}$$

$$\alpha = \left(\frac{X_{CC}}{X_{CC} + X_{ACC}}\right)$$

4.6 ACC structural model

Goodwin et al. developed the only existing ACC structural model from Reverse Monte Carlo simulation based on PDF of synthetic ACC. This model proposes that ACC is comprised of a Ca-rich framework and Ca-poor channels.[30] While the structural data used in the transformation experiments have relatively low structural resolution because of the time resolution requirements, some transformation behavior can be interpreted in light of the Goodwin model. As proposed above, variation in the transformation behavior is partially attributable to different poulations of hydrous components. This is consistent with the model in that the bonding in the Ca-poor channels are dominated by hydrogen bonding. An essential step in the transformation from hydrous ACC to anhydrous calcium carbonate is loss of hydrous components. Different H environments in the three ACC samples studied could lead to variance in transformation behaviors consistent with the Goodwin model.[30]

5. Conclusions

The *in situ* analysis of ACC transformation under various experimental conditions provides unique insights into relative transformation kinetics and polymorph selection. Previous *in situ* studies focused on transformation in the synthesis solution.[35, 79, 93] This left gaps in our understanding of the isolated effects of reaction solution and partial dehydration on undoped ACC transformation. We found that polymorph selection was correlated with both ACC synthesis method and transformation kinetics, which are also linked themselves. Increasing relative transformation kinetics correlated with increasing overall H_2O content. Introducing calcite-saturated reaction solutions promotes the formation of vaterite while partial dehydration promotes calcite formation in ACC 1b experiments. Driving for or departure from equilibrium plays central roles in all of these effects.

Studies of surface charge of ACC in different possible reaction solutions could help us predict what effects cations and anions in solution will have on transformation behavior. An *in situ* analysis of the slow transformation of ACC 2 using NMR may provide more information on possible proto-crystalline structures as well as help determine transformation mechanism. There are still many aspects of ACC stabilization and transformation that remain unclear, but these experiments fill a critical gap in our understanding of this industrially and biologically important material.

Supporting Information

S1. Calculation of compositions used for PDF processing

Compositions at different time points in the ACC transformation were calculated from linear combination fitting results and known compositions of calcium carbonate polymorphs. Parameter estimates are the fractions of known end-members determined to contribute to the unknown sample. The following calculation was used to generate the compositional data in Table S **3**.

$$c = ParameterEstimate(CC)$$
$$v = ParameterEstimate(Vat)$$
$$a = ParameterEstimate(ACC)$$
$$w = ParameterEstimate(DI)$$
$$H = 2w + 2na$$
$$C = c + v + a$$
$$O = 3c + 3v + w + 3a + an$$
$$Ca = c + v + a$$

S2. Analysis of the appropriateness of LCF to the study of ACC transformation

Inherent in the application of LCF methods is the assumption that we know and have pristine data for all of the phases present. While we can identify crystalline phases from Bragg pattern indexing, the amorphous phase(s) presents some ambiguity. Several researchers have proposed anhydrous intermediates in the transformation of ACC to crystalline polymorphs,[79, 129] yet conclusive structural evidence has been lacking. In modeling the dehydration of ACC, Saharay et al. predict changes to short range structure.[81] Schmidt et al. identified small but consistent changes to the ACC structure with dehydration of all three ACC types.[125] This small change, proposed as a slight average decrease in first shell Ca–O coordination number, has negligible effect on the linear combination fitting results. We used two different approaches to confirm that LCF with the available end-members describes the transforming system well. The goal of the first method was to determine if the different water populations of the three ACC types, caused observable differences in LCF fitting. While the hydration states of the three ACC types vary, their total scattering patterns are nearly indistinguishable (see Schmidt et al. comparison of ACC types) so it was expected that substituting ACC end-members would produce negligible differences in the LCF.[125] We performed LCF using three different unreacted, normalized ACC samples as end-members for the ACC1b-4.DI experiment, and there were no discernable differences in the fits with respect to predicted phase fraction or RMSE (results not shown).

The second test compared the LCF effects of using fresh, hydrated versus partially dehydrated ACC 1a as amorphous end-members. A comparison of *I(Q)* shows minor intensity and peak position differences in the 1–7 $Å^{-1}$ range (Figure 5a). All fits utilize the time series data from experiment 1a-1.DI. The first fit uses the fresh, hydrated ACC 1a sample from the 1a-1.DI experiment as the amorphous end-member (Figure 5b). The second fit uses the amorphous end-member from an experiment with partially dehydrated ACC 1a in place of the hydrated ACC (1b-4.DI.115; Figure 5c). The third fit uses both ACC samples (Figure S **15**d).

The LCF results potted over time show the transformation starts with a single phase, ACC. Calcite begins crystallizing at ~1 min. Calcite is rapidly formed while ACC is lost until approximately 10 min when the phase fractions reach a plateau, ~75% calcite and ~25% ACC. Comparison of the hydrated versus partially dehydrated single ACC fits (Figure S **15**b and c)

shows that the phase fractions remain unchanged, but the average RMSE is greater for the partially dehydrated ACC end-member (though the difference is small, ~0.005). Comparing these two fits with the two ACC end-member fit reveals distinct differences. For the two ACC fit, the hydrated ACC fraction approaches zero while the partially dehydrated ACC reaches a plateau of ~45% (~55% calcite). If the primary source of misfit was caused by a missing end-member, addition of the correct end-member would be expected to significantly decrease the average RMSE. However, the average RMSE for the two-ACC fit is not significantly less than for the single hydrated ACC fit. While an anhydrous intermediate ACC may form as ACC transforms and the structural differences between hydrous and partially dehydrated ACC have been observed previously, the use of multiple ACC end-members in LCF are not warranted.[125] Therefore, we conclude that an operational definition of ACC as the unreacted starting experimental material is an appropriate proxy for any amorphous ACC phases present throughout transformation.

S3. Goodness of Fit

To test the goodness of fit for experiments, comparison of selected time points were made on time series data 1b-4.DI. and 2-2.DI.115 (Figure S **16**). These experiments represent the LCF results with the lowest and highest average RMSE, respectively. LCF predicted *I(Q)* data were plotted with measured *I(Q)* data with differences to examine (1) how well the predictions represent the measured data and (2) where in Q-space misfit occurs. As expected based on average RMSE, very little misfit is visible in the 1b-4.DI experiment while significant misfit is apparent for 2-2.DI.115. Greatest differences occur in the low *Q*-range. The misfit in the ACC 2 experiments is characterized by sharp peaks in the difference pattern indicating misfit is due to a crystalline component rather than an amorphous component. This is likely the result of grain size differences. The calcite reference standard is 1.8 um diameter and the vaterite has an unknwn grain size distribution. The change in misfit over time is also likely due to changes in grain size over time due to Ostwald ripening of the nucleated crystallites.

S4. Structure of fresh and transforming ACC

Transformation experiments were conducted on the three ACC types by changing two variables: (1) reaction solution was DI water or Cc-eq solution and (2) the ACC was freshly synthesized or partially dehydrated. The effects of partial dehydration on the structures of these three ACC types were reported previously.[125] Because of the short collection times of the *in situ* total scattering experiments and additional scattering from the reacting solution, the subtle structural differences caused by partial dehydration were not observable. The hydration state and reacting fluid were altered to examine possible effects on reaction kinetics and polymorph selection rather than direct structural effects. For these reasons, only DI water experiments are presented and discussed in a structural context. Comparison of the three unreacted ACC structures are shown in Figure S **17**. Short-range G(r) comparisons of selected time points from a reaction time series of each ACC type are shown in Figure S **17**.

S5. H_2O Behavior in 4 end-member fits

Linear combination fitting results with four end-members show only amorphous phase contributions at the start of experiments, followed immediately by increase in the scattering contribution from DI water, then the crystallizing fraction (described in the main paper in detail). The reaction solutions reach near maximum saturation of the powder within 30 sec for 80 % of

experiments and within 45 sec for 92 % of experiments (Figure S **19** and Figure S **20**). Two experiments exhibit atypical behavior, one with a longer duration before maximum saturation (~2 min to reach saturation) and one with a maximum powder saturation early in the experiment followed by what appears to be slow loss of the reaction solution. These behaviors may imply a lack of back-pressure in the delivery line or possibly a difference in capillary packing. Both experiments with a-typical saturation behaviors and three representative experiments are shown in Figure S **19** and Figure S **20**. The only observable effects of the atypical behavior in the time series LCF plots were slight differences in the ACC loss slopes over short durations. Since these sections of the plots were not used for further quantitative analysis independently of the whole loss curve, the reacting fluid behavior should not affect overall interpretations and conclusions.

S6. Replicate transformation experiments and ACC 1b reproducibility

Replicate experiment transformation data for ACC 1a and 1b are shown in Figure S **21** and Figure S **22**. Extended time points are shown on the same scale with a break indicated. Error is calculate RMSE from the fit calculation. Reproducibility in ACC 1b experiments made quantitative analysis of phase fractions and transformation rates difficult. Overlays of all ACC 1b experiments grouped by phase fraction and vaterite/calcite ratio are shown in Figure S **23**. Figure S **24** shows replicate experiments for ACC 2.

S7. Model application

Application of the JMA model equation to transformation data yielded ambiguous results. The JMA model is most commonly applied to two component systems so two different approaches were used to fit the ACC 1b data (Figure S **25**). Standard application to all three ACC samples are compared in Figure S **26**.

Table S 3. Molar compositions for generation of *in situ* time point *F(Q)* and *G(r)* functions calculated from parameter estimates where *n* is the moles of H_2O/mole $CaCO_3$ for pristine ACC samples from Table 1.

		Molar Composition				Parameter Estimates				
	t (min)	H	C	O	Ca	CC	DI	Vat	ACC	nH_2O
1a-1.DI	0	3	1	4.5	1	0	0	0	1	1.5
	1	2.15	0.50	2.56	0.50	0.107660	0.502031	0.007435	0.380544	1.5
	1.75	1.80	0.48	2.33	0.48	0.215027	0.522825	0.009276	0.251920	1.5
	19	1.43	0.46	2.09	0.46	0.340464	0.542273	0.004252	0.115000	1.5
1b-4.DI	0	3.2	1	4.6	1	0	0	0	1	1.6
	0.5	2.37	0.42	2.46	0.42	0.0225195	0.5832275	0.0252315	0.3765953	1.6
	0.75	2.12	0.46	2.43	0.46	0.0570109	0.5516895	0.0798116	0.3188474	1.6
	1	1.80	0.50	2.41	0.50	0.0979517	0.505402	0.1567631	0.2470638	1.6
	1.5	1.38	0.53	2.27	0.53	0.1422372	0.4797958	0.2554292	0.1302019	1.6
	9	1.00	0.52	2.06	0.52	0.1857704	0.4927305	0.3307031	0.0041981	1.6
2-2.DI	0	2.4	1	4.2	1	0	0	0	1	1.2
	2	2.07	0.55	2.68	0.55	0.0622937	0.4574698	0.0027662	0.4825826	1.2
	3.25	1.84	0.45	2.28	0.45	0.1416748	0.5494183	0.0030836	0.3080788	1.2
	25	1.61	0.47	2.21	0.47	0.2225042	0.5106835	0.0013481	0.2456549	1.2

Table S 4. Experiment list and labels noting experimental conditions. Labels can be read as follows: ACC type-sample#.aging solution.dehydration temperature (if any). Each sample number designates the entire yield from a single synthesis; some were divided into aliquots for multiple experiments.

Label	ACC Type	Reacting Solution	Dehydration Temperature
1a-1.DI	1a	DI water	none
1a-2.DI	1a	DI water	none
1a-3.Ca	1a	Cc-eq solution	none
1a-3.DI.115	1a	DI water	115 °C
1a-4.DI.115	1a	DI water	115 °C
1a-5.Cc	1a	Cc-eq solution	none
1a-6.Cc.115	1a	Cc-eq solution	115 °C
1b-1.DI	1b	DI water	none
1b-2.DI	1b	DI water	none
1b-3.DI	1b	DI water	none
1b-3.DI.115	1b	DI water	115 °C
1b-4.DI	1b	DI water	none
1b-4.DI.115	1b	DI water	115 °C
1b-5.Cc	1b	DI water	none
1b-5.Cc.121	1b	Cc-eq solution	121 °C
1b-6.Cc	1b	Cc-eq solution	none
1b-6.Cc.115	1b	Cc-eq solution	115 °C
2-1.DI	2	DI water	none
2-2.DI	2	DI water	none
2-2.DI.115	2	DI water	115 °C
2-3.Cc	2	Cc-eq solution	none
2-3.Cc.115	2	Cc-eq solution	115 °C
1-4.DI	2	DI water	none
2-4.Cc	2	Cc-eq solution	none
2-4.Ccb	2	Cc-eq solution	none

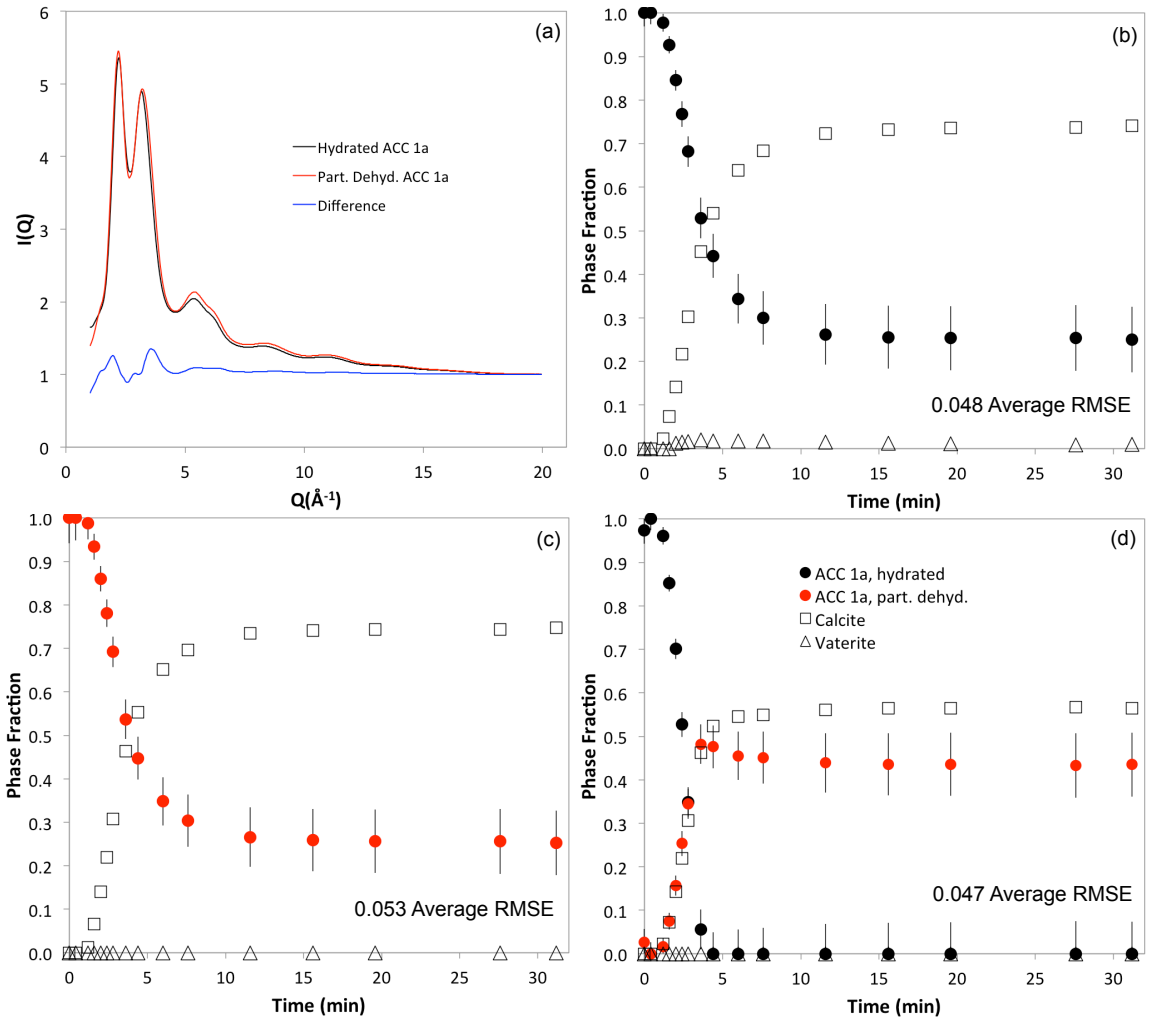

Figure S 15. Results from the tests to determine the effects of ACC hydration on LCF. (a) *I(Q)* comparison of fresh and partially dehydrated ACC 1a with difference are plotted on the same scale. LCF results plotted over reaction time for experiment 1a-1.DI showing (a) a three end-member fit with fresh, hydrated ACC 1a as the amorphous phase, (b) a three end-member fit with a dehydrated ACC 1a as the amorphous phase, and (c) a four end-member fit with both amorphous phases. Error bars apply to all phases but are shown only on ACC end-members for clarity.

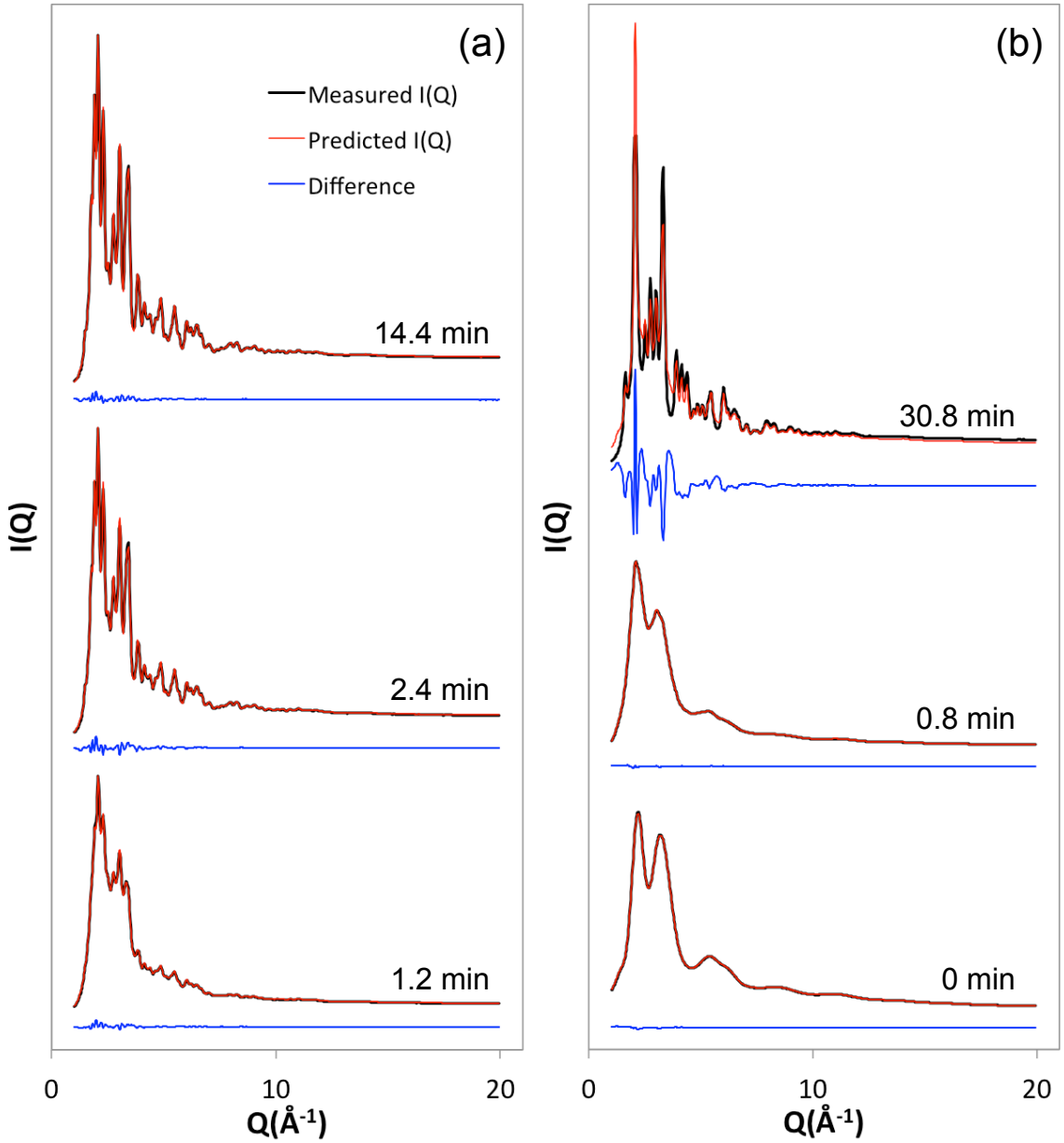

Figure S 16. Analysis of linear combination fits for three time points for (a) the 1b-4.DI and (b) 2-2.DI.115 transformation experiments showing plots of measured and predicted I(Q) with differences. There are arbitrary offsets along the vertical axis, however, the differences are on the same scale as the I(Q) functions. These two experiments were chosen because they had the lowest (ACC 1b) and highest (ACC 2 average root mean squared error of all the transformation experiments.

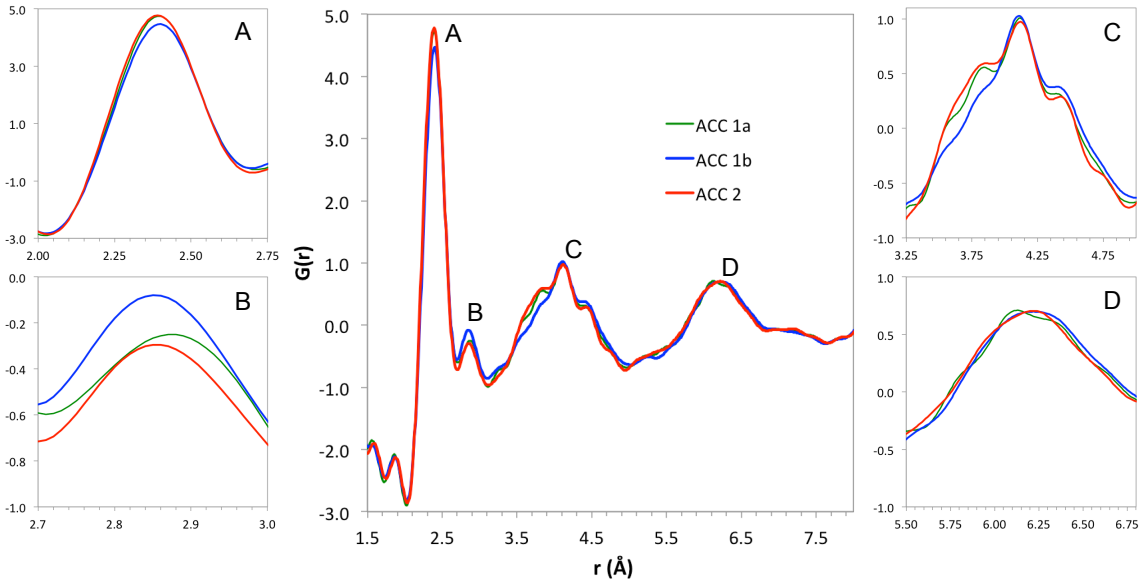

Figure S 17. Detailed study of fresh ACC 1a, 1b, and 2 PDFs with close-up images of four primary ACC pair correlation distances.

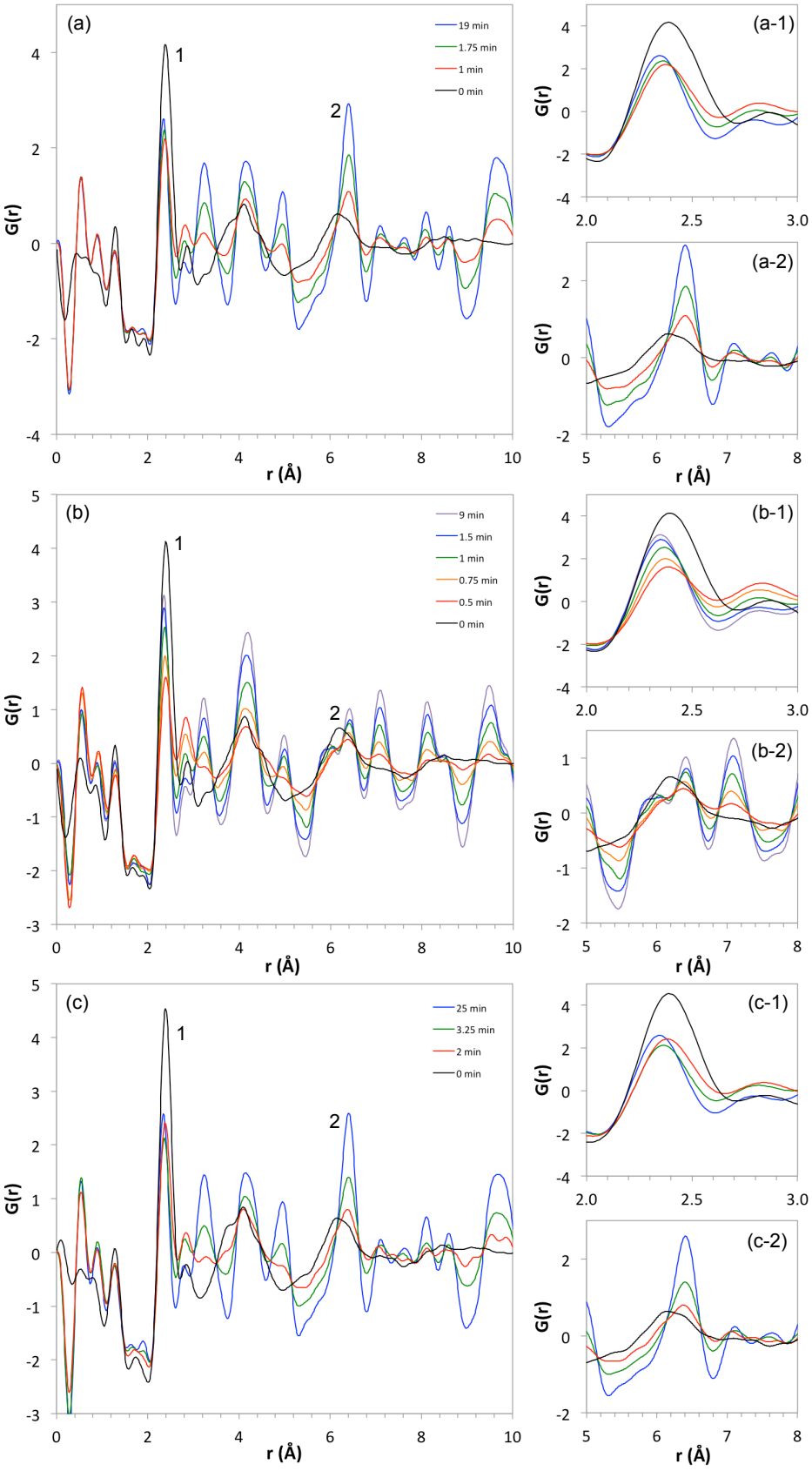
(a)
19 min
1.75 min
1 min
0 min
1
2
G(r)
r (Å)
(a-1)
(a-2)
(b)
9 min
1.5 min
1 min
0.75 min
0.5 min
0 min
(b-1)
(b-2)
(c)
25 min
3.25 min
2 min
0 min
(c-1)
(c-2)

Figure S 18. Short-range G(r) comparisons of overlaid time series data for ACC (a) 1a, (b) 1b, and (c) 2 showing short-*r* range views for two peaks of interest.

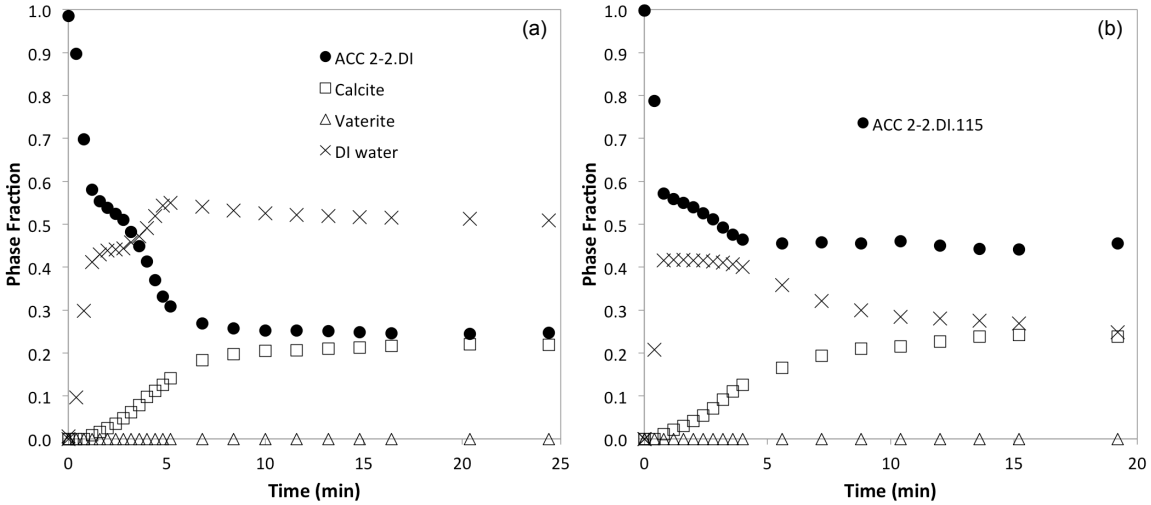

Figure S 19. Four end-member linear combination fit results for the two experiments with atypical saturation behaviors: experiments (a) 2-2.DI and (b) 2-2.DI.115.

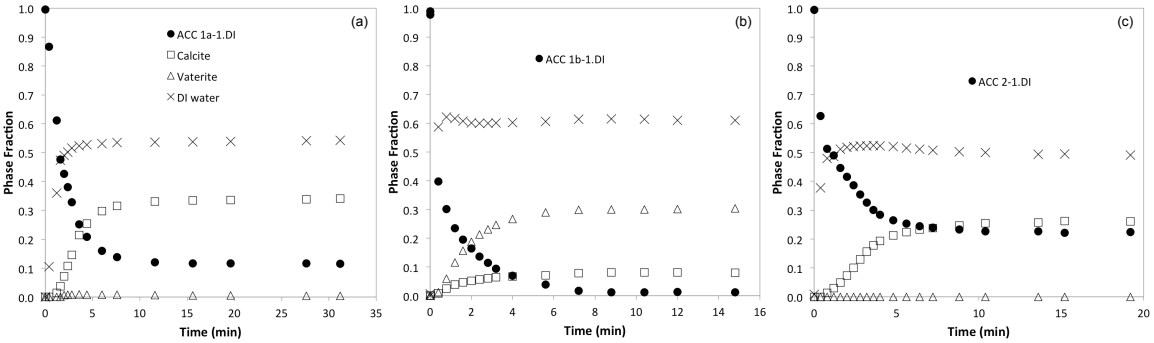

Figure S 20. Four end-member linear combination fit results for three experiments with typical saturation behaviors: experiments (a) 1a-1.DI, (b) 1b-1.DI, and (c) 2-1.DI.

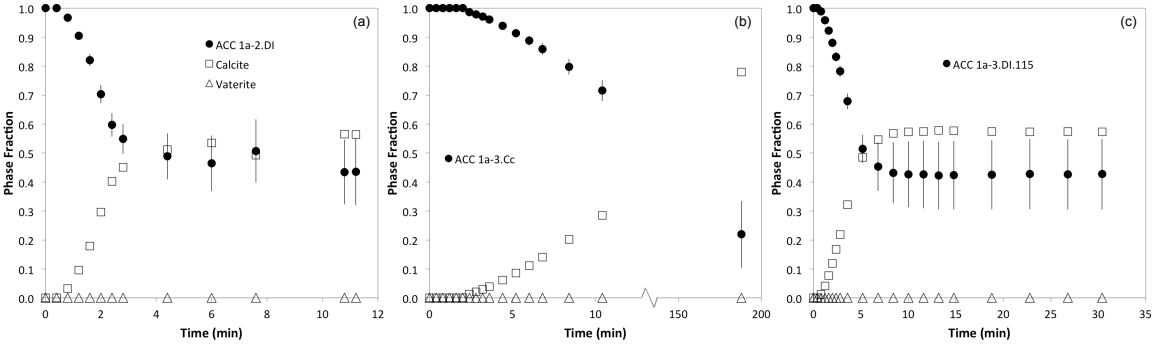

Figure S 21. Time series LCF results showing the fractions of phases during in situ transformation of ACC 1a samples. The three times series plotted are (a) 1a-2.DI (b) 1a-3.Ca,

and (c) 1a-3.DI.115. Phase fraction error bars are the calculated root mean squared error from LCF. Error bars apply to all phases but are shown only on ACC fraction for clarity.

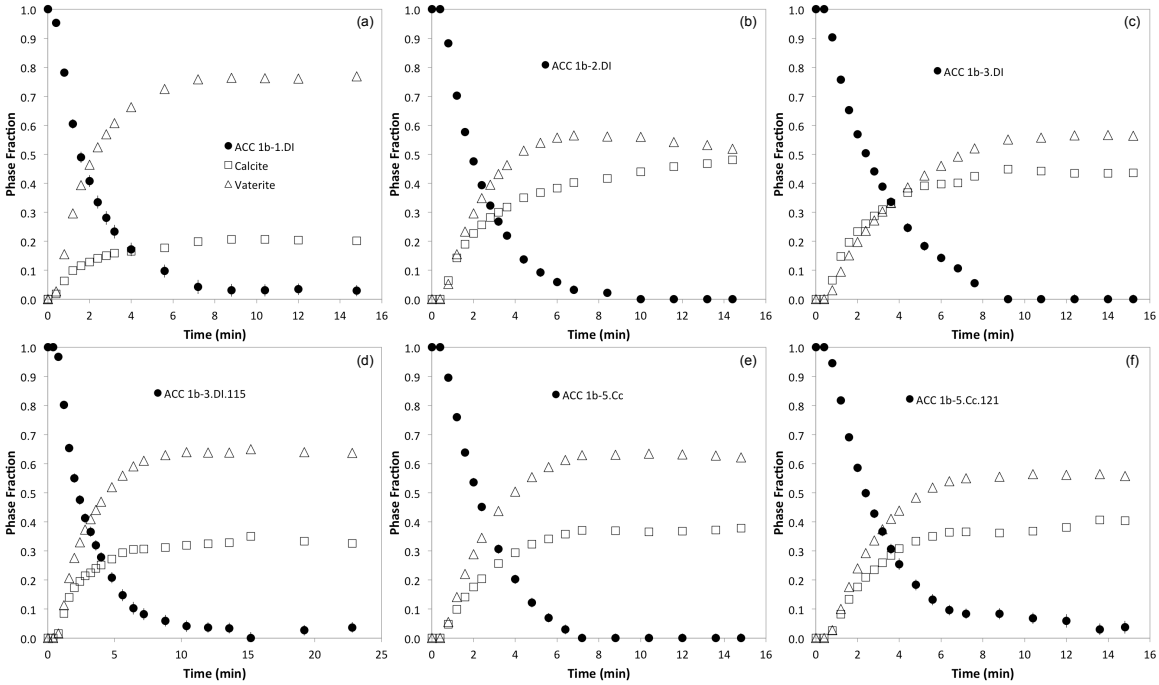

Figure S 22. Time series LCF results showing the fractions of phases during in situ transformation of ACC 1b samples. The three times series plotted are (a) 1b-1.DI, (b) 1b-2.DI, (c) 1b-3.DI, (d) 1b-3.DI.115, (e) 1b-5.Ca, and (f) 1b-5.Ca.121. Phase fraction error bars are the calculated root mean squared error from LCF. Error bars apply to all phases but are shown only on ACC fraction for clarity (some are smaller than the marker).

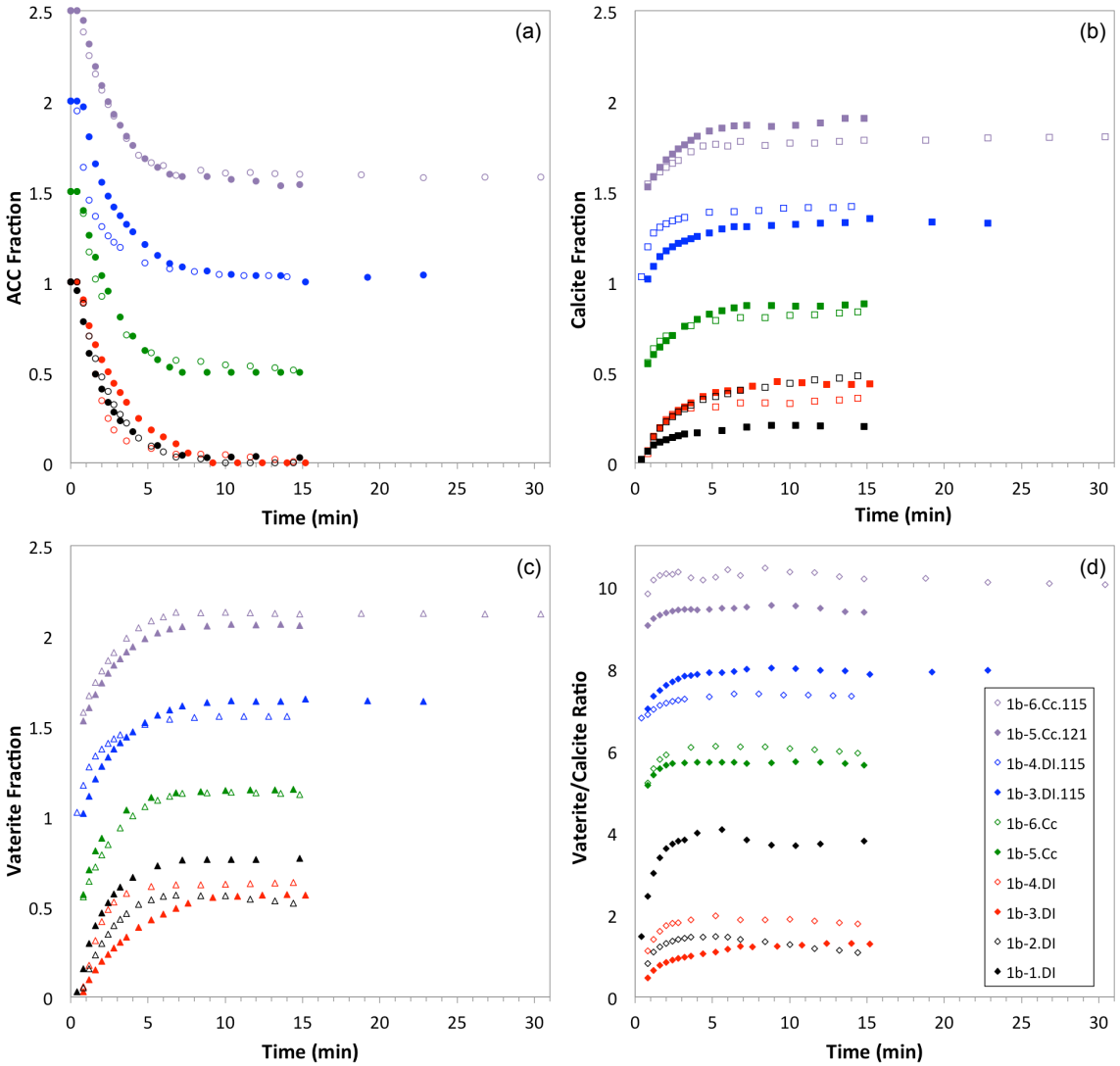

Figure S 23. Qualitative comparison of ACC 1b transformation variability for LCF results plotted over time for all replicates; results are grouped by experimental conditions with arbitrary offsets along the y axis. Plots show (a) ACC fraction, (b) calcite fraction, (c) vaterite fraction, and (d) the vaterite to calcite ratio over the same time axes.

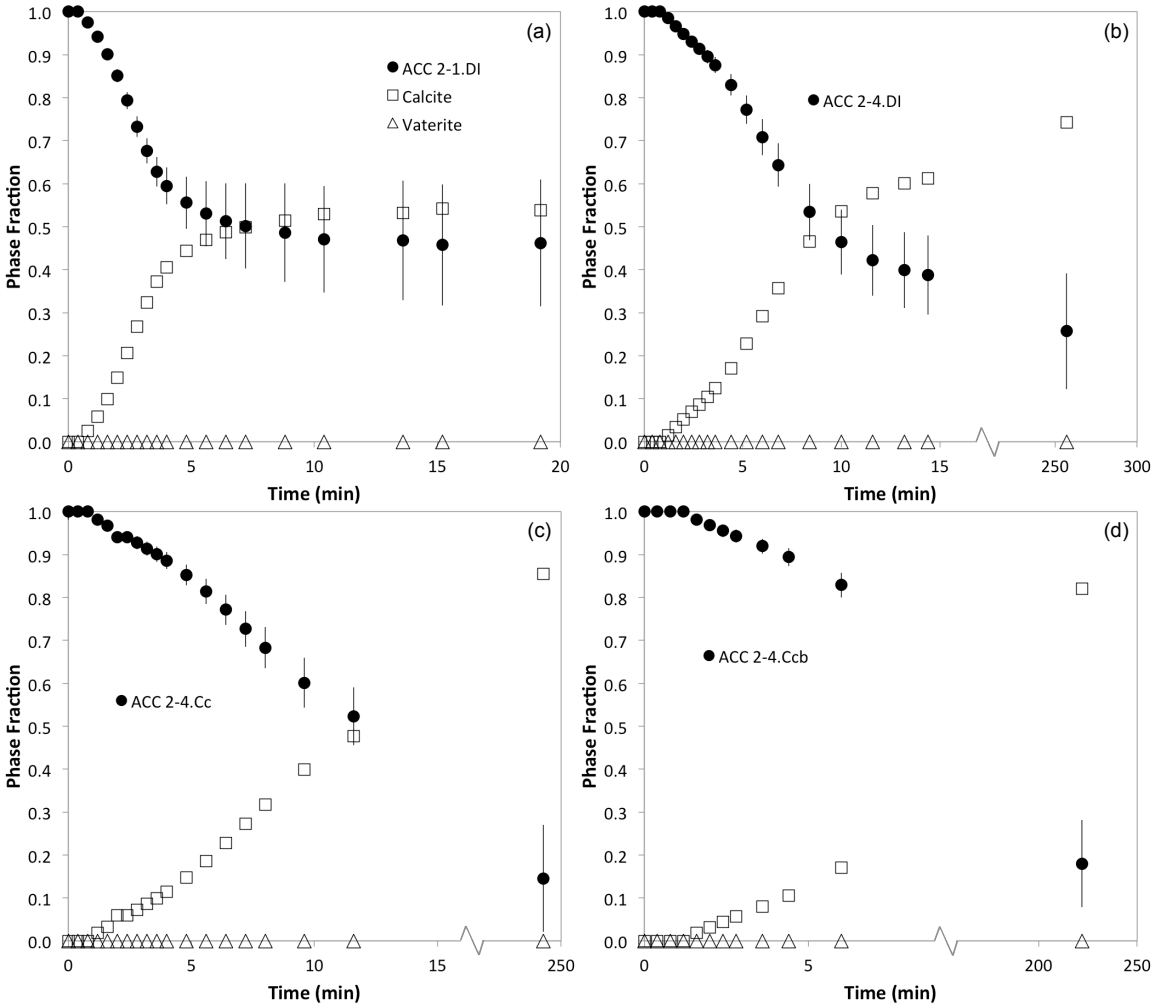

Figure S 24. Time series LCF results showing the fractions of phases during in situ transformation of ACC 2 samples. The three times series plotted are (a) 2-1.DI, (b) 2-4.DI, (c) 2-4.Cc, and (d) 2-4.Ccb. Phase fraction error bars are the calculated root mean squared error from LCF. Error bars apply to all phases but are shown only on ACC fraction for clarity.

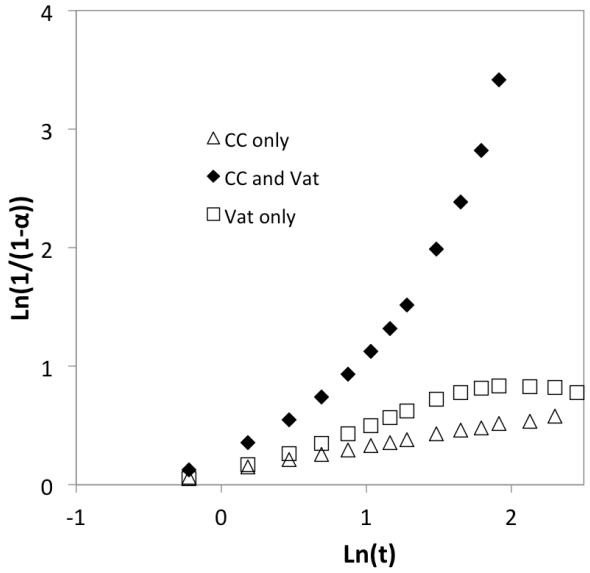

Figure S 25. Application of JMA model to experiment 1b-3.DI showing the divergent behavior treating CC+Vat as the transformed fraction (α) as well as the two polymorphs independently.

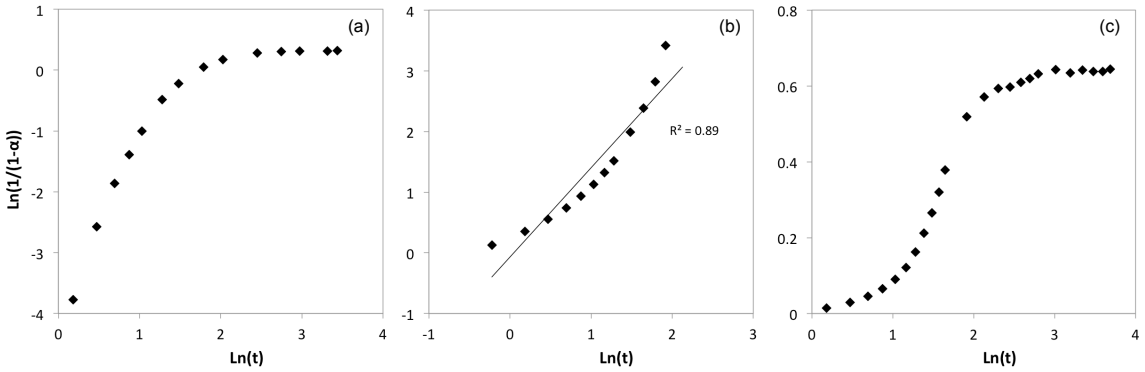

Figure S 26. Application of the Johnson-Mehl-Avrami model to fresh ACC samples aged in DI water for experiments (a) 1a-1.DI, (b) 1b-3.DI, and (c) 2-2.DI.

Chapter 4: Crystallization behavior of biogenic amorphous calcium carbonate: Role of hydration state

ABSTRACT: Amorphous calcium carbonate (ACC) from the gastrolith of the American lobster with different starting hydration states was transformed in DI water. In situ X-ray total scattering measurements provide short and intermediate range structural information throughout the transformation. Using ex situ analyses of amorphous and crystalline standards, linear fits of the time-series data produced a clear picture of the biogenic ACC transformation pathway and the effects of hydration state on polymorph selection and quantitative transformation kinetics. Gastrolith ACC transforms to a mixture of calcite and vaterite with dominant calcite. Dehydration down to 0.5 mole H_2O/mole $CaCO_3$ (starting at 1.4) suppresses vaterite formation and decreases transformation rates compared to hydrated samples. Gastrolith ACC transforms at a slower rate than synthetic ACC with a large amorphous fraction remaining at comparable time points (Chapter 3). Structural comparison of hydrated and partially dehydrated gastrolith shows subtle, but consistent changes indicating a slight decrease in the first shell calcium coordination with increasing dehydration. These results are similar to the experimental structural findings for partially dehydrated synthetic ACC and consistent with molecular dynamics structural predictions. Extended isothermal heating revealed different patterns of H_2O component loss for gastrolith ACC compared to synthetic samples. This result is expected because biogenic ACC has been shown to have two hydrous components compared to the four components of synthetic ACC samples (though one synthetic H component was revealed via an NMR method not applied to LG samples). However, similar to synthetics, there is evidence for kinetically hindered H_2O loss. These findings indicate H_2O directly affects ACC stabilization and transformation and suggests that the distinct structural roles of each hydrous component would likely define the stabilization mechanism for this important component.

1. Introduction

Metastable amorphous calcium carbonate (ACC) is a common transient precursor to crystalline calcium carbonate polymorphs (calcite, vaterite, aragonite). Biogenic ACC, found in worms, plants, and a wide variety of marine organisms,[1, 3] contains varying amounts of magnesium,[16, 18, 21] phosphate,[16, 125] organic macromolecules,[39, 47, 48, 52] and H_2O,[21, 135] which play roles in stabilization, transformation end-products,[7, 14, 136] and morphology/orientation.[123] *In vivo*, ACC serves as transient calcium storage, as a temporary precursor to crystalline structural component, or as a stable structural component throughout an organisms lifetime.[1, 19] During the molting process of some crustaceans, an aggregation of ACC, called gastrolith, forms in a sac in the stomach wall, functioning as calcium storage for the subsequent shell formation.[16, 137] In lobsters, this ACC occurs in relatively large volumes, allowing for a greater variety of analytical techniques than some of the microscopic biogenic occurrences.

X-ray scattering studies have compared the ACC formed in lobster gastrolith (LG) from the *Homerus americanus* with synthetic ACC, revealing only subtle differences in the short and medium range structure (<15 Å).[21] There are, however, notable differences to the H_2O contents, which holds interesting implications for the transformation of hydrated ACC to anhydrous crystalline polymorphs.[21] Biogenic ACC exhibits a range of H_2O contents, from 0 to 1.2 mole H_2O/mole $CaCO_3$.[1, 24] In contrast, synthetic ACC is always hydrated, ranging from 0.33 to 1.6 mole H_2O/mole $CaCO_3$.[1] As determined previously by different NMR spectroscopic experiments, synthetic ACC contains four distinct hydrous components while LG ACC contains only two.[21, 125] The characterization of H_2O components were explored under static conditions, and the effects of H_2O structure on stabilization and transformation are not clear.

Despite much study on both synthetic and biogenic ACC the nature of the amorphous to crystalline transformation mechanism remains unclear, particularly with respect to the possibility of intermediate dehydrated states, polymorph selection controls, and transformation kinetics. Several studies have reported anhydrous biogenic ACC,[23, 24] and several researchers have also proposed an anhydrous intermediate in the transformation pathway of hydrated ACC.[19, 24, 78, 79, 93] Saharay et al. and Raiteri and Gale both reported significant changes in the short-range structure with decreasing hydration in molecular dynamics studies, and Schmidt et al. found experimental evidence for small but consistent structural changes related to dehydration.[81, 82, 125] Gong et al. examined biogenic ACC using X-ray absorption spectroscopy and photoemission emission spectroscopy, and Rodriguez-Blanco et al. analyzed synthetic ACC forming and transforming in the synthesis solution using x-ray diffraction and electron microscopy. Both reported subtle changes they interpreted as the presence of an anhydrous intermediate, but the evidence is not conclusive. However, the effects of hydration state on structural stability and the exact role of these proposed anhydrous intermediates need further exploration.

Radha et al. found significant energetic differences when comparing both synthetic/biogenic samples and samples with different hydration states.[24] Schmidt et al. compared the transformation behaviors of synthetic ACC with different hydration states to isolate the structural effects of H_2O in ACC. In situ X-ray total scattering data were collected for synthetic fresh, hydrated and partially dehydrated ACC samples reacted with DI water and a calcite-equilibrated solution (Chapter 2). They found that partial dehydration caused a slight decrease in transformation rates and an increase in the fraction of ACC remaining during transformation. Similar experiments with a biogenic ACC analog are necessary to further apply these findings to more complex ACC compositions with different hydration states. The described trends would also be more easily observed in slower ACC transformations allowing greater kinetic resolution, which is expected from the report by Reeder et al. that found LG ACC stored at ambient conditions remained amorphous up to a year after harvesting. Synthetic ACC stored under ambient conditions begins to crystalize in a much shorter time frame (~1 month).

In this study, we combined *in situ* and *ex situ* synchrotron X-ray total scattering experiments on fresh and partially dehydrated LG ACC to examine the time-resolved transformation of hydrous, biogenic ACC. These *in situ* and *ex situ* scattering methods allowed us to observe early stages of transformation and obtain information on polymorph selection, relative transformation kinetics, and controls on the transformation pathway. Thermal analyses revealed differences in dehydration behavior and heat-induced transformation behavior. A water loss mechanism is proposed for gastrolith ACC. These findings hold implications for the calcium carbonate mineralization pathway relevant for industrial and biogenic processes.

2. Materials and Methods

2.1 Lobster gastrolith samples

Gastrolith samples were removed from mature American lobsters, *Homerus americanus*, in pre-molt stage and stored in dry ethanol until ready for use. LG was disaggregated, rinsed with dry acetone, and gently ground in a mortar and pestle prior to use. Full characterization of fresh gastrolith ACC is described by Reeder *et al*.[21]

2.2 Reference samples

Reagent grade calcite was obtained from Spectrum Chemical, triple rinsed with deionized (DI) water, and dried at 60 °C for >24 hr. Vaterite was synthesized by mixing 10 mL of 0.4 M

sodium carbonate with 10 mL of 0.4 M calcium chloride.[34,35] The resulting precipitate was stirred for 5 min, vacuum filtered, rinsed with fresh acetone, and dried. Pure synthetic aragonite and DI water were also used as a standard for X-ray total scattering experiments

2.3 Transformation experiments

X-ray total scattering spectra were collected *in situ* and *ex situ* for transformation of ACC to crystalline products. Fresh, acetone-rinsed, and gently ground lobster gastrolith was packed in a 1.29 mm inner diameter Kapton capillary followed by a piece of kimwipe to act as a wick. A micro-pipet was used to add DI water in sufficient amount to saturate the sample. Data collection was started less than 1 minute after the addition of the DI water, and continued for 30 min to 4 hr for in situ experiments. A single scattering spectrum was collected over 1 min. Data transfer and resetting of the detector required 15 sec, so the effective time interval between spectra was 1.25 min.

Long duration transformation time points were obtained from offline reaction experiments. Freshly rinsed and ground LG ACC sample was suspended in DI water and allowed to react at ambient temperature. After ~20 hr, LG sample was filtered, rinsed with acetone and dried under soft vacuum for 5–10 min. Spectra were collected for 5 min and 2 – 3 spectra were averaged. After analysis, the partially reacted sample was re-suspended in fresh DI water and left to react at ambient temperature. After 48 hr of total reaction time, the preparation and analysis process was repeated.

2.4 Dehydration experiments and thermal analysis

Simultaneous thermogravimetric analysis and differential scanning calorimetry (TGA-DSC) was completed on a Netszche Jupiter STA instrument. Approximately 10 mg of sample was loaded into a clean alumina crucible and all experiments were completed under flowing nitrogen. For the basic, dynamic temperature program, sample was heated from 30 to 900 °C at 10 °C/minute. For the extended isothermal scans, sample was heated to 150 °C at 10 °C/minute, maintained at this temperature for 10 hr, and then heated from 150 to 900 °C at 10 °C/minute. To examine the heat-induced transformation behavior of partially dehydrated gastrolith ACC, a series of samples was pre-treated to temperature T in the Netszche instrument (where T was 115, 125, 150, or 200 °C), the furnace was allowed to cool to room temperature, and the partially dehydrated samples were analyzed with the basic, dynamic 30–900 °C heating program described above.

Partial dehydration of gastrolith samples was achieved in two ways: heating and extended exposure to vacuum. Dehydrated by heating was performed using a Lindberg Blue Mechanical Oven (in air) or TGA-DSC, with temperature settings of 115, 150, and 200 °C (at 6 °C/min). Samples heated in the Lindberg Blue Oven weighed before and after heating to determine the fraction of mass lost.

Two gastrolith samples were partially dehydrated by vacuum exposure. Samples were packed in Kapton capillaries and weighed. One sample was placed in a vacuum chamber attached to a roughing pump vacuum chamber for 48 hr. The second sample was placed in a chamber under high vacuum held at 6×10^{-5} mbar for 48 hr. After removal from vacuum, samples were re-weighed, and analyzed within 15 min. The H_2O contents for fresh, hydrated samples were calculated from TGA data (Table **8**). H_2O contents for thermally dehydrated samples were also calculated from TGA data. To calculate initial H_2O contents, mass loss percentages from multiple TGA runs were recorded from 30 to 400 °C using the Netzche

analysis software. The mass loss up to 400 °C was assumed to be all H_2O and used to calculate the initial H_2O content of the lobster gastrolith on a per mole basis. The moles of calcium carbonate were calculated from the remaining mass and assumed to be unaffected by heating.

Table 8. H_2O contents of fresh and partially dehydrated LG samples used in total scattering analyses and *in situ* transformation experiments. Reported uncertainties are based on N=9. There were no replicates for vacuum dehydrated LG samples.

ACC	Dehydration	H_2O Fraction Remaining	Moles H_2O / mole $CaCO_3$
Fresh LG	none	100%	1.45 ± 0.04
LGd-115	heated to 115 °C	66%	0.95 ± 0.06
LGd-150	heated to 150 °C	34%	0.49 ± 0.04
LGv-low	Low vacuum 48 h	98%*	1.4
LGv-high	High vacuum 48 h	62%	0.9

*Reported H_2O fraction lost is within the balance measurement error, ±0.0005 g.

2.5 X-ray total scattering and pair distribution function analysis

Synchrotron X-ray total scattering data were collected at Argonne National Laboratory's Advanced Photon Source at the insertion device beamline 11-ID-B. The incident X-ray energy, 58.X keV (λ = 0.2127 Å), was selected with a Si(311) monochromater, and sample-detector distance and geometry were calibrated using NIST standard cerium dioxide sample (diffraction intensity set: 674a). The 2-D scattering data were collected with a Perkin-Elmer amorphous silicon detector and converted to 1-D with the program Fit2D, which was also used to apply standard corrections.[115]

Intensity data were first transformed to *Q*-space from 2θ to produce *I(Q)* using the program PDFgetX2.[116] Standard and beamline-specific corrections were applied[117], and the H_2O contents calculated from thermal analysis results (Section 2.2.2) were used to constrain the experimental total scattering structure function, *S(Q)*, and the reduced experimental structure function, *F(Q)*. Truncated *F(Q)* data (20–23 Å) were Fourier transformed to produce the pair distribution function (PDF), or *G(r)*.

2.6 Linear combination fitting of time series X-Ray total scattering data

Changes in the relative proportions of phases in time-series data sets were determined using linear combination fitting (LCF) of normalized intensity data, *I(Q)*. (Figure **22**; *F(Q)* and *G(r)* plots shown in Supporting Information, Figure S **27**). Using standard least squares, fitting was performed using four references spectra: calcite, vaterite, DI water, and amorphous gastrolith ACC (dry, prior to addition of DI water). Fitting was initially performed with aragonite as a fifth references spectrum, but aragonite parameter estimates were not statistically significant. After fitting with four end-members, the parameter estimates from calcite, vaterite, and ACC components were combined and the fractional contribution of each was calculated. The water fraction was found to be nearly uniform among samples (discussion of water behavior in Supporting Information, Figure S **28**) and its contribution was subtracted to normalized solid fractions. Each LCF has an associated root mean squared error (RMSE) that is calculated form the misfit between the predicted and the measured *I(Q)*. Linear combination fitting commonly produces near zero and negative parameter estimates when contributions are near a single pure

end-member state, *e.g.* 100% amorphous. A threshold contribution of 0.5% contribution to the *I(Q)* was set based on minimum RMSE; parameter contributions below the threshold were set to zero. The DI water *I(Q)* is most similar to the amorphous *I(Q)* (Figure **22**), though all of the end-members are correlated. Summary of fits for the time series data with the greatest and least misfit are shown in Supporting Information Figure S **29**.

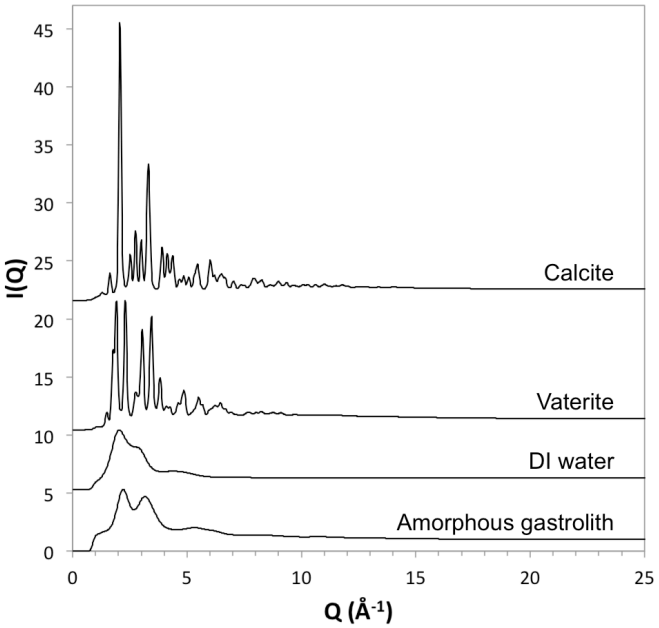

Figure 22. Normalized *I(Q)* comparison of fresh gastrolith, calcite, vaterite, and DI water.

3. Results and Discussion

Results and discussion are addressed from two directions: (1) hydration state and dehydration behavior and (2) the amorphous to crystalline transformation. In each subsection, LG ACC results are presented first followed by comparison to synthetic ACC results.

3.1 LG ACC hydration state and dehydration behavior

In this section, we present TGA-DSC results showing H_2O loss behavior under different heating programs. Combining these results with previously published findings, we propose an H_2O loss pathway. This section also addresses the effects of dehydration on LG ACC thermal stability with proposed implications for the transformation pathway. Finally, this section presents the structural effects of changing hydration state observed with X-ray total scattering methods.

3.1.1 H_2O loss pathway for LG ACC

The TGA curve of fresh LG ACC reveals three primary mass losses (Figure **23**). The first steep mass loss occurs from ~30 through 115 °C followed by a more gradual mass loss from 115 to 300 °C. The final large mass loss begins at ~650 °C. The mass losses correspond to features in the DSC curve: a broad endotherm centered at 120 °C, a small doublet centered at 350 °C, and a strongly endothermic even centered at 800 °C. XRD of patterns taken at intermediate points in the program (indicated by the arrows in Figure **23**) guide interpretation. XRD patterns of fresh gastrolith (not shown) and gastrolith samples heated to 115 (Figure **23** top right panel) and 150 °C (not shown), appear identical and are dominated by a broad doublet centered at 40 °2θ,

indicating no development of long-range order. This indicates that the first endothermic feature of the DSC represents loss of H_2O. The endothermic feature corresponds to the mass loss from 50 to 275 °C in the TG curve. In the DSC, the small exothermic doublet at 350 °C represents transformation to the crystalline phase and is confirmed by XRD of samples heated to 500 °C. Sharp exothermic peaks in the DSC commonly denote crystallization reactions, but the feature may be suppressed by simultaneous reactions involving organic or other inorganic components. Chitin degradation, a two-step process with DSC features at 290 and 360 °C, may contribute to the crystallization doublet.[138] A broad exotherm feature from 450 to 650 °C cannot be fully identified. XRD of gastrolith samples heated to 450 and 650 °C (at the exotherm onset and maximum; not shown) appear identical to the pattern at 500 °C. Lack of change to long-range order suggests this reaction involves light element organic components not essential to the basic Ca-rich framework. The final endothermic reaction and associated mass loss represents the decarbonation reaction that produces calcium oxide. Assuming the average mass loss for LG ACC from 30 to 400 °C is all due to loss of H_2O components, the initial H_2O content of the fresh LG ACC is 1.4 mole H_2O/mol $CaCO_3$. Thermal analysis of fresh, hydrated LG with corresponding XRD patterns of intermediate transformation products (Figure **23**) reveals features similar to those of synthetic ACC samples.[125]

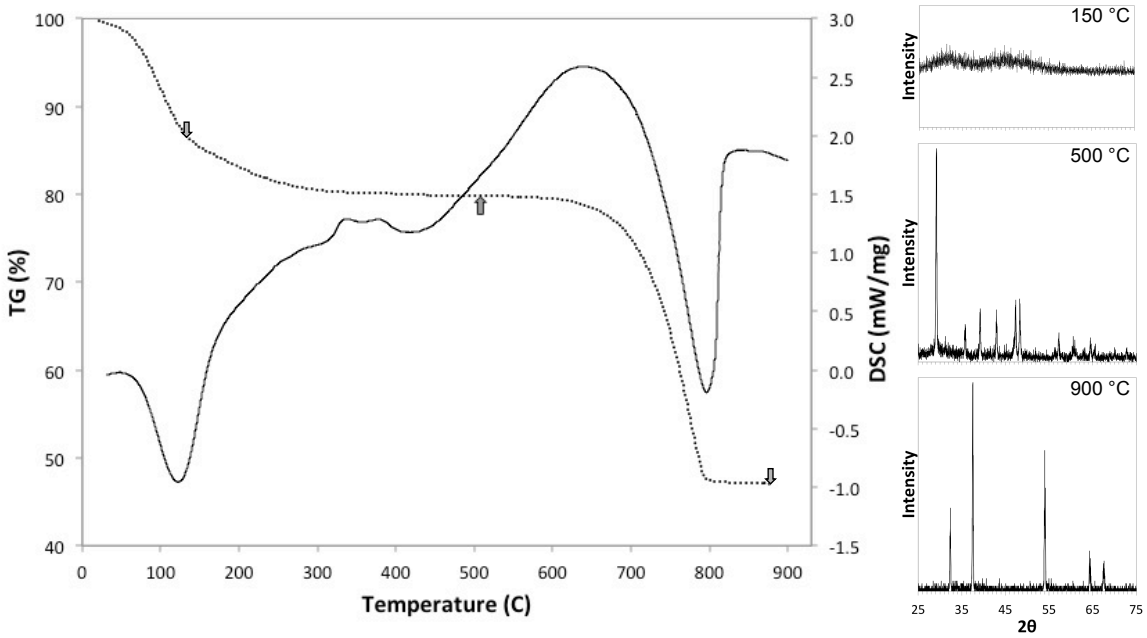

Figure 23. Thermal analysis of fresh, hydrated gastrolith showing TGA (dashed line, left axis) and DSC (solid line, right axis) versus temperature (horizontal axis). Arrows indicate temperatures where runs were interrupted to obtain corresponding XRD patterns showing transformation products to calcite and eventually calcium oxide.

Extended isothermal heating of synthetic ACC samples revealed evidence of kinetic hindrance of H_2O release from the ACC. The same kind of experiments were also conducted on fresh LG ACC samples. Samples were heated dynamically to 150 °C, held isothermally for 10 hr, then heated dynamically to 900 °C at 10 °C/min (Figure **24**). LG ACC samples reveal steep mass loss in the first dynamic regime, slow but steady loss in the isothermal heating regime, and crystallization and decarbonation in the second dynamic heating regime. Up to

15 min, gastrolith ACC loses 78 % by weight of its H_2O. From 15 min to the end of the isothermal regime at 612 min, the ACC loses an additional 11 % of initial H_2O mass. Several sample runs were interrupted at the end of the isothermal regime and analyzed with XRD. Through the entire 600 min of isothermal heating at 150 °C, the LG ACC remained amorphous.

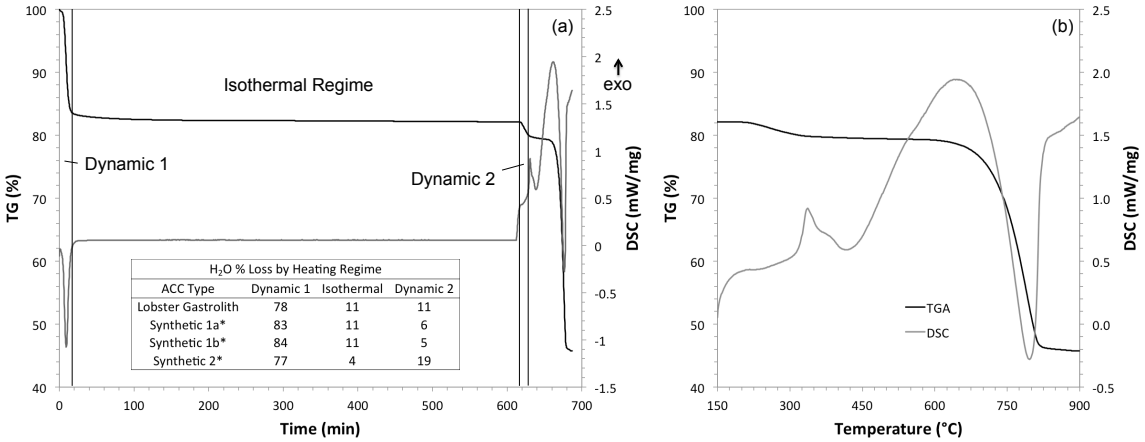

H_2O % Loss by Heating Regime

ACC Type	Dynamic 1	Isothermal	Dynamic 2
Lobster Gastrolith	78	11	11
Synthetic 1a*	83	11	6
Synthetic 1b*	84	11	5
Synthetic 2*	77	4	19

Figure 24. Extended isothermal and dynamic TGA-DSC analysis of a representative gastrolith ACC sample (a) with respect to time for the whole experiment and (b) with respect to temperature for the second dynamic heating regime (150-900 oC). Vertical lines define dynamic and isothermal heating regimes for comparison of H_2O loss for synthetic and gastrolith ACC experiments (inset). Synthetic ACC data from Schmidt et al..[125]

The DSC trace shows a broad endothermic peak associated with initial H_2O loss. Slow continued weight loss occurs in the isothermal regime, with no distinct features in the DSC curve. The exothermic peak centered at 630.5 min (336 °C) represents the crystallization reaction, confirmed with ex situ XRD before and after the exotherm in a replicate experiment. The large broad endotherm starting at ~660 min (630 °C) corresponds to the decarbonation reaction as observed in the basic TGA-DSC experiments.

While there are multiple components in the LG ACC that could potentially contribute to mass loss in the isothermal regime (organic components or inorganic Mg and P), comparison to synthetic ACC results helps narrow down the options. Mass loss in the three synthetic ACC samples cannot be attributed to any organic materials, Mg, or P, yet the mass loss behavior for biogenic and synthetic samples is qualitatively similar. The mass loss in the LG ACC is likely attributable to components they have in common. The only options for synthetic ACC mass loss are H_2O or CO_2. Loss of CO_2 in any appreciable amount would likely affect long-range order. For instance, if the 11% isothermal regime H_2O fraction loss was actually attributed to slow evolution of CO_2 (corresponding to ~2.2% overall mass loss), that would mean decomposition of ~0.1 mole CO_3^{2-}/mole $CaCO_3$. Loss of CO_2 could not be confirmed with ^{13}C NMR data, which showed no significant changes to the carbonate associations but experiments were not in situ. By comparison to synthetic ACC mass loss, behavior and NMR results, we conclude that the mass loss up to the point of crystallization is due to loss of hydrous components. After isothermal heating of LG ACC, another fraction of mass is lost up to crystallization.

There are several possible causes for the final pre-crystallization mass loss: restrictedly mobile H_2O, rigid, structural H_2O, organic/inorganic components, and residue of evaporated acetone from rinsing. Organic and inorganic components cannot be the sole source of the mass

loss because residual mass losses after isothermal heating (second dynamic regime loss) were observed in the three different additive-free, synthetic ACC samples.[125] If the mass loss was due to a residue from rinsing, the three synthetic samples and LG ACC should all show similar mass loss fraction. The mass loss across synthetic and biogenic samples ranges from 1 to 3.8% total mass loss (not % of initial H_2O mass) and replicates show that these residual mass loss range are outside of reproducibility error. This leaves hydrous component(s) or other, unsuspected possibilities. The kinetically hindered loss of these H_2O components (and possibly some small fraction of organic components) may be caused by a physical barrier, like entrapment within pore spaces, as proposed in our previous study.[125]

Extended isothermal experiments on synthetic ACC samples showed that mass was lost in different proportions depending on synthesis method.[125] Comparison of synthetic and gastrolith ACC extended isothermal results (Figure **24** inset) shows that LG H_2O loss is unique compared to synthetic ACC samples. Synthetic ACC samples lose 77–84% H_2O in the first dynamic heating regime with LG ACC losing 78%. In the isothermal regime, LG ACC and two of the synthetics lose 11% compared to 4% loss for the third synthetic sample. At 11% mass loss in the second dynamic regime, LG ACC falls in the range of synthetic ACC loss of 5 to 19%. Based on NMR and extended isothermal experiments, Schmidt et al. suggested that different starting fractions of the various hydrous components cause the different dehydration profiles observed in synthetic ACC.[125] Using NMR, Reeder et al. determined that fresh LG contains two hydrous components, rigid H_2O and restrictedly mobile H_2O.[21] Other studies have reported a range of water contents for biogenic ACC samples so different populations of hydrous components within biogenic ACC structures are likely as well.[3, 16, 20, 22, 78] In conclusion, the H_2O component populations specific to LG ACC and the distinct structural roles of each component contribute to the unique dehydration profile observed in extended isothermal experiments. Extended isothermal heating also reveals evidence for kinetic hindrance of H_2O release (in the isothermal heating regime) in LG ACC similar to synthetic ACC samples.

3.1.2 Dehydration effects on thermal stability

Pre-treatment of gastrolith ACC results in a shift in its mass loss and thermal behavior as determined by TGA-DSC analysis (Figure **25**). For samples heated to 150 °C and below, the shapes of the mass loss curves for dehydrated samples are similar to that for fresh gastrolith but shifted to higher temperatures, with the point of maximum mass loss rate (first derivative minimum) shifting from 127 to 235 °C for fresh ACC and for ACC heated to 200 °C, respectively. For gastrolith heated to 200 °C, the mass loss occurs in two distinct steps, one sharp loss below 40 °C (likely related to adsorbed H_2O) then near zero loss up to 200 where a second slower loss begins. As pre-treatment temperatures increase, these TG changes are associated with diminishing H_2O loss endotherms. The minimum in the dehydration endotherm in the DSC curve shifts to higher temperature (from 121 to 157 °C for fresh gastrolith to sample heated to 150 °C), and the dehydration enthalpy decreases (28.9 kJ mol^{-1} for fresh, hydrated sample to 2.3 kJ mol^{-1} for sample heated to 150 °C to 0 kJ (mole $CaCO_3$)$^{-1}$ for sample heated to 200 °C).

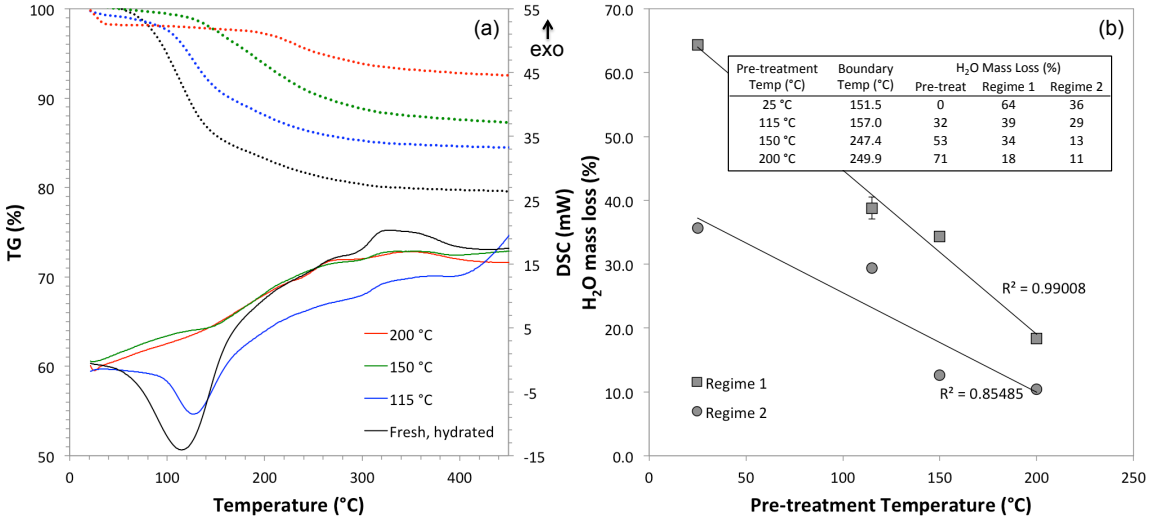

Figure 25. Weight loss and heat flow results for fresh, hydrated gastrolith ACC and gastrolith ACC that was heated at 115, 150, and 200 °C. TGA results (dashed lines) on the left vertical axis, and DSC results (solid lines) on the right vertical axis.

TGA curves were divided into two mass loss regimes before crystallization based on the first derivative. The point at which the mass loss slope changes rapidly (the elbow) is defined as the regime boundary temperature. On the higher temperature side of the regime boundary temperature, the first derivatives approach a plateau at the crystallization temperature. The boundary temperature increases with increasing pre-treatment dehydration (Figure **25**b inset). In other words, the fraction of H_2O lost in early heating decreases with increasing pre-treatment. The H_2O mass loss (calculated assuming total mass loss up to crystallization is water) for each regime reveals a decreasing trend with rapid H_2O loss in regime 1 and slower loss over the broader regime 2. These findings indicate that different hydrous components evolve at different rates and the populations of different hydrous components can be changed (to alter the dehydration profile) with pre-treatment.

Though the gastrolith ACC contains no hydroxyl environment, the H_2O loss regimes observed with TGA-DSC are likely similar to those observed in the NMR studies of synthetic and biogenic ACC described above.[21, 125] In NMR analyses of partially dehydrated synthetic ACC, Schmidt et al. found that rigid, structural H_2O was removed from ACC simultaneously with restrictedly mobile H_2O at similar rates. The rapid mass loss (below 150 °C in Figure **25**a) is likely dominated by loss of restrictedly mobile H_2O and some fraction of rigid structural H_2O. The steady-state loss regime between 150 °C and crystallization is likely dominated by loss of structural H_2O.

Studying the heat-induced transformation of partially dehydrated ACC sheds more light on the contributions of H_2O components to gastrolith ACC transformation behavior. With increasing pre-treatment temperature, the initial H_2O loss endotherm is shifted to higher temperatures, an indication of an increase in thermal stability. Since each hydrous component must have a unique structural role, a change in thermal stability would be expected with changes to the H_2O populations upon dehydration. A decrease in the more loosely bound H_2O and a relative increase in the more tightly bound fraction could cause this shift. The shift could also be caused by communication between the populations of hydrous components, which is evident from NMR of synthetic ACC.[125]

3.1.3 Structural evidence for LG ACC hydration state

The reduced experimental structure function for fresh, hydrated LG ACC exhibits a single beat pattern with broad peaks typical of amorphous materials (Figure **26**).[119] The first *F(Q)* peak at ~2.2 $Å^{-1}$ is indicative of their medium range order.[29] PDFs exhibit short and medium range structure with no atom pair correlations beyond ~12 Å. The two sharpest PDF peaks at ~1.3 Å and 2.4 Å correspond to average C–O and Ca–O bond distances, respectively. Multiple atom–atom average distances are thought to contribute to the next highest amplitude atom pair correlations at 4 and 6 Å (Ca–Ca, Ca–O, and Ca–C, in order of decreasing scattering intensity).

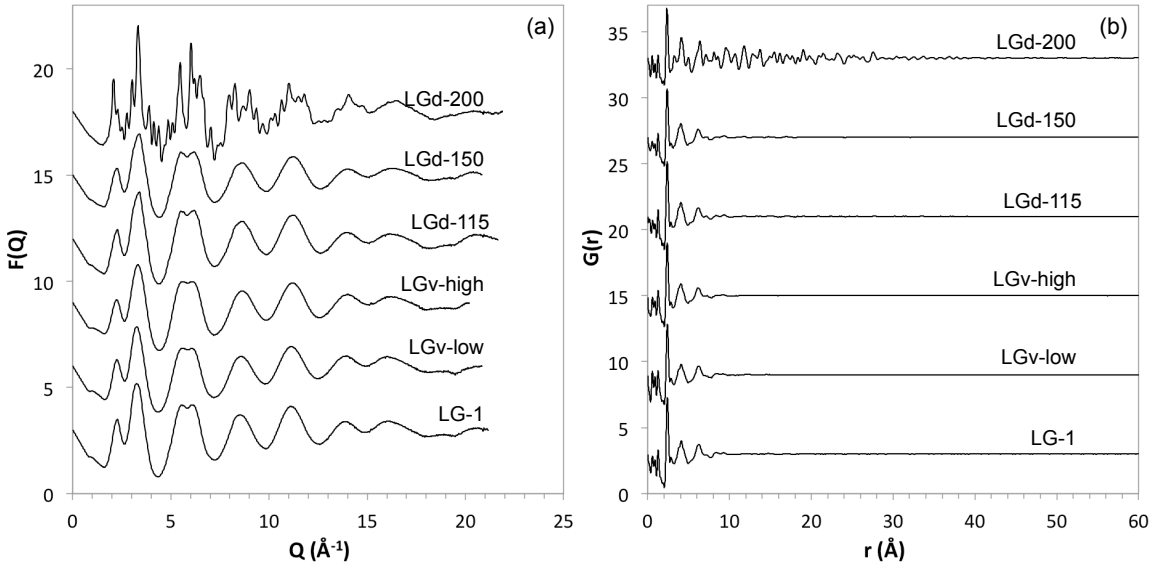

Figure 26. Total scattering comparison of fresh, heat dehydrated, and vacuum dehydrated gastrolith showing results in (a) F(Q) and (b) G(r).

In *F(Q)*, the samples dehydrated by heating to 115 and 150 °C and the samples dehydrated by vacuum appear indistinguishable from one another and the fresh, hydrated gastrolith. Samples placed under low vacuum experienced weight loss (-0.4 %) within measurement error of 0. Samples under high vacuum experienced total weight loss (8 %) similar to heating to 115 °C (Table **8**). As in the *F(Q)* comparison, the vacuum dehydrated samples exhibit no distinguishing PDF features from heat dehydrated samples. Comparison of dehydrated and fresh LG samples shows very subtle differences. The pair correlation maxima of the Ca–O peak exhibits a slight shift to lower *r* and loss of peak intensity for progressively dehydrated samples. The other observable difference between the fully hydrated and partially dehydrated samples is seen most distinctly in the pair correlation at ~2.8 Å, which corresponds to the O–O distance (short r-range comparison in Figure **27**).[127] The peak position shifts for peaks B, C, D (Figure **27**), and the peak centered at ~2.8 Å are small (0.02–0.03 Å), but consistent with reported changes due to dehydration.[125]

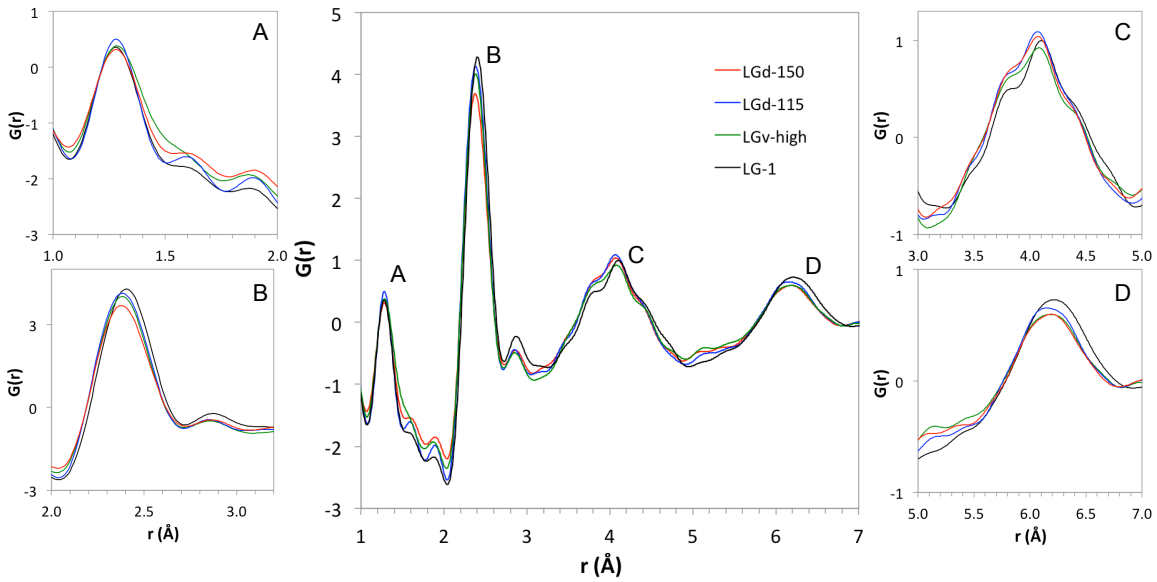

Figure 27. Short *r* range PDF comparison of fresh and vacuum and heat dehydrated LG samples highlighting the four most prominent peaks of the amorphous ACC pattern: the C–O pair correlation at ~1.3 A, the Ca–O correlation at ~2.4 A, and the mixed pair correlations at ~4 and 6 A (primarily contributions from Ca–Ca nearest and next nearest neighbor pairs).

In the sample heated to 200 °C, sharp, narrow peaks at low-*Q* in *F(Q)* are evidence of the onset of crystallization, but the broad peaks that extend to higher Q are evidence that the transformation is only partial.[119] As opposed to the sharp, low-*Q* Bragg peaks, the broad *F(Q)* peaks are caused by diffuse scattering. Under dry, flowing nitrogen, LG does not crystallize until ~350 °C, but the flowing gas in the total scattering experiments was ambient air with significant H_2O vapor content (compared to TGA-DSC experiments), which induced a lower temperature transformation.

The structural features observed with X-ray total scattering of dehydrated LG show minute differences between fresh and partially dehydrated gastrolith ACC. Hydrogen is effectively X-ray transparent, especially in comparison to the X-ray scattering cross sections of other ACC components, C, O, and Ca. The absence of dramatic structural changes in the increasingly dehydrated amorphous samples indicates that the Ca-rich framework of the ACC remains intact. The observed changes are subtle, but consistent with both theoretical and experimental studies of dehydrating ACC samples. In molecular dynamics studies, Saharay et al. predicted changes to the partial and total radial distribution functions (RDF) of ACC as a function of hydration state.[81] Raiteri and Gale predicted similar partial (Ca–Ca) RDF results for the 4 Å peak, but observed different trends for the 6 Å peak, though partial RDFs and total PDFs are not directly comparable and the changes are small for comparable hydration states.[82] Schmidt et al. observed the same trends (peak shifts and intensity differences described above) in experimental X-ray total scattering studies of fresh and partially dehydrated synthetic ACC samples.[125] With the exception of the single 6 Å peak from Raiteri and Gale,[82] all reported experimental and theoretical structural trends are consistent with the results presented here.

3.2 ACC transformation

In this section, we present LG ACC transformation in two ways. The structural view is presented first through analysis of successive X-ray total scattering patterns of transforming LG

ACC. The second view is a time-resolved pathway of the calcium carbonate polymorphs present throughout transformation. The effects of partial dehydration on transformation behavior are also presented. To put these experiments in a broader context, in situ, short duration experiments are compared to longer duration ex situ experiments and biogenic and synthetic ACC transformations are contrasted. Finally, a transformation pathway for dry ACC in DI water is proposed with suggested controls on polymorph selection and kinetics.

3.2.1 Structural analysis of transforming LG ACC

X-ray total scattering structural data is presented for three experiments to compare the transformations of fresh, hydrated LG ACC and samples partially dehydrated to 115 and 150 °C. Transformation experiments were all conducted with DI water as the reacting fluid. Six in situ total scattering transformation experiments and two ex situ experiments were performed (Table **9**). Total scattering data were processed to obtain *I(Q)* functions for further analysis with LCF (discussed in the next section). Unreacted, dry LG *I(Q)* data feature a broad, smooth doublet centered at ~3 $Å^{-1}$ with low intensity, less distinct features up to ~10 $Å^{-1}$ (Figure **28**). Introduction of the reacting solution causes a slight suppression of the second peak of the main doublet, which is most easily observed in the t = 1 min *I(Q)*. As the reactions progress, *I(Q)* data show the progressive development of sharp Bragg features. Even at the longest time points, the *I(Q)* baseline is elevated beneath the Bragg peaks indicating the presence of amorphous material.

Table 9. Transformation experiment list.

Label	Fraction H_2O Remaining	Dehydration Temperature	Max time point
In Situ Experiments			
LG-1	100%	--	240 min
LG-2	100%	--	100 min
LG-3	100%	--	30 min
LG-d115	66%	115 °C	30 min
LG-d115 replicate	66%	115 °C	30 min
LG-d150	34%	150 °C	30 min
Ex Situ Experiments			
LG-A	100%	--	48 hr
LG-B	100%	--	48 hr

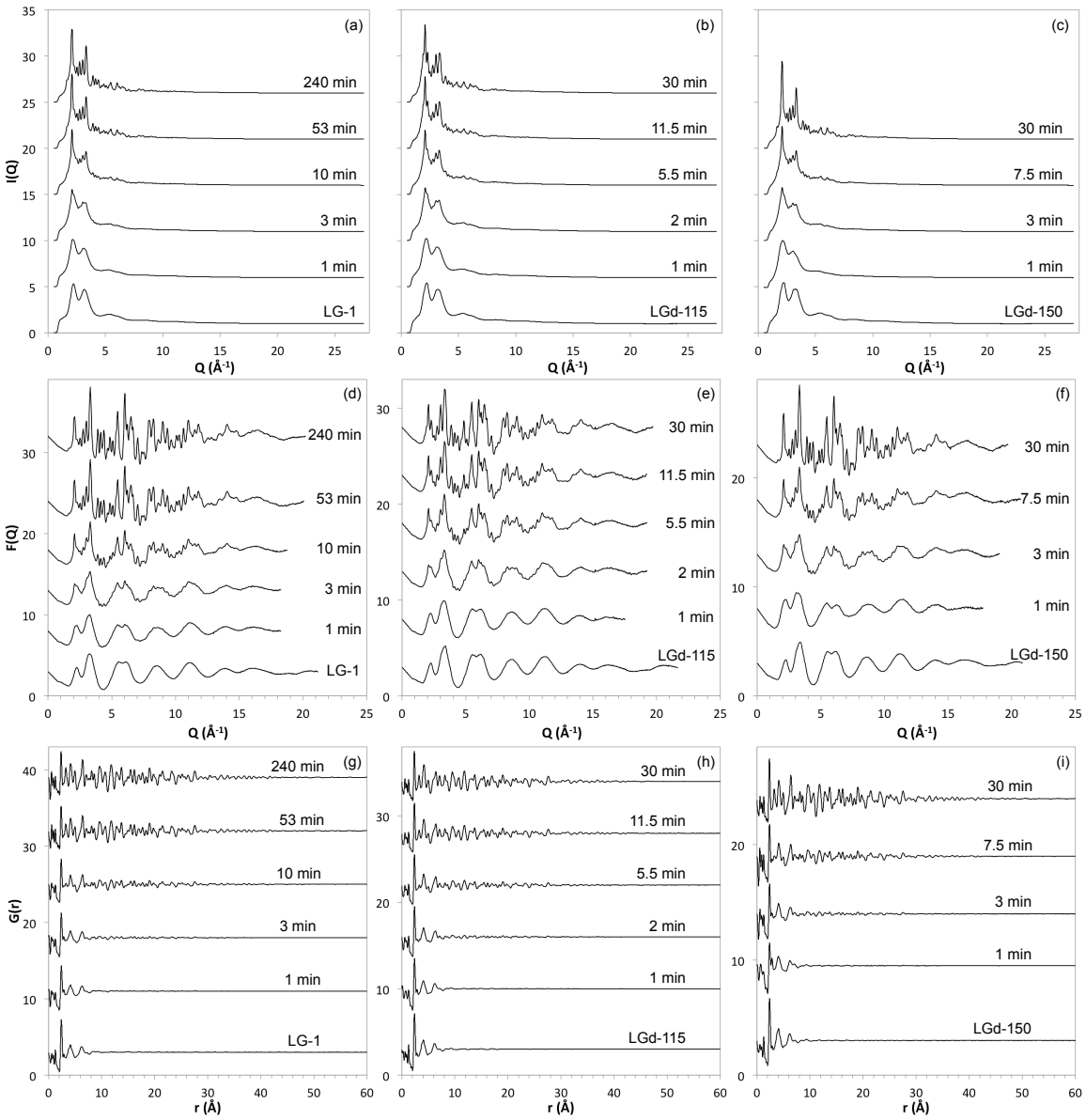

Figure 28. Total scattering results from in situ transformation experiments showing (a-c) *I(Q)*, (d-f) *F(Q)*, and (g-i) *G(r)* plots of select time points from (a, d, g) LG-1, (b, e, h) LGd-115, and (c, f, i) LGd-150. In addition to fresh, unreacted LG patterns, time points correspond to the first minute, the time representing ~5%, 20%, and 40% ACC loss, and the final time point, respectively (from bottom to top in each panel). For the LGd-150 experiment, 40% ACC loss and the final time point coincide.

The reduced structure function shows slight loss of intensity compared to the fresh, dry powder when water enters the system (at t = 1 min time points; Figure **28**). This is consistent with absorption due to water observed in previous in situ H_2O-mediated experiments (Chapter 3). Sharp peaks are first observable in the 2–3 min spectra for all three experiments, indicating the onset of crystallization. The number and intensity of sharp peaks increase as reaction time increases. Pair distribution functions also show subtle evidence for the introduction of the reacting solution, a loss in overall intensity, changes in the lowest r peaks (<2 Å), and a more

pronounced 2.8 Å peak, which was expected due to the O–O nearest neighbor distance in H_2O.[127] As in the F(Q), the first evidence of crystallization is seen in the 2–3 min spectra for all experiments. As time progresses, the number, intensity, and *r*-range of Bragg peaks increase. The differences in the total scattering time series data between the three hydration states is too subtle to observe visually. This time series data is similar to the progressions observed for synthetic ACC samples (Chapter 3; quantitative comparisons are presented and discussed in the next section).

3.2.2 Transformation pathways for fresh and partially dehydrated LG ACC

Linear combination fitting was performed using three reference spectra as described in section 2.6, with resulting phase fractions plotted as a function of reaction time (Figure **29**). The time series results for fresh, gastrolith ACC (Figure **29**a) show initial rapid loss of the ACC fraction with formation of calcite followed 2–6 minutes later by vaterite. After approximately 30 min, the rate of ACC loss slows, approaching an asymptote at ~60% of initial ACC. LG-1, LG-2, and LG-3 experiments (see Table **9**) exhibit a predominance of calcite over vaterite. Differences between replicates (LG-1 to LG-3) are less than 10% over comparable time scales. Even at the longest time points in the LG-1 experiment (4 hr), 55% of gastrolith ACC persists. Other studies of biogenic ACC, samples have seen similar preservation of the amorphous component coexisting with crystalline transformation products.[19]

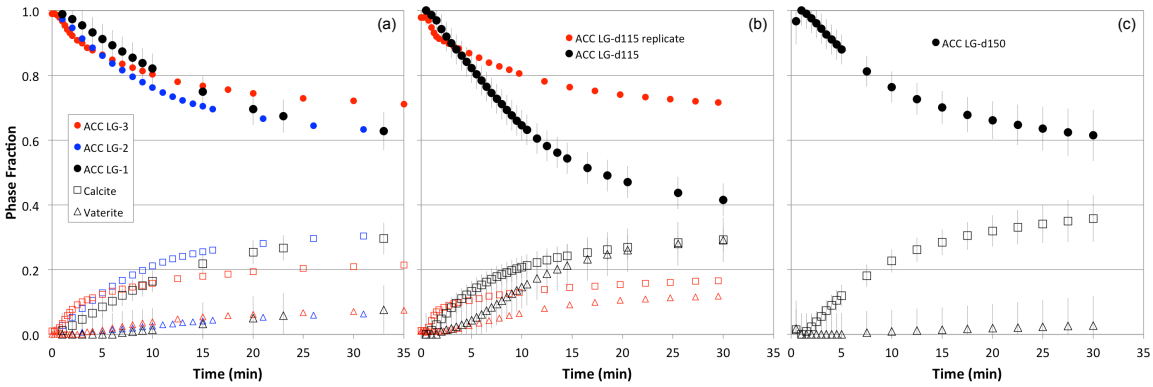

Figure 29. Time-resolved transformation behavior for in situ total scattering experiments showing phase fractions over time for (a) LG-1, (b) LGd-115, and (c) LGd-150. Error bars represent a concatenated root squared error of the root mean squared error calculated from the LCF for each time point and uncertainty based on reproducibility data for each phase (N=12).

In situ transformation experiments on lobster gastrolith ACC samples partially dehydrated by heating to 115 and 150 °C (Figure **29**b and Figure **29**c) reveal incomplete transformation, similar to experiments performed on fresh, hydrated samples. None of the partially dehydrated LG ACC experiments reach an asymptote over the 30 min time scale of observation. In the LG-d115 experiments, calcite and vaterite both form in the first 2 min, while vaterite formation in the LG-d150 experiment lags behind calcite formation by more than 6 min. Reproducibility for the LG-d115 experiments was much worse than for fresh LG experiments. Qualitatively, the LG-d115 experiments show intriguing behavior in the crystalline fractions. Early in the transformations (<10 min), crystalline fractions show a clear lag in vaterite formation compared to calcite. After 10–15 min, both LG-d115 experiments show that the gap

begins to close with equal and near equal calcite and vaterite formation. Transformation of LG ACC partially dehydrated to 150 °C exhibits near complete suppression of the vaterite fraction. More LG sample and more replicates are necessary to fully explore the transformation behavior differences between fresh and partially dehydrated LG ACC samples quantitatively. *Ex situ* experiments would also be necessary to look at the long-term transformation behavior and kinetics.

Because large fractions of the LG ACC persist over the time scales of the in situ experiments, longer time points were obtained from ex situ experiments. The solid to liquid ratios in the two methods represent the only difference. Ex situ experiment samples were reacted with ~2.5 mL of DI water rather than the ~20 µL used in the in situ experiments (for the same mass of sample). The solid/liquid ratios have the potential to affects kinetics due to differences in diffusion and saturation in the reaction fluid, but qualitative comparison of overall trends is still reasonable. Comparison of in situ and ex situ transformations show continued loss of ACC, with a lower limit of ~20% remaining at 48 hr (Figure **30**). The calcite fraction increases to greater than 60% while the vaterite fraction shows minimal change.

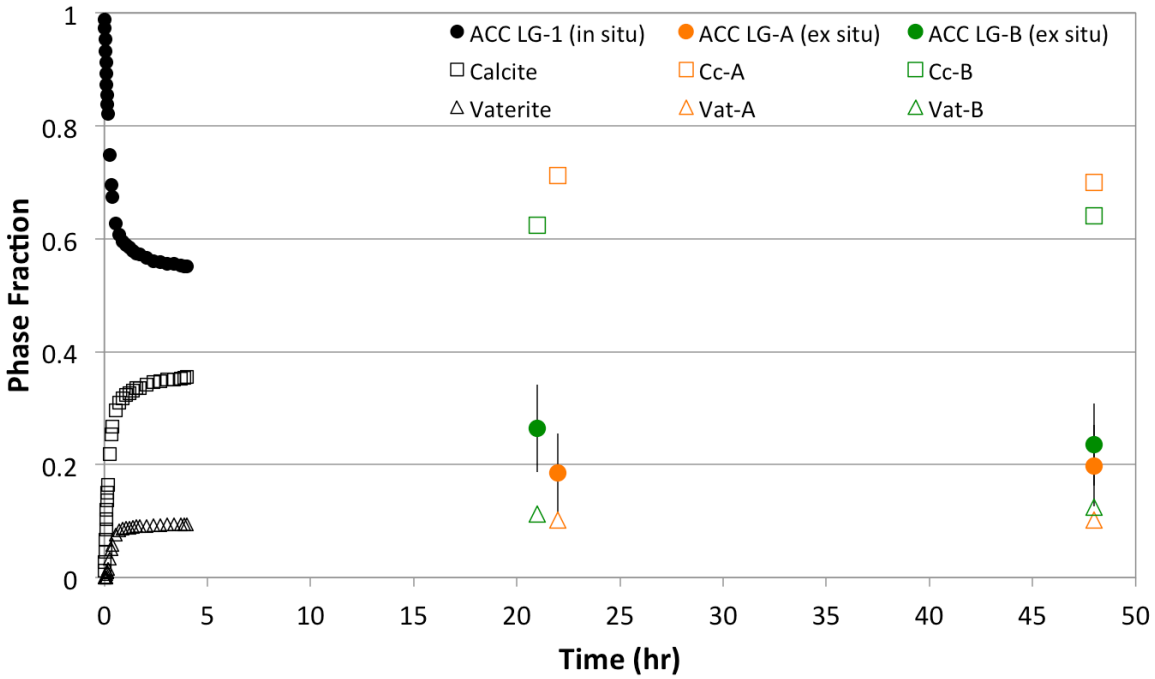

Figure 30. Comparison of time-resolved transformation behavior for in situ and ex situ experimental series showing the LG-1 in situ time series on the same time scale as two ex situ DI water reaction experiments.

It is expected that even longer time points would begin to show transformation from metastable vaterite to calcite as was observed in synthetic transformation experiments (Chapter 3). Evidence for the vaterite to calcite transformation in the synthetic ACC experiments was observed in 3–4 hr time points. However, all ACC transformed to crystalline phases in <30 min in synthetic ACC experiments compared to these gastrolith experiments where the LG ACC is still present and transforming at 48 hr.

3.2.3 Synthetic versus biogenic transformation pathways

The synthetic and biogenic ACC samples contain different overall starting H_2O contents (Table **8** and Chapter 2 Table **1**).[125] Direct comparison of fresh, hydrated synthetic and biogenic ACC transformation on the same time scale shows ACC loss is slowest for LG ACC (Figure **31**). As a result the LG ACC shows the highest fraction of amorphous material at the 30 min time point with ACC 1b nearly reaching completion in 15 min. After LG ACC, ACC 2 exhibits the greatest resistance to transformation and the slowest kinetics of the synthetic ACC samples. LG ACC forms a similar calcite fraction to ACC 1b. While ACC 1a and 2 form no appreciable vaterite, LG ACC forms less than 10% vaterite compared to the nearly 80% vaterite formed by ACC 1b.

LG ACC transformation reveals a distinct transformation pathway (defined by both kinetics and polymorph selection) compared to synthetic samples. This mirrors the comparison of the biogenic and synthetic dehydration behaviors where it was concluded that different populations of hydrous components and their unique structural roles determined dehydration behavior. The same reasoning can be applied to transformation behavior, where transformation from hydrated ACC to anhydrous crystalline polymorphs requires significant change to the H_2O structure.

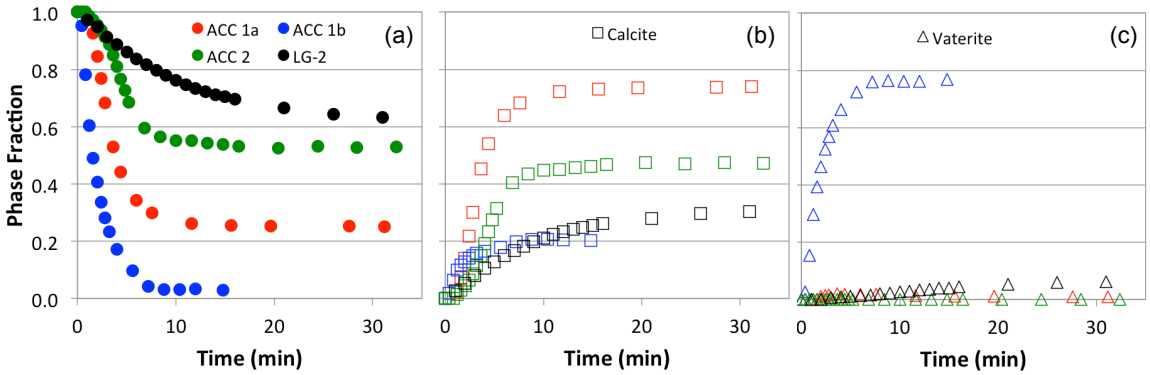

Figure 31. Comparison of time-resolved transformation behavior for biogenic and synthetic ACC samples reacting in DI water on the same time scale showing (a) ACC, (b) calcite, and (c) vaterite. Mineral phases are distinguished by marker style, while experimental series (starting ACC types) are distinguished by color. Synthetic sample data from Chapter 3.

3.2.5 Transformation kinetics and polymorph selection

In situ experiments exhibit a wide range of transformation kinetics. Comparison of H_2O-mediated time series results (Figure **31**a) shows that dehydration may affect both the rate of transformation (ACC loss or inversely, crystalline formation is commonly used as a proxy for the degree of transformation as it is here) and the overall fraction of ACC lost. From the modeling work of Saharay et al., increasing dehydration would cause the bond strength of remaining hydrous components to increase.[81] From this conclusion, we could expect that any partial dehydration would decrease transformation rates and degree of reaction progress. However, more than one factor controls transformation kinetics. Due to the limited number of hydrous component bonding sites available in a given amount of ACC, there may be certain proportions of H_2O components and overall contents that stabilize the amorphous structure more than other arrangements. For instance, in the ACC model by Goodwin et al. some hydrous components are located in Ca-poor channels where bonding is dominated by weaker H-bonds while some hydrous components are coordinated with calcium atoms in the Ca-rich framework.[30] Loss of

hydrogen bonded components might not weaken the structure as much as loss Ca-ccordinated hydrous components. The mobile and rigid H_2O proportions generated by heating to 115 °C may not be as stable as those populations in fresh, hydrated LG and LG dehydrated to 150 °C.

Hydration state may also affects polymorph selection. The three different hydration states all produce slightly different proportions and formation times for the crystalline fractions. The loss of 66% of total H_2O is correlated with near total suppression of the vaterite fraction in the LG-d150 experiment. Whereas loss of only 33% of total H_2O is correlated with nearly equal Cc and Vat fractions in LGd-115. The mechanism controlling polymorph selection is unclear, but these experiments suggest an important role for hydrous components. Further work on the relationships between H_2O content, hydrous component populations, and ACC transformation is needed and is forthcoming from our group.

4. Conclusions

The minute structural changes observable with PDF reveal a mostly intact Ca-rich framework, indicating that the myriad differences observed in heat-induced and H_2O mediated transformations of fresh and partially dehydrated LG are driven at least in part by the changing H_2O structure. In light of these results, hydration state plays a key role influencing both transformation kinetics and polymorph selection. The extended isothermal experiments here and the similar experiments on synthetic ACC samples by Schmidt et al. found evidence for kinetic hindrance of H_2O loss, but the mechanism of this hindrance cannot be determined from the techniques used in either study.[125] We conclude that LG dehydration proceeds via a two step process: (1) simultaneous loss of rigid and restrictedly mobile H_2O at slightly different rates until most or all of the mobile H_2O is depleted and (2) loss of a remaining, kinetically hindered H_2O fraction. The exact role(s) of each hydrous component remains to be seen. This study and other works have begun exploring the complex roles of H_2O in ACC transformation, but many questions remain.

Supporting Information

The F(Q) and G(r) patterns for LCF end-members are identical to those described in Chapter 3 (Figure S **27**).

The DI water contribution to the *I(Q)* for the 115 °C sample experiment shows a slight increase until approximately 17 min, which is comparable to the DI water contribution behavior in the fresh gastrolith experiments (Figure S **28**). The DI water contribution for the 150 °C sample experiment exhibits unusual behavior compared to other experiments. This may have been caused by lack of excess water to soak the sample fully so water moved through the sample without fully saturating. This theory is supported by the comparison of the DI water contribution for this experiment compared to all other *in situ* gastrolith experiments. At approximately 30 min, the contribution of DI water is 18 %, 25 %, and 30 % for this experiment, the 115 °C sample experiment, and the fresh gastrolith experiments, respectively. The contributions of the DI water and amorphous phase are the most difficult to deconvolve so the unusual behavior of the DI water is unlikely to affect the crystalline components, which are more important to the discussion of polymorph selection.

Experimental reproducibility error was calculated for each phase (ACC, Cc, Vat) from 12 identical time points in the LG-1 and LG-2 experiments. The overall root squared error for each time point (error bars in transformation time series figures) contains contributions from the phase fraction reproducibility uncertainties and the fitting RMSE.

Plots comparing the predicted versus measured I(Q) from LCF are shown with differences for the experiments with the greatest and least RMSE (Figure S **29**). The misfit shown by the difference curve in the LG-1 I(Q) comparison is sharp rather than broad, indicating errors due to crystalline components. The most likely cause is differences in grain size as crystal growth progresses (discussed in Chapter 3 Supporting Information).

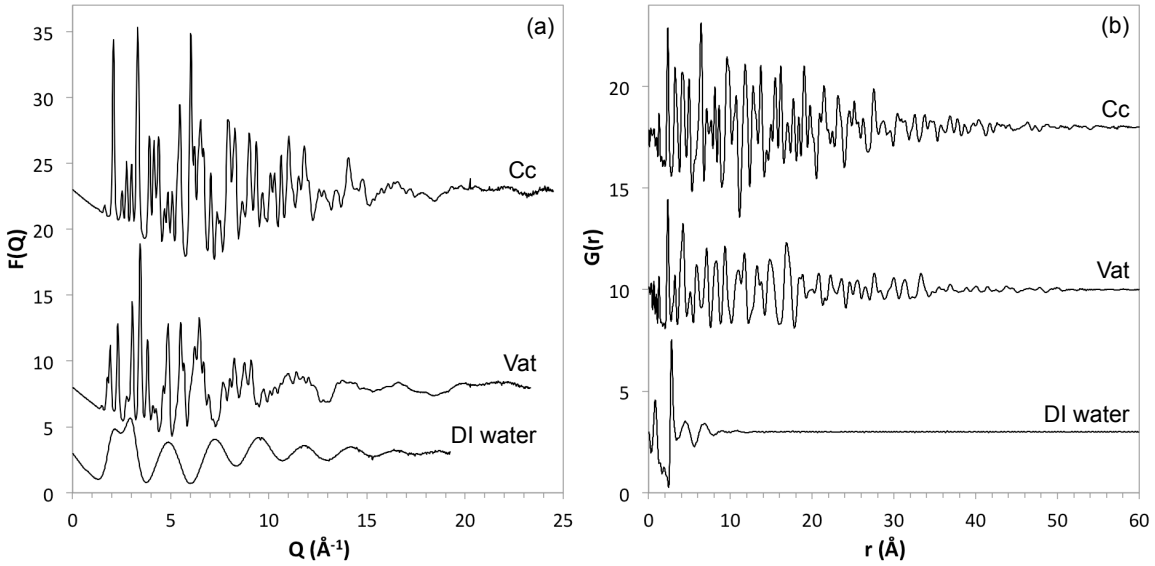

Figure S 27. X-ray total scattering results for crystalline polymorphs and DI water showing (a) the reduced structure function and (b) the pair distribution function.

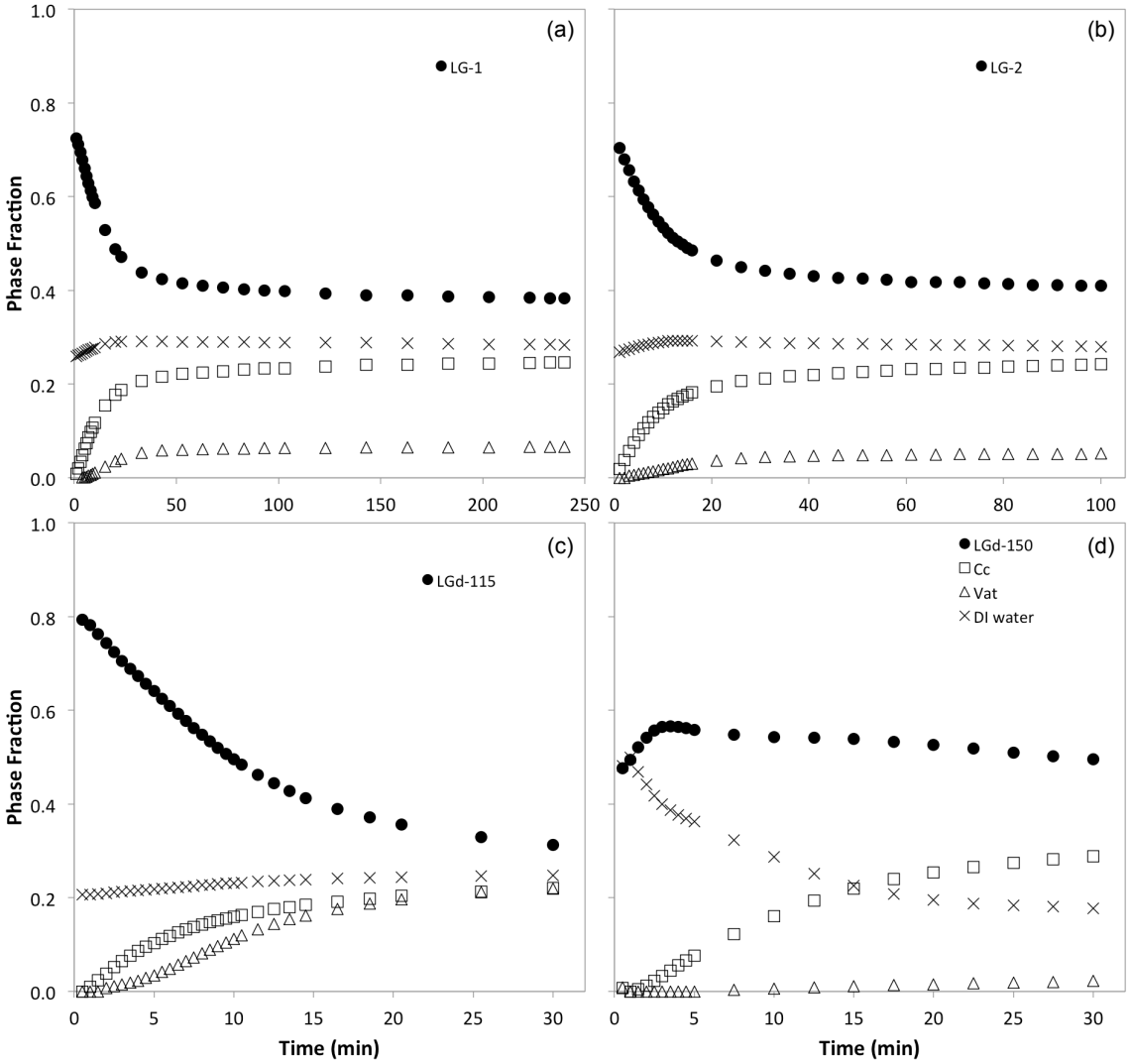

Figure S 28. Time-resolved four end-member transformation behavior for *in situ* total scattering experiments showing phase fractions over time for (a) LG-1, (b), (c) LGd-115, and (d) LGd-150.

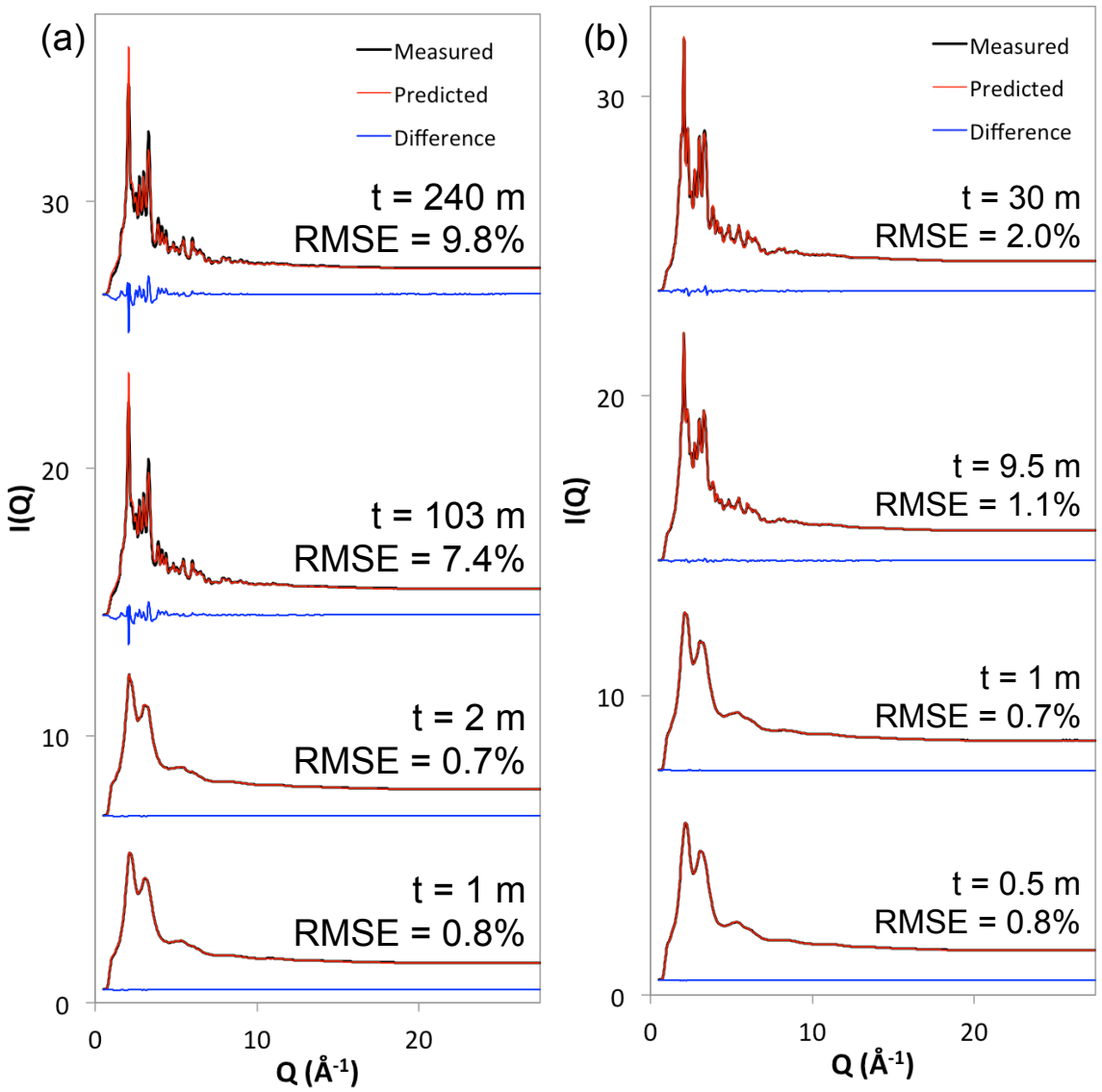

Figure S 29. Goodness of fit analysis for experiment with the (a) largest calculated RMSE, LG-1, and the smallest calculated RMSE, LG-115. Plots show overlays of the predicted and measured *I(Q)* data with difference on the same scale (arbitrary offset along the y-axis between time points).

Chapter 5: Transformation behavior and structure of a series of amorphous calcium carbonate/phosphate hybrids

ABSTRACT: A series of phosphate doped amorphous calcium carbonate (ACC) samples and carbonate doped amorphous calcium phosphate (ACP) samples were synthesized from aqueous solutions at low temperature and pressure (PACC series). Phosphate was observed to partition preferentially into the solid over carbonate. Thermal analysis revealed an increasing thermal stability with increasing phosphate content. Local and intermediate range structure was investigated using Ca K-edge X-ray absorption spectroscopy and X-ray total scattering and pair distribution function (PDF) analysis. Local structure from near-edge spectroscopy showed no indication of deviation from octahedral calcium coordination. PDFs of the PACC series show a progressive change from ACC-like to ACP-like structural features, with intermediate composition samples containing pair correlations at unique distances compared to ACC or ACP. Although the charge imbalance in this phosphate/carbonate substitution prevent a true solid solution from forming, further analyses of the PACC series structures using principal component analysis and linear combination fitting revealed that the structural data can be modeled with two end members with the structural intermediates exhibiting the greatest misfit. The structural effects of phosphate dopants in ACC have not been well studied to date despite it being commonly found in biogenic ACC samples and the theorized stabilizing effects of phosphate. Although carbonate is a known component of crystalline bone minerals, the structural effects of carbonate incorporation on ACP are not well understood. This study provides new insight on the role of anion dopants in these medically and industrially useful materials.

1. Introduction

Amorphous precursors to crystalline materials are found in numerous organisms and under a wide range of environmental conditions in vitro.[1, 18, 55] Amorphous calcium carbonate (ACC) and amorphous calcium phosphate (ACP) are known in biological systems as precursors to stable crystalline phases and have been studied in the laboratory to understand their roles in bio-inspired materials synthesis and engineering. ACC occurs throughout the lower phyla of the animal kingdom with a variety of compositions and functions and is also an important industrial material.[3, 21, 23] ACP has medical applications ranging from surface coatings on joint replacements to dental bio-composites that promote enamel regeneration.[105-110] Despite its common use in bone-related treatments, the occurrence of ACP as a precursor to mineralized vertebrate bone is still debated.[9, 10, 105, 139]

Biogenic and synthetic ACC samples have been shown to incorporate additives that may be grouped into three categories: inorganic ions,[2, 40-43, 76, 84, 112] organic macromolecules,[47-49, 55, 57, 59-63, 77, 91, 102, 140, 141] or metal-organic combinations.[20, 64, 85, 87] Of the inorganic ions, few studies have examined phosphate incorporation in vitro despite its importance in biogenic ACC.[1, 3, 21, 39, 44, 100] Sugiura et al. studied the effects of phosphate doping on ACC transformation and found phosphate to be an accelerator of the ACC transformation to vaterite at low concentrations and an inhibitor at high concentrations.[44] Al-Sawalmih et al. concluded that phosphate, rather than magnesium and organic macromolecules, is the key to biogenic ACC stabilization. To understand the stabilizing effects of phosphate on ACC, a better picture of the structural effects of its incorporation is needed.

The short- and medium-range structure of ACP is most commonly described in terms of the Posner cluster, a spherical, 9.5 Å, anhydrous molecule with the formula $Ca_9(PO_4)_6$ (with the ACP formula generally reported as $Ca_3(PO_4)_2 \bullet nH_2O$).[9, 142] The occurrence of carbonate in bone mineral has been noted but carbonate structural effects on ACP are not well characterized.[9, 105, 143] Carbonate incorporation into ACP has been shown to increase the Ca/P ratio and provide a

stabilizing effect in solution.[143] Posner and Betts found that carbonate caused distinct changes to crystalline hydroxyapatite structure, but there is a paucity of information on the effects of carbonate on amorphous structure.[9]

In this study, we studied the incorporation behavior of phosphate into ACC and carbonate incorporation into ACP, focusing on the short and medium range structural effects. Thermal analysis was used to examine heat-induced transformation behavior and to determine H_2O contents. X-ray absorption spectroscopy and X-ray total scattering were employed to observe changes in the short and intermediate range structure with changes to the phosphate/carbonate ratio. The combined information about amorphous structure, transformation behavior, and composition sheds light on the roles of anion dopants on ACC and ACP structures and stabilities and the effects of competing carbonate/phosphate during synthesis. The microscopic structure of these materials holds the key to manipulation of desirable macroscopic properties for medical and industrial applications and will also contribute to a gap in our understanding of biogenic amorphous precursors.

2. Methods

2.1. Inorganic Phosphate-Doped ACC Samples (PACC)

A series of amorphous calcium phosphate/carbonate samples were synthesized adapting the procedures of Koga et al. (1998). Three 0.02 M solutions were made from reagent grade sodium carbonate, sodium phosphate monobasic, and calcium chloride dihydrate from Fisher Scientific (solutions 1, 2, and 3, respectively). Solutions 1, 2, and 3 were combined in numerical order (Table **10**), precipitates formed immediately, and samples were filtered through a 0.45 μm Nylon membrane filter on a vacuum filtration system. Samples were immediately rinsed with fresh acetone to remove water, vacuum dried, and placed under soft vacuum in a desiccating chamber for 10-20 minutes. Sample labels include the prefix PACC followed by the % phosphate in the synthesis solution with the exception of 0.5% phosphate in solution, which has the designation PACC05.

Table 10. Starting solution compositions for PACC samples in mole percentages. Solution volumes for PACC50 and PACC70 syntheses were increased to increase sample yield.

Label	% phosphate in solution	% carbonate in solution	Mole PO_4^{3-}/mole CO_3^{2-} in solution	Solution 1 (mL) Na_2CO_3	Solution 2 (mL) $NaH_2PO_4 \bullet H_2O$	Solution 3 (mL) $CaCl_2 \bullet 2H_2O$
ACC	0%	100%	--	20.0	0	20.0
PACC05	0.5%	99.5%	0.01	19.9	0.1	20.0
PACC2	2%	98%	0.02	19.6	0.4	20.0
PACC5	5%	95%	0.05	19.0	1.0	20.0
PACC10	10%	90%	0.11	18.0	2.0	20.0
PACC30	30%	70%	0.43	14.0	6.0	20.0
PACC50	50%	50%	1.00	15.0	15.0	30.0
PACC70	70%	30%	2.33	12.0	28.0	40.0

2.2 Reference Samples

Undoped synthetic ACC was synthesized following similar methods to the PACC samples but omitting solution 2 (identical to ACC 1b from Schmidt et al.).[125] Equal volumes of solution 1 and 3 were mixed followed by the identical rinsing, drying, and dessicating procedures applied to PACC samples. Reagent grade calcite was obtained from Spectrum, rinsed, and dried before analysis. Vaterite was synthesized by adapting the method of Gebauer et al.[34, 35] Dopant-

free ACP was synthesized following the method of Eanes.[144] Pure synthetic hydroxyapatite (HAP) and octa-calcium phosphate (OCP) were used for standards.

2.3 Aging experiments

Aging experiments were performed on PACC2 and ACC samples to qualitatively compare transformation products and kinetics. Freshly synthesized samples were analyzed by XRD then placed in controlled humidity chambers at 92% relative humidity and ambient temperature (20–21 °C). Over 0.5 to 11 hr, samples were removed from the environmental chambers at selected intervals, analyzed by XRD, and returned to the chambers. XRD scans were 15 min and samples were exposed to ambient humidity conditions for less than 20 min for each analysis. The aging time was calculated from the time samples were enclosed within an environmental chamber. Although chambers are small (1.75 L), there is a 5–10 min lag between opening a chamber and returning to the maximum relative humidity, 92%.

2.4 Thermal Analysis and Calorimetry

Simultaneous thermo-gravimetric analysis and differential scanning calorimetry (TGA-DSC) measurements were completed on a Netzsch STA 449C Jupiter instrument. Samples were heated over the interval 30–900 °C at 10 °C/min under flowing nitrogen gas in an Al_2O_3 crucible.

2.5 Compositional Analysis

Compositional analyses for phosphate were completed on a SealAA3 multichannel analyzer using the colorimetric molybdenum blue method. Samples were dissolved with HCl and serially diluted with deionized water prior to phosphate analysis. Carbonate mass fractions were calculated from TGA data. Mass losses from 500 to 900 °C were assumed to be due to decarbonation reactions.

2.6 X-ray Scattering

Conventional X-ray diffraction (XRD) was conducted on a Scintag diffractometer with a copper Kα source (λ = 1.54 Å). Scans were collected over the range 10–80 °2θ at a scan rate of 2 °/min.

Total X-ray scattering data were collected at the undulator beamline 11-ID-B at Argonne National Laboratory's Advanced Photon Source (APS). Beam energy (58 keV, λ = 0.2127 Å) was selected with a Si(311) monochromator, and scattered X-rays were detected with a Perkin Elmer amorphous silicon area detector. Sample-detector distance and detector non-orthogonality were calibrated using a NIST CeO_2 standard (diffraction intensity set: 674a). Conversion of collected data from 2D to 1D was performed in the program Fit2D, applying a polarization correction upon integration.[115]

Intensity data were transformed into the experimental total scattering structure function, *S(Q)* and the reduced experimental structure function, *F(Q)*. All ACC *F(Q)* data were truncated at ~20–23 $Å^{-1}$ before Fourier transformation to the pair distribution function, *G(r)*, with the program PDFgetX2, where beamline-specific and standard corrections were applied.[116, 117] Sample compositions used to normalize intensity data were calculated from a combination of TGA-DSC measurements and linear combination fitting results of total scattering *I(Q)* data (full explanation of this procedure is found in Supplemental information and final compositions are given in Table S **5**).

2.7 X-ray Absorption Spectroscopy

X-ray absorption fine structure (XAFS) and X-ray absorption near-edge (XANES) spectra were collected at the bending magnet beamline X-19A at Brookhaven National Laboratory's National Synchrotron Light Source (NSLS). The first peak in the derivative of the edge energy observed for a 6 μm titanium metal foil was set to 4966 eV for monochromator calibration, and the foil was mounted between I_t and I_{ref} for calibration checks throughout beamtime. A double-crystal Si(111) monochromator was used to vary the incident energy around the calcium K-edge at 4038 eV, with 50% detuning for harmonic rejection. All data were collected in transmission mode using gas-filled ion chambers. Samples were analyzed <3 hours from the time of synthesis.

3. Results and Discussion

3.1 Phosphate/carbonate incorporation

Partitioning of phosphate and carbonate between solution and solid precipitate (PACC) is shown in Figure 1. We see that the molar PO_4^{3-}/CO_3^{2-} ratio in the solid increases with increasing molar PO_4^{3-}/CO_3^{2-} ratio in the synthesis solution, although the relationship is not linear. Low phosphate in solution samples (PACC05 to PACC2) produced ratios that were identical within one standard deviation. The PACC10 and 30 replicates were in good agreement, but there was a large spread in the PACC50 sample replicates. The source of this reproducibility issue is unknown at this time. Comparison to the 1:1 line (dashed line in Figure **32**) shows that phosphate is preferentially incorporated into the solid over carbonate. A linear regression does not represent the whole range of data well. The data were fit with a $y = 8.3\ x^{1.6}$ curve, producing an $R^2 > 0.9$. The low phosphate containing samples (PACC05 through PACC10) are well-represented by the 1:1 relationship however (Figure **32** inset). This analysis assumes complete electrolyte dissociation in solution. In reality, there is a mixture of PO_4^{3-}, HPO_4^{2-}, and $H_2PO_4^-$ phosphate species in solution with a nearly 50/50 ratio of HPO_4^{2-} and $H_2PO_4^-$ at neutral pH. There is also a mix of carbonate/bicarbonate species, but protonation differences for both anions would affect only the hydrous component incorporation and not the phosphate/carbonate molar ratio.

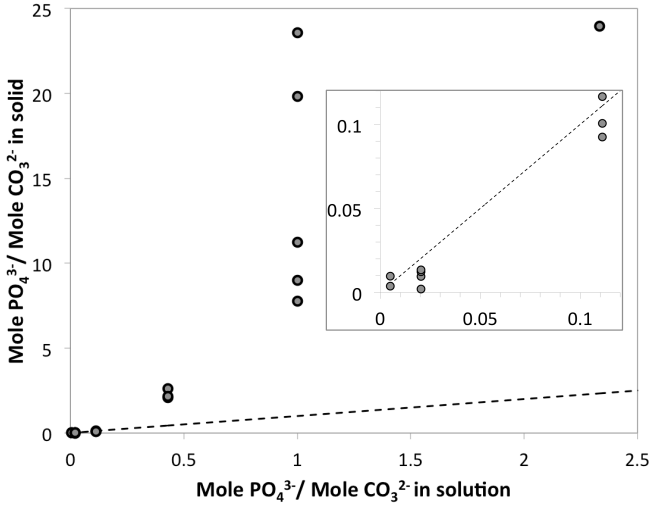

Figure 32. Molar phosphate/carbonate ratios in the solid and synthesis solution for samples in the PACC series with an inset showing low-phosphate PACC samples. The dashed line represents the 1:1 proportion.

Phosphate/carbonate molar ratios in the solid do not provide insight into the method of incorporation or the identity of the solid phase(s) present. We propose 3 possibilities for the identity of the PACC series samples: (1) phosphate-doped ACC in an effective solid solution with carbonate-doped ACP, (2) a mixture of ACC and ACP phases, or (3) a combination of both. We will explore these possibilities through thermal and structural analysis.

3.2 Dehydration behavior and heat-induced transformation

Thermal analysis provides simultaneous information about H_2O content and heat-induced transformation behavior for PACC samples across the composition range of the series. Figure **33** shows an overlay of representative data for the entire PACC series. Figure S **30** in the supplemental information shows data with replicates. There are three first-order features that vary across the PACC series in both TGA and DSC plots: the first large mass loss and associated broad endotherm over the temperature range 30–300 °C, the crystallization exotherms occurring over a wide range of temperatures, and the large mass loss and associated endotherm from 600–900 °C. All samples (PACC series and ACC and ACP reference samples) show the large initial mass loss and endotherm commonly attributed to H_2O loss, though the character of the features varies. ACC H_2O loss is characterized by an obvious multi-step mass loss and large area endotherm. The mass loss slope, temperature range over which the mass loss occurs, and area of the associated DSC endotherm vary over the PACC series. The area of the dehydration endotherm peak decreases with increasing phosphate/carbonate molar ratio in the solid. PACC05 through PACC10 show an overall H_2O loss behavior (similar slope, temperature range, and endotherm area) most similar to ACC. PACC30 through PACC 70 exhibit an extended temperature range over which H_2O loss occurs, and smaller area endotherms. PACC70 shows the complicated loss behavior most clearly with an initial steep mass loss slope from 30–160 °C then a shallower mass loss slope from 160–420 °C. Similar complex H_2O loss behavior was described by Schmidt et al. and attributed to different hydrous populations dominating mass loss.[125]

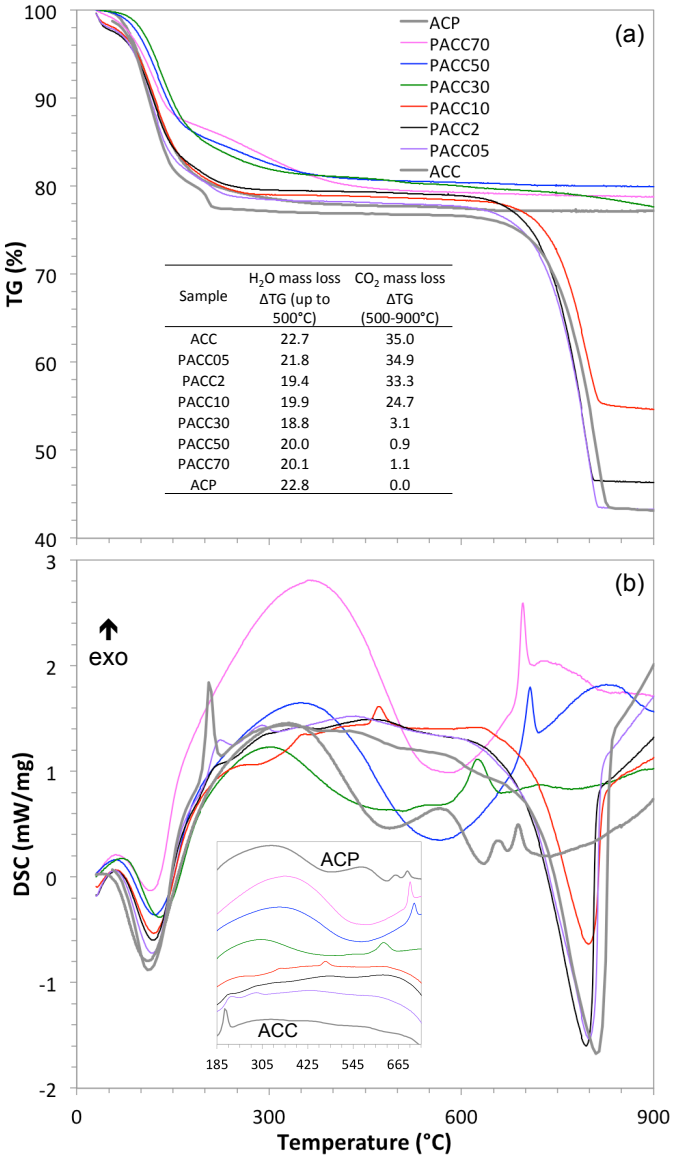

Sample	H_2O mass loss ΔTG (up to 500°C)	CO_2 mass loss ΔTG (500-900°C)
ACC	22.7	35.0
PACC05	21.8	34.9
PACC2	19.4	33.3
PACC10	19.9	24.7
PACC30	18.8	3.1
PACC50	20.0	0.9
PACC70	20.1	1.1
ACP	22.8	0.0

Figure 33. Thermal analysis of PACC series showing (a) TG and (b) DSC. Inset table lists mass losses at four temperatures of interest, and inset figure in panel (b) shows the DSC curves over the temperature range of crystallization with arbitrary offsets along the y-axis. Uncertainty for ACC sample represents the standard deviation from 6 replicates. Reproducibility uncertainties for PACC series mass loss are ± 1.2 %, an average of the standard deviations of the 4 samples with replicates at the 4 reported temperatures. Relative mass loss resolution within a single analysis is 25 ng; heat flow measurement sensitivity is 0.73 μV/mW).

The second first-order feature, the crystallization exotherm, reveals a wide variation in temperature range and character of exothermic peaks for PACC samples (Figure **34**b and inset). PACC05 shows a small exothermic doublet (Figure **34** inset). Exothermic features for PACC2 are nearly suppressed despite being amorphous. PACC10 has two small exothermic features separated by ~100 °C. All other PACC samples (PACC30, 50, and 70) have a single crystallization exotherm. ACC has a single, highly exothermic crystallization peak at ~200 °C, and ACP has a crystallization doublet at ~665 °C. The plot of PACC series crystallization

temperatures versus phosphate/carbonate molar ratios in the solid exhibits a non-linear relationship (Figure **34**a), which is expected due to the partitioning behavior described in Section 3.1. The plot of crystallization temperature versus the fraction of evolved CO_2 reveals a direct positive relationship (Figure **34**b). This indicates that crystallization temperature for the PACC series samples is directly related to carbonate content.

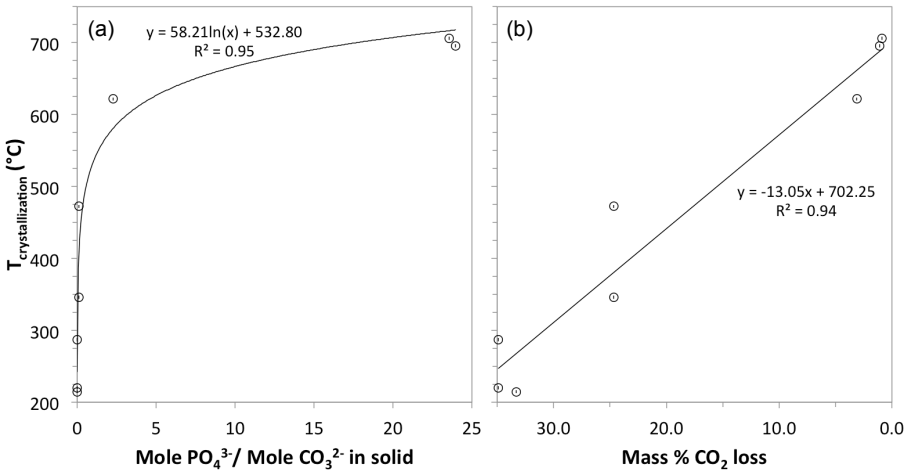

Figure 34. Plot of crystallization temperatures versus (a) starting phosphate fraction in solution and (b) mass % CO_2 evolved from the sample on heating. Temperature uncertainty shown is ±2.3 °C based on replicates. Inset table shows average peak position and integrated peak areas (exothermic reactions are positive). Peak area uncertainty is ±9.5 J/g based on replicates.

The last first-order feature for comparison is the high-temperature mass loss and associated endotherm due to decarbonation (Figure **33**). ACC exhibits the greatest mass loss and the largest area endotherm from decarbonation. For the PACC series samples, % mass loss from decarbonation decreases with increasing phosphate content (Figure **33**a inset). For PACC50 and 70, there is no visually obvious mass loss or endotherm, however, there is measureable mass loss. The decarbonation loss for PACC50 and 70 are similar, which could indicate that above a certain phosphate/carbonate mole ratio in solution, the precipitated species has a set phosphate/carbonate mole ratio that can be incorporated into the solid. The PACC70 phosphate content was similar to the higher end PACC50 values (Figure **32**). Further constraint of the PACC50 phosphate/carbonate mole ratio in the solid would confirm this interpretation. ACP shows no measurable mass loss at high temperature.

PACC series thermal behaviors show a progression of increasing crystallization temperatures with increasing phosphate content, which is evidence for phosphate incorporation in ACC and carbonate incorporation in ACP rather than a series of mineral mixtures. Because TGA-DSC is a bulk analysis technique, the behavior of a mixture should appear as a mass weighted combination of the two components. For extreme mixtures (*e.g.* low ACC and high ACP), the effects of the smaller component on the average thermal behavior might be lost, but for intermediate mixtures, *e.g.* PACC10 and 30, there would be some evidence of mixed behavior. For example, a sample containing a 50/50 ACC/ACP mixture by weight would show a crystallization exotherm of the ACC at ~200 °C and the ACP at ~700 °C. Though PACC10 does exhibit two possible crystallization features, neither occur at the ACC or ACP crystallization temperatures. No samples show evidence of this kind of mixed behavior indicating that the PACC samples are different from their pure ACC and ACP counterparts. If fractions of pure

ACC and/or pure ACP are co-precipitating in the PACC syntheses, they are in small enough amounts that they do not affect the TGA-DSC measurements. We conclude that the progressive change in crystallization is the result of carbonate or phosphate being structurally incorporated into ACP and ACC structures.

Evidence for variation in the hydrous components is found in the comparison of the ACP and high-P PACC sample TG curves. While ACP shows a steep H_2O loss slope followed by a short continuous transition to a near-zero mass loss regime, PACC50 and 70, which otherwise have thermal behaviors close to ACP, exhibit an additional mass loss regime from ~140–350 °C. This additional mass loss regime has a slope intermediate between the initial steep H_2O loss and the near-zero, higher temperature mass loss and indicates a more complex H_2O picture than pure ACP. Posner and Betts proposed that the 15–20 wt% H_2O in ACP is not structural, only interstitial between $Ca_9(PO_4)_6$ clusters.[9] A sample with only adsorbed H_2O would exhibit the kind of TG curve described above for ACP. Multi-step mass loss in lower temperature regimes has been previously attributed to the complex loss of different H_2O components in ACC.[125] Schmidt et al. concluded that low temperature multi-step mass loss was caused by different populations and different structural roles of the four hydrous components in synthetic ACC.[125] They also found evidence for kinetic hindrance of H_2O loss on heating, which could contribute to the large temperature range of the intermediate mass loss regimes in PACC50 and 70.[125]

The multiple phosphate and carbonate species present during synthesis could also promote variation in hydrous component incorporation. In a density functional theory-based modeling study of carbonate substitution into hydroxyapatite, Astala and Stott concluded that the substitution of a carbonate for a phosphate was energetically more favorable than carbonate substitutions elsewhere and correlated to additional inclusions of H atoms.[145] Alterations to the H_2O structure may be part of the charge balance from carbonate substitutions. In their hydrothermal syntheses of a series of different phosphate carbonate ratio materials, Eliassi et al. determined that some of the amorphous phases included hydrous components, particularly in the form of OH.[146] Schmidt et al. found evidence that OH components were not readily lost at temperatures up to 200 °C from NMR and TGA-DSC data.[125] Incorporation of OH components into high phosphate PACC samples could explain the multi-step mass loss up to 350 °C. TGA-DSC analyses indicate that even a small amount of carbonate incorporation has the potential to affect ACP thermal behavior, which may be attributable, in part, to the simultaneous incorporation of structural hydrous components.

3.3 PACC series structure

3.3.1 Short-range structure and the calcium environment

Plots of normalized absorption coefficients of Ca K-edge XAFS data show the pre-edge feature and singlet peak after the white line characteristic of Ca K-edge data as expected (Figure **35**). The $k^3\chi(k)$ curves show a diminishing single beat pattern. There is a slight change in the shoulder feature at 3.4 $Å^{-1}$, which is sharp for PACC2 and PACC10 samples but less well-defined for samples with higher phosphate contents. The most distinct change with increasing phosphate content is evident in an overlay of the $k^3\chi(k)$ data (see Supplemental Information Figure S **31**), a loss of peak amplitude at higher k peaks is correlated with an increase in phosphate content.

A large glitch is pervasive at ~9 $Å^{-1}$ in all data taken at this beamline. The glitch occurs over multiple points. Tow to three points were removed from the glitch in each file in each data set before averaging. This deglitching still left some samples with remnants of the glitch, which

appears to have different character in different samples. The PACC2 curve appears to have a small offset at the glitch. However, the same glitch leaves what appears to be a dip in a broad peak after deglitching, particularly obvious in the PACC30 and PACC50 curves.

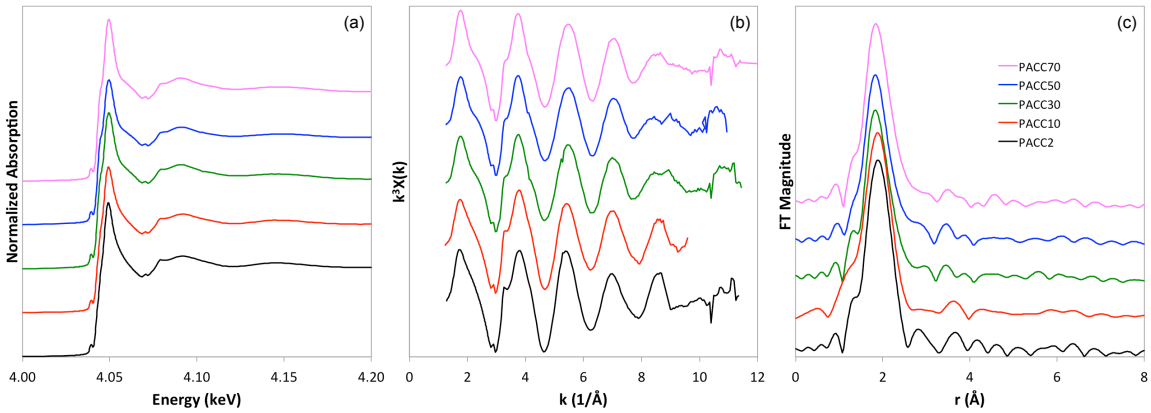

Figure 35. XAFS results for PACC series samples showing (a) normalized absorption, (b) χ(k) with a k-weighting of 3, and (c) χ(r).

Fourier transform magnitudes of the $k^3\chi(k)$ curves exhibit a shift in the first shell peak maxima to shorter r with increasing phosphate/carbonate molar ratio in the solid (1.89 to 1.82 Å). Changes beyond the first shell are subtle. PACC30, 50, and 70 have a distinct high-r shoulder feature with a possible second shell at 3.4 Å, though the data is not corrected for phase shifts. PACC70 shows a possible third shell at 4.5 Å, but these features are small relative to rippling. The broader first peak in the FT magnitude for PACC10 is due to the shorter *k*-range used. PACC2 FT magnitude shows no discernable features beyond the first shell. As we concluded in sections 3.1 and 3.2, the PACC samples appear to have unique intermediate structure compared to ACC and ACP though comparison to references would corporate this conclusion.

Normalized XANES data contains three primary features: the pre-edge peak (feature 1 in Figure **36**), the shoulder on the white line (feature 2), and the white line maximum (feature 3). The differences in the absorption curves are difficult to distinguish, but the first and second derivatives show clear variations (Figure **36**b and Figure **36**c). In the first derivative, the samples can be grouped by appearance, PACC2 and 10 curves are similar and PACC30-70 curves are similar. The primary difference is found in the energy region between features 1 and 2 with the slope peaking in that region for PACC30-70 and the slope showing more variation for PACC2 and 10.

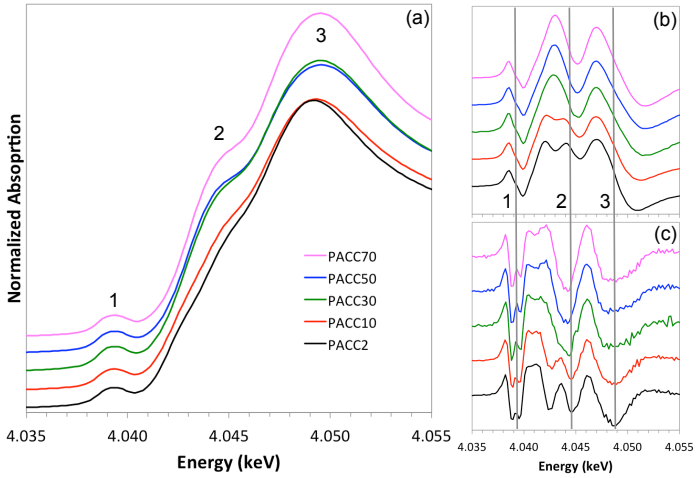

Figure 36. Near edge region comparison of (a) normalized absorption with arbitrary 0.1 vertical offsets along the y-axis and the (b) first and (c) second derivatives over the same energy range.

Du et al. conducted a Ca K-edge XANES study of ACP formation.[142] They analyzed features in the near edge region using second derivatives to qualify changes to molecular orbitals.[142] Du et al. observed the development of short-range structure for ACP samples forming in suspension. Features 1 and 2 correspond to the 1s to 3d and 4p electron transitions, respectively.[29, 147] PACC data shows no changes to the 1s to 3d transition. Changes in feature 1 would be expected if we were observing the formation of the Ca^{2+} solid coordination, transitioning from the H_2O surrounded metal to the solid coordination and guided by dipole selection rules. The 1s to 3d transition is forbidden for perfect octahedral symmetry.[29, 142, 147] The development of feature 2, particularly evident in the second derivative, was attributed to a shift toward octahedral symmetry due in part to bidentate coordination possible for the phosphate according to Du et al.[142] There are intensity differences for the first shell peak, feature 3, but no clear trends with phosphate content.

3.3.2 Short and intermediate range structure

I(Q) data obtained from X-ray total scattering from PACC samples show a broad primary doublet at low Q, with broader oscillations that dampen by 10 $Å^{-1}$ (Figure **37**). As phosphate content increases, the peak at 2.1 $Å^{-1}$ shifts to lower *Q* and increases in intensity while the second peak in the doublet (at ~3.1 $Å^{-1}$) systematically shifts to higher *Q* and decreases in intensity (see Supporting Information Figure S **32** for an overlay of select patterns from the PACC series). The broad feature centered at ~5.2 $Å^{-1}$, the last clearly distinguishable feature, exhibits subtle shape changes as well.

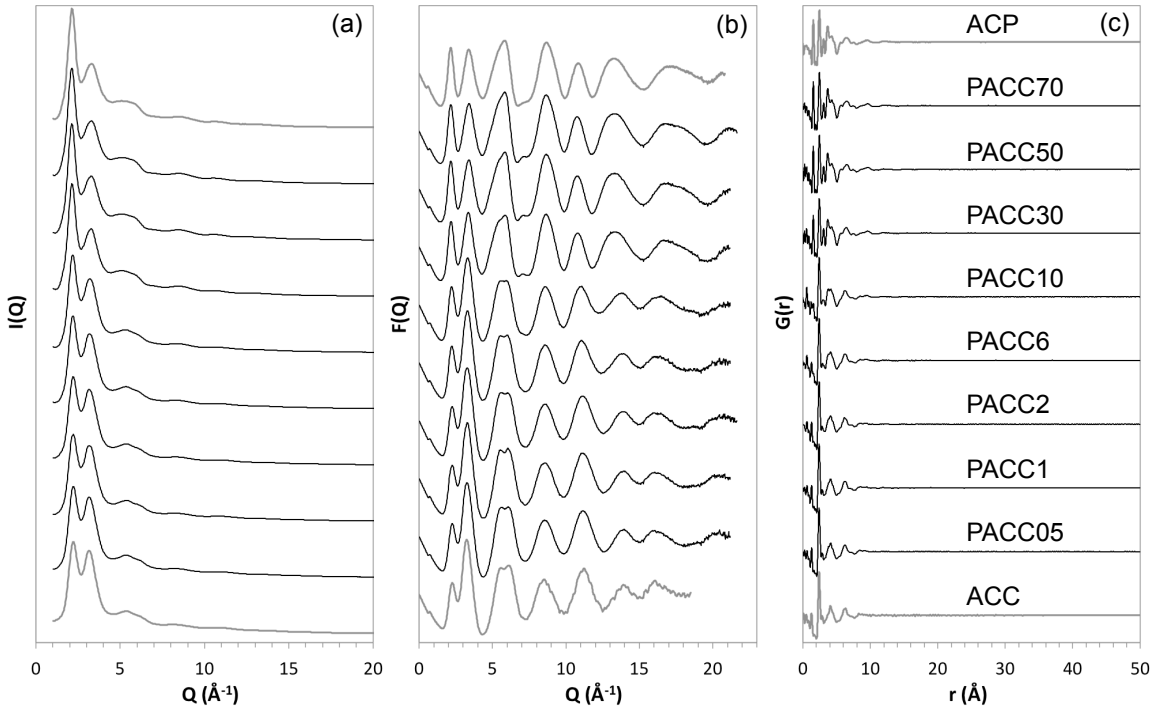

Figure 37. Total scattering results for ACC, PACC series, and ACP showing (a) normalized I(Q), (b) F(Q), and (c) G(r), all with arbitrary offsets along the y-axis.

F(Q) patterns are characterized by a multiple beat pattern with attenuating intensity with increasing *Q*. Changes with increasing phosphate content are clear, with a change in the frequency of oscillations from the mid to high *Q* range and changes to peak shape (Supplemental Information Figure S **32**). PDF patterns for all samples have atom pair correlations over short and intermediate distances up to ~15 Å, with no correlations at higher r, which is characteristic of amorphous materials. Pair correlations for ACC and low phosphate samples diminish at slightly shorter distances (~14 Å) compared to ACP and high phosphate content samples (~16 Å).

The PACC samples can be categorized into groups: those with ACC-like features (PACC05–2), those with structural features from both ACC and ACP (PACC6 and 10), and those with ACP-like features (PACC30–70). For certain features, the intermediate samples can sometimes be grouped with end-members. Differences in pair correlations with increasing phosphate content of the solid are more obvious in a short *r* comparison (Figure **38**). The 1A peak (carbonate C-O first neighbors) at 1.27 Å in ACC is present in PACC05 through 10 samples, though the intensity is noticeably lower, and the distance is slightly smaller (1.25 Å) in PACC6 and 10. For the *G(r)* of PACC30 and above, the carbonate correlation distance is no longer evident. ACP and PACC70 through 30 show a distinct 1.53 Å correlation (phosphate P-O, 1B) with no peak or shoulder at the 1A position. The intensity of the 1B peak in PACC30 is lower than the other high-P samples and the intensity is significantly lower for PACC6 and 10, which contain both 1A and 1B peaks. PACC05 through 2 contain smaller peaks shifted to slightly higher *r*, which may not be evidence of the P-O correlation. Peak 2, the average Ca-O first shell (with contributions from water oxygen and carbonate oxygen suggested from ACC modeling),[29, 81] shows a progressive, slight shift to higher pair correlation distances with increasing phosphate content. ACC, PACC05, and PACC1 have peak 2 maxima at 2.39 Å. For

PACC2 and 6, peak 2 shifts to 2.40 Å, and for PACC10 peak 2 shifts to 2.41. While these distances are within error of identical for this technique, the overall trend indicates these differences may be real, with PACC30-70 and ACP exhibiting the highest pair correlation distance at 2.44 Å. Posner and Betts report that peak 2 also contains contributions from O-O in hydroxyapatite samples.[9]

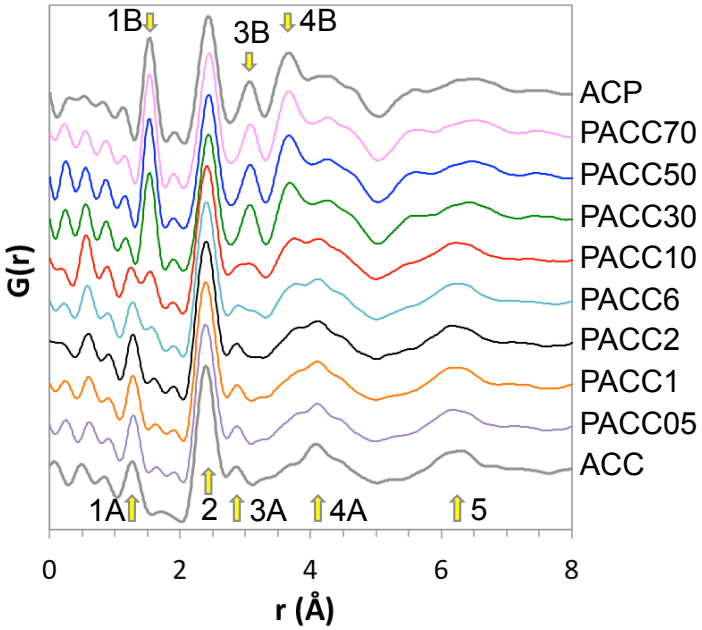

Figure 38. Short r-range comparison of PACC series G(r) with arbitrary offsets along the y-axis.

The 3A/B peak also shows a progressive shift to higher distances with phosphate, and two primary characteristics. The ACC-like group peaks at 2.86–2.87 Å while the ACP-like group (PACC10 through PACC70) peaks at ~3.07 Å. PACC6 peak 3A reaches a maximum nearer the ACC group at 2.90, but PACC6 and 10 are clear intermediates when comparing peak shapes. The 3A peak at ~2.8 Å contains contributions from C-O_{water} and Ca-C.[81] Peak 4A and 4B are dominant in the ACC-like (PACC05–6) and ACP-like (PACC10–70) groups, respectively, with PACC6 and 10 again showing distinct characteristics of both. As *r* increases, the peaks become broader and less distinguishable, making clear groupings more difficult. Peak 5 is the last easily compared peak, with the ACP-like group primarily distinguished by the large low-*r* shoulder feature in PACC30–70. For ACP, correlations in the 3–6 Å region are dominated by phosphate interatomic distances.[9] For ACC, the broad peaks centered around 4 and 6 Å are dominated by Ca-X pairs (X = Ca, O, and C).[29]

In section 3.2, we proposed, based on thermal transformation behavior, that the PACC series cannot solely be comprised of a mixture of ACC and ACP. Examining the structure in detail, there is further evidence for this, particularly in the intermediate samples PACC6 and 10 and the progressive slight shifts in peak positions correlated to phosphate content, *i.e.* peak 2. Studying a series of Mg-doped ACC samples, Radha et al. also concluded that the series of samples were not mixtures of calcium and magnesium carbonates but intermediate amorphous materials.[41] While the effects of the cation are different due to the similar ion size and charge balance, both studies exhibit a structural flexibility for accommodating compositional variation over a limited range.

There is also evidence, however, for structural similarities to end-members, which is complicated by the very subtle shifts in peaks and the nature of the bulk techniques. Despite the progressive changes to thermal behavior and PDF peak positions, there appears to be a phosphate content threshold, above which, samples (PACC30–70) show remarkable structural similarities to ACP. This is expected from the compositional results where the PACC30 through 70 samples all had high phosphate/carbonate molar ratios relative to PACC05 through 10 (Figure **32**). The structural similarities between ACP and high phosphate PACC samples indicate that small amounts of carbonate can be accommodated without significant changes to average structure. The distinct difference in the PACC30 thermal behavior compared to the PACC50 and 70 samples suggests carbonate incorporation may affect H_2O structure, which is not observable in X-ray total scattering because of hydrogen's weak X-ray scattering cross-section, but has the potential to affect behavior on heating.

3.4 Principal Component analysis

To further analyze the structural similarities of the ACC-like and ACP-like groups, principal component analysis (PCA) and linear combination fitting (LCF) were performed on the minimally processed *I(Q)* data (Figure **37**a). PCA is a technique well suited to identifying similarities and differences in large data sets and redefines the data in terms of mathematical "components" that account for variation in the data.

Loading plots visualize the data in terms of two components, with the fraction of variance covered by component 1 shown on the x-axis and the fraction of variance covered by component 2 shown on the y-axis. This plot helps identify subsets of data that vary in similar ways. For the PACC series samples, the *I(Q)* data are all relatively similar: they are all amorphous, contain calcium, oxygen, and H_2O, and have varying amounts of carbonate and phosphate. As a result, over 98% of the sample variance is accounted for by component 1, and the samples all plot in a narrow range for component 2 (Figure **39**a). The clustering of the entire series indicates that all data are positively correlated. On the positive side of the x-axis the ACP-like samples cluster, PACC30–70 with PACC30 showing the most difference from the others. On the negative side, the ACC-like samples cluster, PACC05–10, with PACC6 and 10 showing more variation in component 2 than PACC05–2.

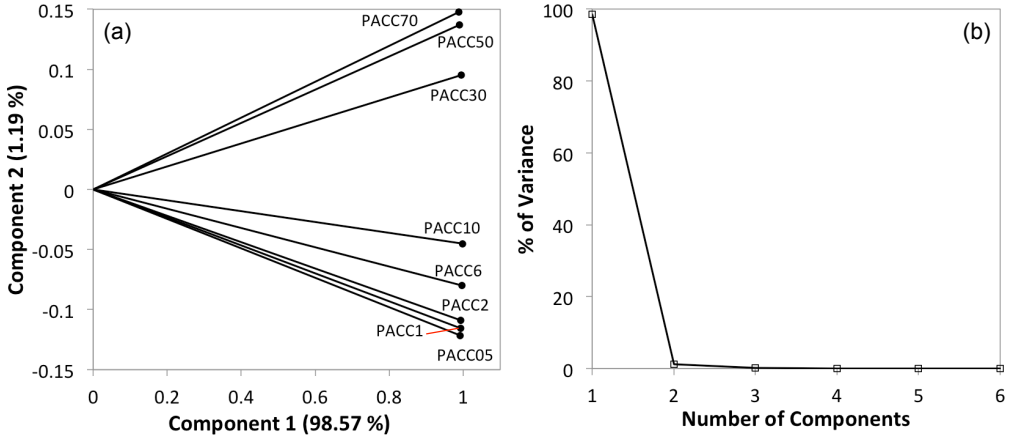

Figure 39. Principal component analysis of PACC series showing (a) the loading plot for the first two principal components and (b) the scree plot for the cumulative variance accounted for by each principal component.

Plotting the cumulative percentage of the variance accounted for by each successive component identifies the minimum number of components necessary to represent the entire data set, defined as the point where the slope of the line changes abruptly to near-zero, at two components in this case. While PCA is useful for reducing a large or complicated data set to minimal components, it does not provide the identity of those components. Possible end-member components can be tested from a fairly small pool of structurally and compositionally similar mineral phases: ACC and ACP being the obvious choices, HAP, OCP, brushite, biogenic ACC, and tri-calcium phosphate to name a few others. LCF results for each sample in the PACC series were plotted versus the % phosphate in the starting solution to compare end-members and misfit (Figure **40** and supplemental information Figure S **33**).

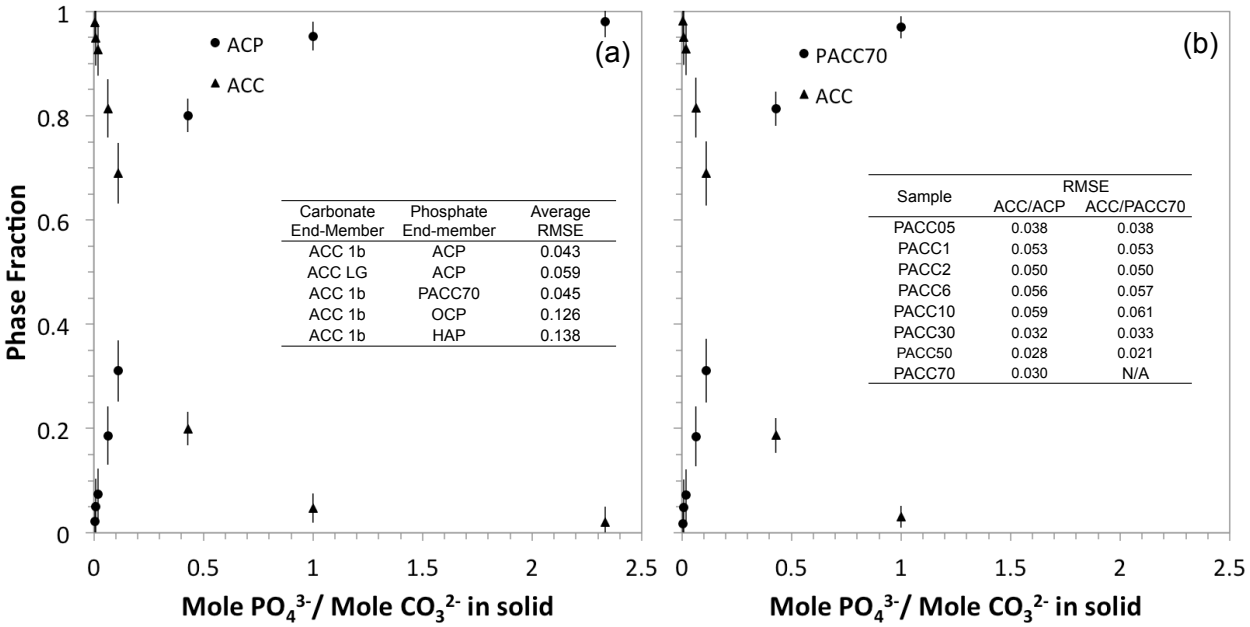

Carbonate End-Member	Phosphate End-member	Average RMSE
ACC 1b	ACP	0.043
ACC LG	ACP	0.059
ACC 1b	PACC70	0.045
ACC 1b	OCP	0.126
ACC 1b	HAP	0.138

Sample	RMSE ACC/ACP	RMSE ACC/PACC70
PACC05	0.038	0.038
PACC1	0.053	0.053
PACC2	0.050	0.050
PACC6	0.056	0.057
PACC10	0.059	0.061
PACC30	0.032	0.033
PACC50	0.028	0.021
PACC70	0.030	N/A

Figure 40. Plot of LCF phase fraction predictions for each sample in the PACC series showing (a) ACC and ACP as end-members and (b) ACC and PACC70 as end-members. Inset table (a) shows the average root mean squared error of the PACC series phase fractions from linear combination fits with different carbonate and phosphate end-members, and inset table (b) compares the RMSE for each of the plotted LCF results.

As phosphate content of the solid increases, LCF results using two end-member fits show a progressive increase of the ACP phase with a corresponding decrease in the ACC phase (Figure **40**a). Error is the greatest for mid-P samples with the smallest error bars seen for PACC05 and PACC30–70. Conducting LCF with biogenic ACC (from lobster gastrolith, LG) produced slightly greater misfit, as defined by comparing average RMSE (Figure **40**a inset). Since the PACC synthesis method is a variation of the ACC synthesis method, it was expected that the ACC would be the best pure ACC end-member. Multiple alternatives to pure ACP were tested including crystalline calcium phosphates, which produced the greatest misfit. After ACP, the least error was produced using PACC70 as an LCF end-member (Figure **40**b). ACC and PACC70 LCF phase fractions generated were all within error of identical to the phase fractions produced using ACC and ACP as LCF end-members. Comparing RMSE point by point, the PACC70 end-member shows the same degree of misfit for low-P samples (PACC05–2), slightly greater misfit for mid-P samples (PACC6–30), and a lower degree of misfit for PACC50. This

indicates that a carbonated amorphous calcium phosphate is a slightly better approximation for high-P samples. Like the ACC/ACP LCF, ACC/PACC70 LCF shows the greatest error for mid-P samples and the lowest error for the phosphate content extremes. Overall, the low residuals of the fits indicate that high- and low-P PACC samples are well modeled by a two end-member system, but intermediate composition samples are not as well represented.

3.5 Transformation behavior of PACC under high humidity conditions

While thermal analysis provides useful information about heat-induced transformation behavior of PACC samples, transformations to crystalline products under ambient conditions are more relevant to environmental conditions. Figure **41** shows successive XRD patterns of ACC and PACC2 aged under high humidity conditions at ambient temperature for different durations. After 30 min in 92 % relative humidity, ACC shows near complete transformation to a mixture of vaterite and calcite. The diffuse features of the ACC are not evident. After 1 hr of aging, the ACC pattern exhibits no visual differences from the 30 min pattern. The XRD pattern for PACC2 remains amorphous at 30 min. After 2.5 hr aging, the pattern shows clear emergence of sharp Bragg peaks, but still retains a significant component of amorphous material as evident from diffuse features. After 11 hr aging, the PACC2 pattern is dominated by Bragg scattering and shows less evidence of diffuse scattering.

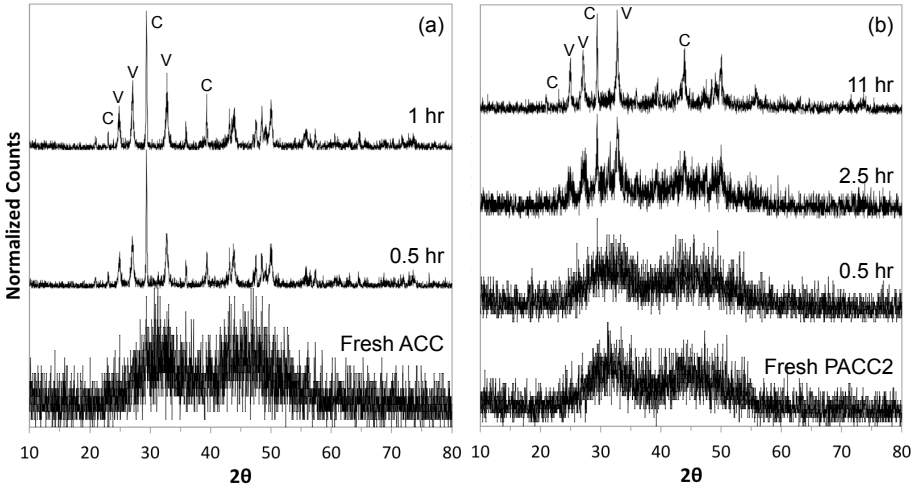

Figure 41. Internally normalized XRD patterns of (a) ACC and (b) PACC2 aged for an increasing duration in high relative humidity conditions. Prominent peaks denoted C or V refer to calcite and vaterite, respectively.

This simple experiment shows that phosphate has a significant effect on transformation behavior under conditions of high humidity. Though both samples transform to a mixture of calcite and vaterite, the peak ratios indicate different relative proportions. Sugiura et al. examined the effects of a range of low-phosphate concentrations on ACC formation and transformation in the synthesis solution and found that phosphate concentration had a significant effect on polymorph selection.[44] They also found an overall positive correlation between increasing phosphate content and the time to onset of crystallization.[44] Though these experiments cannot be compared quantitatively due to the methodological differences, the effects of phosphate are similar in both polymorph selection and transformation kinetics. Stabilization of ACC by phosphate holds implications for research on calcium bioavailability and nutritional

supplements. Meiron et al. determined that ACC is a more bioavailable source of Ca^{2+} than crystalline calcium carbonate, but ACC instability creates impediments for use as a nutritional supplement.[104] Temporary stabilization of the ACC structure by small amounts of inorganic phosphate is a possibility for a more bioavailable dietary calcium.

In situ, time-resolved transformation of ACP samples has not been well explored, primarily focusing on the effects of aging mediums on transformation.[148-150] Abbona and Baronnet studied the effect of magnesium on ACP formation and transformation, finding effects on transformation kinetics as well as morphology, crystal size, and crystal defects.[148] To bridge the gap and expand on the initial, intriguing results of the experiment presented here, an in-depth study of the water-mediated transformation of the entire PACC series samples is forthcoming from our group.

4. Conclusions

Thermal analysis results of the PACC series showed evidence for solid solution-like behavior and also indicated a more complex H_2O structure than concluded in previous ACP studies. In particular, the complex mass loss behavior of the high-P samples revealed that hydrous components are likely being incorporated along with carbonate. These findings warrant further exploration of the H_2O structure of carbonated ACP. Structural analysis suggests that PACC series samples appear to be intermediates between ACC and ACP rather than as mixtures of end-members, though the structural changes are small throughout the compositional series. Ambient temperature transformations of phosphate-doped samples exhibited a significant delay in crystallization compared to un-doped ACC. These results can be bolstered by NMR data looking at the phosphorus associations in the PACC series.

These results open up new areas for exploration. A quantitative analysis of solubility for the PACC series samples would have applications to phosphate cycling in carbonate dominated groundwater systems.[151-153] Identification of the hydrous components of the PACC series via NMR would shed light on the heat-induced and ambient-temperature transformation behavior and provide a contrast to the hydrous component analysis reported for ACC.[125] Further transformation experiments, particularly on the high phosphate samples, could contribute the discussion of ACP as a precursor to carbonated HAP bone mineral. These findings help fill the gap in the ACC literature on the effects of carbonate incorporation and, more broadly, reveal a greater variety of possible amorphous precursors.

Supporting Information

S1. Composition Calculations

The X-ray total scattering data processing of PACC series samples requires compositional information. Chemical formulas were calculated assuming a mixture of two end-members: ACC and ACP. TGA-DSC data were used to calculate H_2O contents. ACC composition was assumed to be $CaCO_3 \cdot nH_2O$, and ACP composition was assumed to be $Ca_3(PO_4)_2 \cdot nH_2O$. The formula units on the left side of Table S **5** were calculated using the parameter estimates for each phase as follows (where *x* and *y* represent the parameter estimates for ACP and ACC, respectively).

$$a \cdot Ca + b \cdot C + c \cdot P + d \cdot O + e \cdot H = x[Ca_3(PO_4)_2 \cdot nH_2O] + y[CaCO_3 \cdot nH_2O]$$

$$\begin{bmatrix} a \\ b \\ c \\ d \\ e \end{bmatrix} = \begin{bmatrix} 3x + y \\ y \\ 2x \\ 8x + x \cdot n_{ACP} + 3y + y \cdot n_{ACC} \\ 2x \cdot n_{ACP} + 2y \cdot n_{ACC} \end{bmatrix}$$

S2. Thermal Analysis

Thermal analysis of PACC sample series with replicates is shown compared to standards ACC and ACP (Figure S **30**). The progression of some features in the TG data is more obvious with offsets rather than overlay. TG data PACC2 and PACC10 replicates show the greatest deviation. DSC data replicates show some variation in peak area, but little variation in peak positions. Overall, replicate agreement is good.

S3. Structural Analysis

Overlays of XAFS and PDF data show progressive changes to short and intermediate range structure (Figure S **31** and Figure S **32**, respectively).

S4. Component Analysis

Additional fits for the PACC series with different end-members are shown in Figure S **33**. The plots include the calculated RMSE for y-error bars.

Table S 5. Compositions of PACC series used to constrain X-ray total scattering data processing calculated from TGA-DSC data and LCF results.

	Composition					Parameter Estimates			
% PO4	H	C	O	P	Ca	ACP	n(H_2O)	ACC	n(H_2O)
0.5	3.34	0.98	4.78	0.04	1.04	0.0214	4.45	0.9786	1.61
1	3.51	0.95	5.01	0.10	1.10	0.0508	4.45	0.9492	1.61
2	3.64	0.93	5.19	0.15	1.15	0.0737	4.45	0.9263	1.61
6	4.28	0.81	6.07	0.37	1.37	0.1862	4.45	0.8138	1.61
10	4.98	0.69	7.04	0.62	1.62	0.3103	4.45	0.6897	1.61
30	7.77	0.20	10.88	1.60	2.60	0.8002	4.45	0.1998	1.61
50	8.63	0.05	12.08	1.91	2.91	0.9527	4.45	0.0473	1.61
70	8.79	0.02	12.29	1.96	2.96	0.9800	4.45	0.0200	1.61

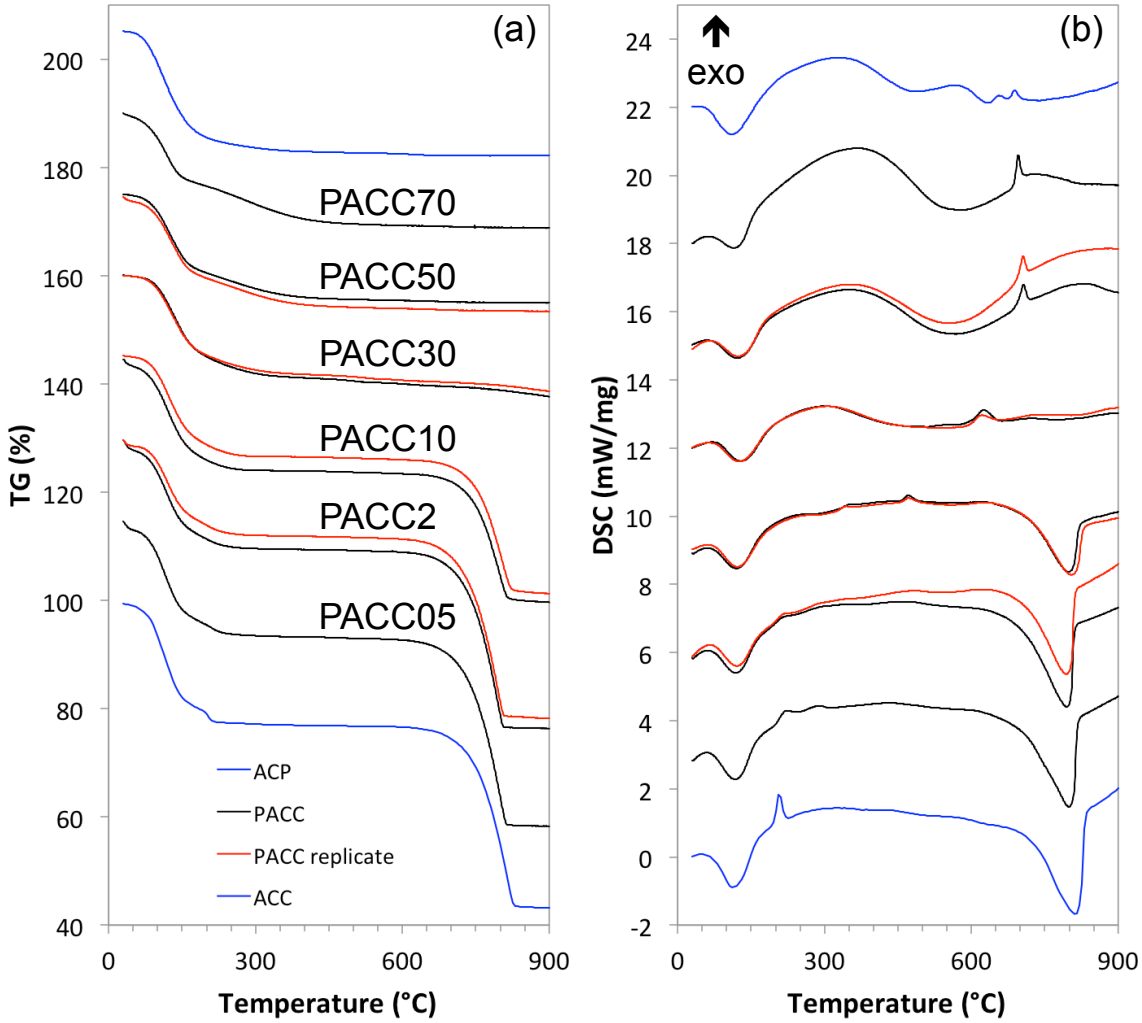

Figure S 30. Thermal analysis of PACC series showing (a) TG with arbitrary 20% offsets along the y-axis and (b) DSC with arbitrary 3 mW/mg offsets along the y-axis. Red traces are replicate analyses.

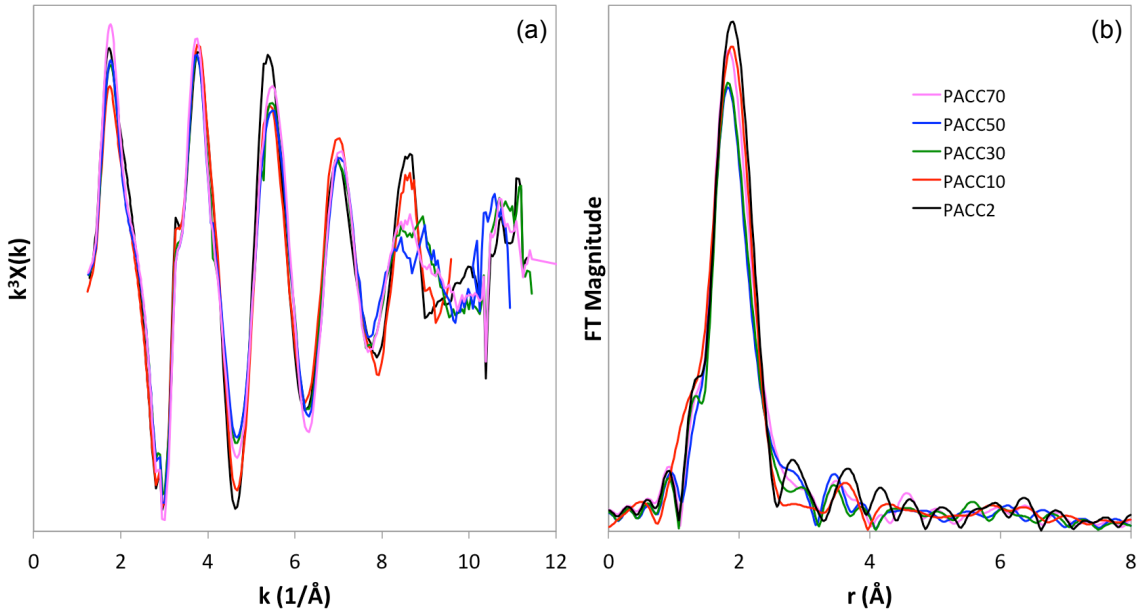

Figure S 31. Overlays of PACC series XAFS data showing (a) χ(k) with a k-weighting of 3 and (b) the Fourier transform magnitude.

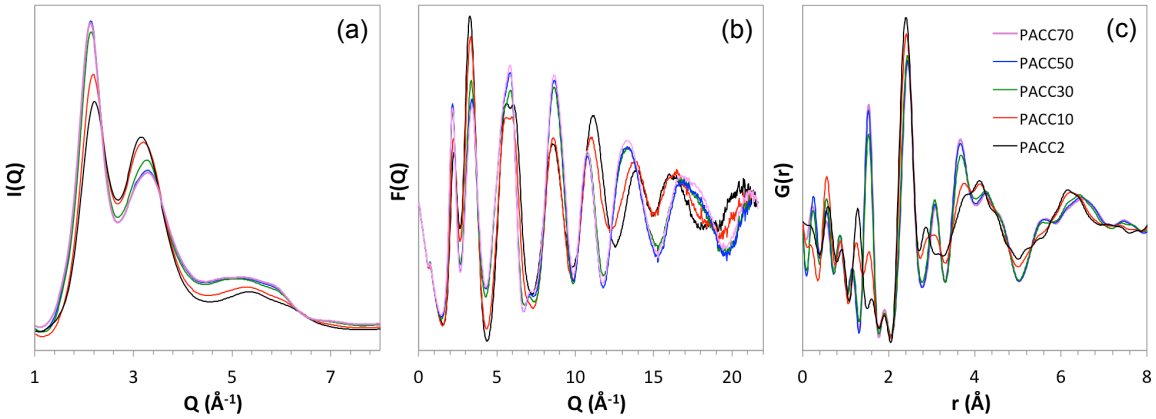

Figure S 32. Overlay comparison of PACC series (a) I(Q), (b) F(Q), and (c) G(r).

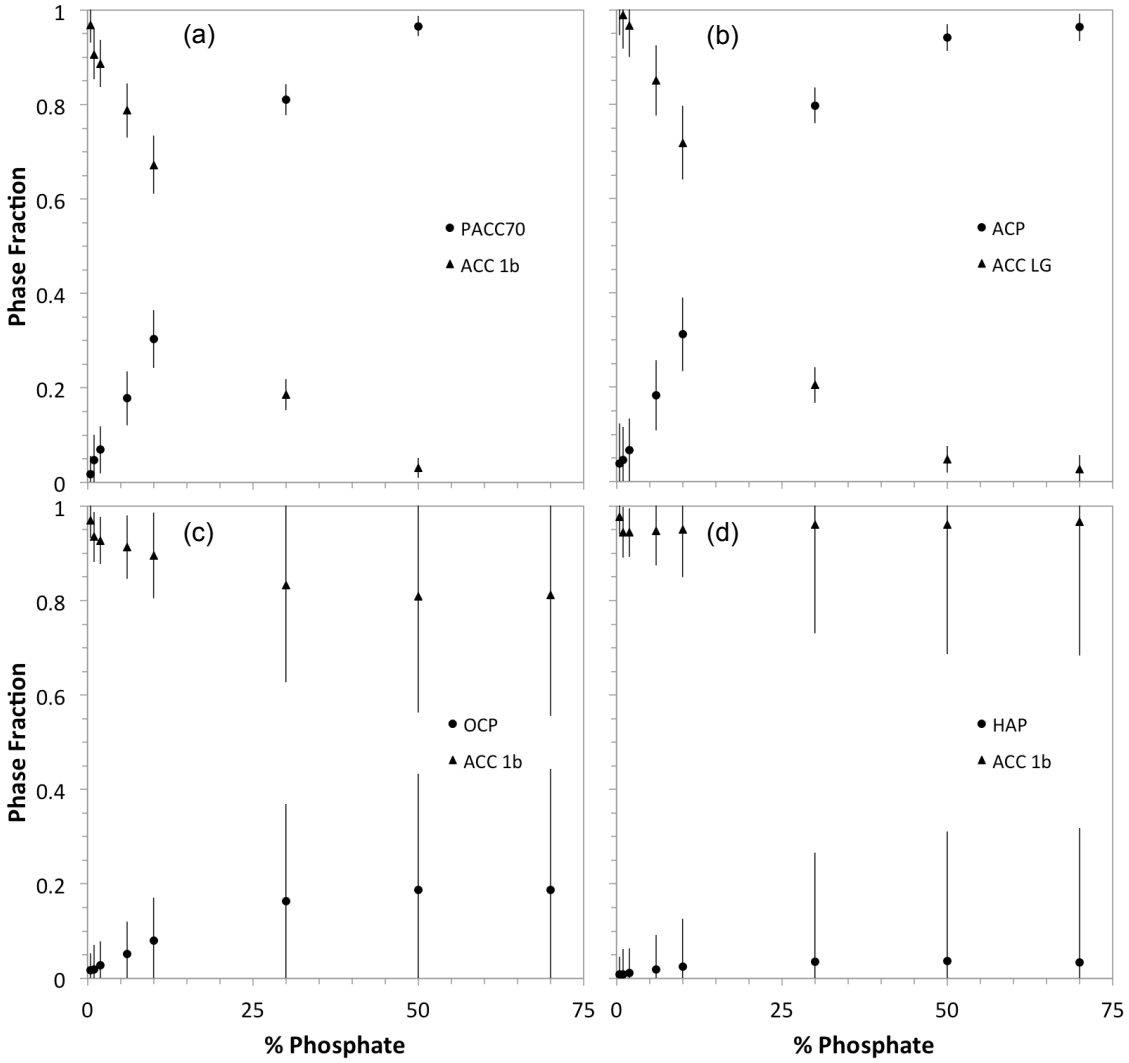

Figure S 33. LCF results plotted versus % phosphate in synthesis solution for various phosphate and carbonate end-members, (a) PACC70 and ACC 1b, (b) ACP and ACC LG, (c) OCP and ACC 1b, and (d) HAP and ACC 1b.

References

(1) Addadi, L.; Raz, S.; Weiner, S., *Advanced Materials* **2003,** 15, (12), 959-970.
(2) Kimura, T.; Koga, N., *Crystal Growth & Design* **2011,** 11, (9), 3877-3884.
(3) Weiner, S.; Levi-Kalisman, Y.; Raz, S.; Addadi, L., *Connect Tissue Res* **2003,** 44, 214-218.
(4) Cartwright, J. H. E.; Checa, A. G.; Gale, J. D.; Gebauer, D.; Sainz-Diaz, C. I., *Angewandte Chemie-International Edition* **2012,** 51, (48), 11960-11970.
(5) Weiner, S., *Bone* **2006,** 39, (3), 431-433.
(6) Weiner, S.; Sagi, I.; Addadi, L., *Science* **2005,** 309, (5737), 1027-1028.
(7) Weiss, I. M.; Tuross, N.; Addadi, L.; Weiner, S., *Journal of Experimental Zoology* **2002,** 293, (5), 478-491.
(8) Wolf, S. E.; Leiterer, J.; Kappl, M.; Emmerling, F.; Tremel, W., *Journal of the American Chemical Society* **2008,** 130, (37), 12342-12347.
(9) Posner, A. S.; Betts, F., *Accounts of Chemical Research* **1975,** 8, (8), 273-281.
(10) Mahamid, J.; Sharir, A.; Addadi, L.; Weiner, S., *Proceedings of the National Academy of Sciences of the United States of America* **2008,** 105, (35), 12748-12753.
(11) Akiva-Tal, A.; Kababya, S.; Balazs, Y. S.; Glazer, L.; Berman, A.; Sagi, A.; Schmidt, A., *Proceedings of the National Academy of Sciences of the United States of America* **2011,** 108, (36), 14763-14768.
(12) Gal, A.; Habraken, W.; Gur, D.; Fratzl, P.; Weiner, S.; Addadi, L., *Angewandte Chemie-International Edition* **2013,** 52, (18), 4867-4870.
(13) Neues, F.; Hild, S.; Epple, M.; Marti, O.; Ziegler, A., *J Struct Biol* **2011,** 175, (1), 10-20.
(14) Islam, K. N.; Bin Abu Bakar, M. Z.; Noordin, M. M.; Bin Hussein, M. Z.; Abd Rahman, N. S. B.; Ali, M. E., *Powder Technology* **2011,** 213, (1-3), 188-191.
(15) Shechter, A.; Berman, A.; Singer, A.; Freiman, A.; Grinstein, M.; Erez, J.; Aflalo, E. D.; Sagi, A., *Biol Bull* **2008,** 214, (2), 122-134.
(16) Raz, S.; Testeniere, O.; Hecker, A.; Weiner, S.; Luquet, G., *Biol Bull* **2002,** 203, (3), 269-274.
(17) Hild, S.; Marti, O.; Ziegler, A., *J Struct Biol* **2008,** 163, (1), 100-108.
(18) Gal, A.; Hirsch, A.; Siegel, S.; Li, C.; Aichmayer, B.; Politi, Y.; Fratzl, P.; Weiner, S.; Addadi, L., *Chemistry-a European Journal* **2012,** 18, (33), 10262-10270.
(19) Politi, Y.; Metzler, R. A.; Abrecht, M.; Gilbert, B.; Wilt, F. H.; Sagi, I.; Addadi, L.; Weiner, S.; Gilbert, P., *Proceedings of the National Academy of Sciences of the United States of America* **2008,** 105, (45), 17362-17366.
(20) Raz, S.; Hamilton, P. C.; Wilt, F. H.; Weiner, S.; Addadi, L., *Advanced Functional Materials* **2003,** 13, (6), 480-486.
(21) Reeder, R. J.; Tang, Y.; Schmidt, M. P.; Kubista, L. M.; Cowan, D. F.; Phillips, B. L., *Crystal Growth & Design* **2013,** 13, 1905-1914.
(22) Levi-Kalisman, Y.; Raz, S.; Weiner, S.; Addadi, L.; Sagi, I., *Journal of the Chemical Society-Dalton Transactions* **2000**, (21), 3977-3982.
(23) Levi-Kalisman, Y.; Raz, S.; Weiner, S.; Addadi, L.; Sagi, I., *Advanced Functional Materials* **2002,** 12, (1), 43-48.

(24) Radha, A. V.; Forbes, T. Z.; Killian, C. E.; Gilbert, P. U. P. A.; Navrotsky, A., *Proceedings of the National Academy of Sciences of the United States of America* **2010,** 107, (38), 16438-16443.
(25) Koga, N.; Nakagoe, Y. Z.; Tanaka, H., *Thermochimica Acta* **1998,** 318, (1-2), 239-244.
(26) Faatz, M.; Grohn, F.; Wegner, G., *Advanced Materials* **2004,** 16, (12), 996-1000.
(27) Huang, F. Z.; Shen, Y. H.; Xie, A. J.; Zhang, X. Z.; Cai, Y.; Wu, W. T., *Crystal Research and Technology* **2009,** 44, (8), 818-822.
(28) Xu, G. F.; Yao, N.; Aksay, I. A.; Groves, J. T., *Journal of the American Chemical Society* **1998,** 120, (46), 11977-11985.
(29) Michel, F. M.; MacDonald, J.; Feng, J.; Phillips, B. L.; Ehm, L.; Tarabrella, C.; Parise, J. B.; Reeder, R. J., *Chemistry of Materials* **2008,** 20, (14), 4720-4728.
(30) Goodwin, A. L.; Michel, F. M.; Phillips, B. L.; Keen, D. A.; Dove, M. T.; Reeder, R. J., *Chemistry of Materials* **2010,** 22, (10), 3197-3205.
(31) Nebel, H.; Neumann, M.; Mayer, C.; Epple, M., *Inorg Chem* **2008,** 47, (17), 7874-7879.
(32) Rez, P.; Blackwell, A., *J. Phys. Chem. B* **2011,** 115, (38), 11193-11198.
(33) Singer, J. W.; Yazaydin, A. O.; Kirkpatrick, R. J.; Bowers, G. M., *Chemistry of Materials* **2012,** 24, (10), 1828-1836.
(34) Gebauer, D.; Voelkel, A.; Coelfen, H., *Science* **2008,** 322, (5909), 1819-1822.
(35) Gebauer, D.; Gunawidjaja, P. N.; Ko, J. Y. P.; Bacsik, Z.; Aziz, B.; Liu, L.; Hu, Y.; Bergstrom, L.; Tai, C.-W.; Sham, T.-K.; Eden, M.; Hedin, N., *Angewandte Chemie-International Edition* **2010,** 49, (47), 8889-8891.
(36) Tester, C. C.; Wu, C.-H.; Krejci, M. R.; Meuller, L.; Park, A.; Lai, B.; Chen, S.; Sun, C.; Balasubramanian, M.; Joester, D., *Advanced Functional Materials* **2013,** 23, 4185-4194.
(37) Becker, A.; Ziegler, A.; Epple, M., *Dalton Transactions* **2005**, (10), 1814-1820.
(38) Vidavsky, N.; Addadi, S.; Mahamid, J.; Shimoni, E.; Ben-Ezra, D.; Shpigel, M.; Weiner, S.; Addadi, L., *Proceedings of the National Academy of Sciences of the United States of America* **2014,** 111, (1), 39-44.
(39) Al-Sawalmih, A.; Li, C.; Siegel, S.; Fratzl, P.; Paris, O., *Advanced Materials* **2009,** 21, (40), 4011-4015.
(40) Politi, Y.; Batchelor, D. R.; Zaslansky, P.; Chmelka, B. F.; Weaver, J. C.; Sagi, I.; Weiner, S.; Addadi, L., *Chemistry of Materials* **2010,** 22, (1), 161-166.
(41) Radha, A. V.; Fernandez-Martinez, A.; Hu, Y. D.; Jun, Y. S.; Waychunas, G. A.; Navrotsky, A., *Geochim. Cosmochim. Acta* **2012,** 90, 83-95.
(42) Wang, D. B.; Hamm, L. M.; Bodnar, R. J.; Dove, P. M., *Journal of Raman Spectroscopy* **2012,** 43, (4), 543-548.
(43) Jiang, J.; Gao, M.-R.; Qiu, Y.-H.; Yu, S.-H., *Nanoscale* **2010,** 2, (11), 2358-2361.
(44) Sugiura, Y.; Onuma, K.; Kimura, Y.; Tsukamoto, K.; Yamazaki, A., *American Mineralogist* **2013,** 98, (1), 262-270.
(45) Tomono, H.; Nada, H.; Zhu, F. J.; Sakamoto, T.; Nishimura, T.; Kato, T., *J. Phys. Chem. B* **2013,** 117, (47), 14849-14856.
(46) Ishii, K.; Tsutsui, N.; Watanabe, T.; Yanagisawa, T.; Nagasawa, H., *Bioscience Biotechnology and Biochemistry* **1998,** 62, (2), 291-296.
(47) Shechter, A.; Glazer, L.; Cheled, S.; Mor, E.; Weil, S.; Berman, A.; Bentov, S.; Aflalo, E. D.; Khalaila, I.; Sagi, A., *Proceedings of the National Academy of Sciences of the United States of America* **2008,** 105, (20), 7129-7134.

(48) Glazer, L.; Shechter, A.; Tom, M.; Yudkovski, Y.; Weil, S.; Aflalo, E. D.; Pamuru, R. R.; Khalaila, I.; Bentov, S.; Berman, A.; Sagi, A., *J Biol Chem* **2010,** 285, (17), 12831-12839.
(49) Aizenberg, J.; Lambert, G.; Addadi, L.; Weiner, S., *Advanced Materials* **1996,** 8, (3), 222-226.
(50) Sato, A.; Nagasaka, S.; Furihata, K.; Nagata, S.; Arai, I.; Saruwatari, K.; Kogure, T.; Sakuda, S.; Nagasawa, H., *Nature Chemical Biology* **2011,** 7, (4), 197-199.
(51) Raabe, D.; Romano, P.; Sachs, C.; Fabritius, H.; Al-Sawalmih, A.; Yi, S.; Servos, G.; Hartwig, H. G., *Mater. Sci. Eng. A-Struct. Mater. Prop. Microstruct. Process.* **2006,** 421, (1-2), 143-153.
(52) Al-Sawalmih, A.; Li, C. H.; Siegel, S.; Fabritius, H.; Yi, S. B.; Raabe, D.; Fratzl, P.; Paris, O., *Advanced Functional Materials* **2008,** 18, (20), 3307-3314.
(53) Wang, S. S.; Xu, A. W., *Crystal Growth & Design* **2013,** 13, (5), 1937-1942.
(54) Liu, Y.; Cui, Y. J.; Guo, R., *Langmuir* **2012,** 28, (14), 6097-6105.
(55) Gorna, K.; Munoz-Espi, R.; Groehn, F.; Wegner, G., *Macromolecular Bioscience* **2007,** 7, (2), 163-173.
(56) Xu, A. W.; Dong, W. F.; Antonietti, M.; Colfen, H., *Advanced Functional Materials* **2008,** 18, (8), 1307-1313.
(57) Huang, S.-C.; Naka, K.; Chujo, Y., *Langmuir* **2007,** 23, (24), 12086-12095.
(58) Wei, H.; SHen, Q.; Zhao, Y.; Wang, D.-J.; Duan-Fu, X., *Journal of Crystal Growth* **2003,** 250, 516-524.
(59) Wolf, S. E.; Leiterer, J.; Pipich, V.; Barrea, R.; Emmerling, F.; Tremel, W., *Journal of the American Chemical Society* **2011,** 133, (32), 12642-12649.
(60) He, L. H.; Yao, L.; Sun, J.; Wu, W.; Yang, J.; Cai, L. F.; Song, R.; Hao, Y. M.; Ma, Z.; Huang, W., *Polymer Degradation and Stability* **2011,** 96, (7), 1187-1193.
(61) Tester, C. C.; Brock, R. E.; Wu, C. H.; Krejci, M. R.; Weigand, S.; Joester, D., *Crystengcomm* **2011,** 13, (12), 3975-3978.
(62) Bentov, S.; Weil, S.; Glazer, L.; Sagi, A.; Berman, A., *J Struct Biol* **2010,** 171, (2), 207-215.
(63) Cai, G.-B.; Chen, S.-F.; Liu, L.; Jiang, J.; Yao, H.-B.; Xu, A.-W.; Yu, S.-H., *Crystengcomm* **2010,** 12, (1), 234-241.
(64) Tao, J. H.; Zhou, D. M.; Zhang, Z. S.; Xu, X. R.; Tang, R. K., *Proceedings of the National Academy of Sciences of the United States of America* **2009,** 106, (52), 22096-22101.
(65) Gunther, C.; Becker, A.; Wolf, G.; Epple, M., *Zeitschrift Fur Anorganische Und Allgemeine Chemie* **2005,** 631, (13-14), 2830-2835.
(66) Kato, T.; Sugawara, A.; Hosoda, N., *Advanced Materials* **2002,** 14, (12), 869-877.
(67) Xu, X. R.; Han, J. T.; Cho, K., *Chemistry of Materials* **2004,** 16, (9), 1740-1746.
(68) Xu, X.; Han, J. T.; Kim, D. H.; Cho, K., *J. Phys. Chem. B* **2006,** 110, (6), 2764-2770.
(69) Lee, K.; Wagermaier, W.; Masic, A.; Kommareddy, K. P.; Bennet, M.; Manjubala, I.; Lee, S. W.; Park, S. B.; Colfen, H.; Fratzl, P., *Nature Communications* **2012,** 3, (725), 1-7.
(70) Li, C.; Hong, G.; Yu, H.; Qi, L., *Chemistry of Materials* **2010,** 22, (10), 3206-3211.
(71) Shen, Q.; Wei, H.; Zhou, Y.; Huang, Y. P.; Yang, H. R.; Wang, D. J.; Xu, D. F., *J. Phys. Chem. B* **2006,** 110, (7), 2994-3000.
(72) Naka, K.; Chujo, Y., *Chemistry of Materials* **2001,** 13, (10), 3245-3259.
(73) Meldrum, F. C.; Ludwigs, S., *Macromolecular Bioscience* **2007,** 7, (2), 152-162.
(74) Yeom, B.; Char, K., *Chemistry of Materials* **2010,** 22, (1), 101-107.

(75) Colfen, H.; Antonietti, M., *Angewandte Chemie-International Edition* **2005,** 44, (35), 5576-5591.
(76) Ihli, J.; Kim, Y. Y.; Noel, E. H.; Meldrum, F. C., *Advanced Functional Materials* **2013,** 23, (12), 1575-1585.
(77) Xu, X.-R.; Cai, A.-H.; Liu, R.; Pan, H.-H.; Tang, R.-K.; Cho, K., *Journal of Crystal Growth* **2008,** 310, (16), 3779-3787.
(78) Gong, Y. U. T.; Killian, C. E.; Olson, I. C.; Appathurai, N. P.; Amasino, A. L.; Martin, M. C.; Holt, L. J.; Wilt, F. H.; Gilbert, P. U. P. A., *Proceedings of the National Academy of Sciences of the United States of America* **2012,** 109, (16), 6088-6093.
(79) Bots, P.; Benning, L. G.; Rodriguez-Blanco, J. D.; Roncal-Herrero, T.; Shaw, S., *Crystal Growth & Design* **2012,** 12, (7), 3806-3814.
(80) Saharay, M.; Kirkpatrick, R. J., *Chem Phys Lett* **2014,** 591, 287-291.
(81) Saharay, M.; Yazaydin, A. O.; Kirkpatrick, R. J., *J. Phys. Chem. B* **2013,** 117, (12), 3328-3336.
(82) Raiteri, P.; Gale, J. D., *Journal of the American Chemical Society* **2010,** 132, (49), 17623-17634.
(83) Koga, N.; Yamane, Y.; Kimura, T., *Thermochimica Acta* **2011,** 512, (1-2), 13-21.
(84) Tang, H.; Yu, J.; Zhao, X., *Materials Research Bulletin* **2009,** 44, (4), 831-835.
(85) Xiao, J.; Yang, S., *Crystengcomm* **2011,** 13, (20), 6223-6230.
(86) Wang, D. B.; Wallace, A. F.; De Yoreo, J. J.; Dove, P. M., *Proceedings of the National Academy of Sciences of the United States of America* **2009,** 106, (51), 21511-21516.
(87) Wang, Y. W.; Kim, Y. Y.; Stephens, C. J.; Meldrum, F. C.; Christenson, H. K., *Crystal Growth & Design* **2012,** 12, (3), 1212-1217.
(88) Stephens, C. J.; Ladden, S. F.; Meldrum, F. C.; Christenson, H. K., *Advanced Functional Materials* **2010,** 20, (13), 2108-2115.
(89) Lee, H. S.; Ha, T. H.; Kim, K., *Materials Chemistry and Physics* **2005,** 93, (2-3), 376-382.
(90) Koga, N.; Yamane, Y., *Journal of Thermal Analysis and Calorimetry* **2008,** 94, (2), 379-387.
(91) Gebauer, D.; Coelfen, H.; Verch, A.; Antonietti, M., *Advanced Materials* **2009,** 21, (4), 435-439.
(92) Pontoni, D.; Bolze, J.; Dingenouts, N.; Narayanan, T.; Ballauff, M., *J. Phys. Chem. B* **2003,** 107, (22), 5123-5125.
(93) Rodriguez-Blanco, J. D.; Shaw, S.; Benning, L. G., *Nanoscale* **2011,** 3, (1), 265-271.
(94) Xiao, J. W.; Wang, Z. N.; Tang, Y. C.; Yang, S. H., *Langmuir* **2010,** 26, (7), 4977-4983.
(95) Ogino, T.; Suzuki, T.; Sawada, K., *Geochim. Cosmochim. Acta* **1987,** 51, (10), 2757-2767.
(96) Fernandez-Martinez, A.; Kalkan, B.; Clark, S. M.; Waychunas, G. A., *Angewandte Chemie-International Edition* **2013,** 52, (32), 8354-8357.
(97) Yoshino, T.; Maruyama, K.; Kagi, H.; Nara, M.; Kim, J. C., *Crystal Growth & Design* **2012,** 12, (7), 3357-3361.
(98) Zhang, Z.; Xie, Y.; Xu, X.; Pan, H.; Tang, R., *Journal of Crystal Growth* **2012,** 343, 62-67.
(99) Xie, Y.; Xu, X.; Tang, R., *Science China-Chemistry* **2010,** 53, (10), 2208-2214.
(100) Sawada, K., *Pure Appl. Chem.* **1997,** 69, (5), 921-928.
(101) Dai, L.; Cheng, X.; Gower, L. B., *Chemistry of Materials* **2008,** 20, (22), 6917-6928.
(102) Li, M.; Mann, S., *Advanced Functional Materials* **2002,** 12, (11-12), 773-779.

(103) Fernandez-Diaz, L.; Pina, C. M.; Astilleros, J. M.; Sanchez-Pastor, N., *American Mineralogist* **2009,** 94, (8-9), 1223-1234.
(104) Meiron, O. E.; Bar-David, E.; Aflalo, E. D.; Shechter, A.; Stepensky, D.; Berman, A.; Sagi, A., *J Bone Miner Res* **2011,** 26, (2), 364-372.
(105) Combes, C.; Rey, C., *Acta Biomaterialia* **2010,** 6, (9), 3362-3378.
(106) Zhao, J.; Liu, Y.; Sun, W. B.; Yang, X. B., *Journal of Dental Sciences* **2012,** 7, (4), 316-323.
(107) Grover, L. M.; Wright, A. J.; Gbureck, U.; Bolarinwa, A.; Song, J. F.; Liu, Y.; Farrar, D. F.; Howling, G.; Rose, J.; Barralet, J. E., *Biomaterials* **2013,** 34, (28), 6631-6637.
(108) Melo, M. A. S.; Chenga, L.; Zhanga, K.; Weir, M. D.; Rodrigues, L. K. A.; Xu, H. H. K., *Dental Materials* **2013,** 29, (2), 199-210.
(109) Melo, M. A. S.; Weir, M. D.; Rodrigues, L. K. A.; Xu, H. H. K., *Dental Materials* **2013,** 29, (2), 231-240.
(110) Saber-Samandari, S.; Gross, K. A., *Acta Biomaterialia* **2011,** 7, (12), 4235-4241.
(111) Killian, C. E.; Metzler, R. A.; Gong, Y. U. T.; Olson, I. C.; Aizenberg, J.; Politi, Y.; Wilt, F. H.; Scholl, A.; Young, A.; Doran, A.; Kunz, M.; Tamura, N.; Coppersmith, S. N.; Gilbert, P. U. P. A., *Journal of the American Chemical Society* **2009,** 131, (51), 18404-18409.
(112) Lam, R. S. K.; Charnock, J. M.; Lennie, A.; Meldrum, F. C., *Crystengcomm* **2007,** 9, (12), 1226-1236.
(113) Kojima, Y.; Kanai, M.; Nishimiya, N., *Ultrason Sonochem* **2012,** 19, (2), 325-329.
(114) Proffen, T.; Page, K. L., *Zeitschrift Fur Kristallographie* **2004,** 219, (3), 130-135.
(115) Hammersley, A. P.; Svensson, S. O.; Hanfland, M.; Fitch, A. N.; Hausermann, D., *High Pressure Research* **1996,** 14, (4-6), 235-248.
(116) Qiu, X. Y.; Bozin, E. S.; Juhas, P.; Proffen, T.; Billinge, S. J. L., *Journal of Applied Crystallography* **2004,** 37, 110-116.
(117) Chupas, P. J.; Qiu, X. Y.; Hanson, J. C.; Lee, P. L.; Grey, C. P.; Billinge, S. J. L., *Journal of Applied Crystallography* **2003,** 36, 1342-1347.
(118) Fulton, J. L.; Chen, Y.; Heald, S. M.; Balasubramanian, M., *Journal of Chemical Physics* **2006,** 125, (9), 4688-4696.
(119) Egami, T.; Billinge, S. J. L., *Underneath the Bragg Peaks: Structural Analysis of Complex Materials*. ed.; Pergamon: 2003; p 404.
(120) B.L., H.; E.M., G.; J.C., D., *Atomic Data and Nuclear Data Tables* **1993,** 54, 181-342.
(121) Massiot, D.; Fayon, F.; Capron, M.; King, I.; Le Calve, S.; Alonso, B.; Durand, J. O.; Bujoli, B.; Gan, Z. H.; Hoatson, G., *Magn Reson Chem* **2002,** 40, (1), 70-76.
(122) Politi, Y.; Levi-Kalisman, Y.; Raz, S.; Wilt, F.; Addadi, L.; Weiner, S.; Sagi, I., *Advanced Functional Materials* **2006,** 16, (10), 1289-1298.
(123) Killian, C. E.; Metzler, R. A.; Gong, Y. U. T.; Olson, I. C.; Aizenberg, J.; Politi, Y.; Wilt, F. H.; Scholl, A.; Young, A.; Doran, A.; Kunz, M.; Tamura, N.; Coppersmith, S. N.; Gilbert, P., *Journal of the American Chemical Society* **2009,** 131, (51), 18404-18409.
(124) Colfen, H.; Mann, S., *Angewandte Chemie-International Edition* **2003,** 42, (21), 2350-2365.
(125) Schmidt, M. P.; Ilott, A. J.; Phillips, B. L.; Reeder, R. J., *Crystal Growth & Design* **2014,** 14, (3), 938-951.
(126) Cai, A.; Xu, X.; Pan, H.; Tao, J.; Liu, R.; Tang, R.; Cho, K., *Journal of Physical Chemistry C* **2008,** 112, (30), 11324-11330.
(127) Chaplin, M. F., *Biophysical Chemistry* **1999,** 83, 211-221.

(128) Toby, B. H.; Egami, T., *Acta Crystallographica Section A* **1992,** 48, 336-346.
(129) Rodriguez-Blanco, J. D.; Bots, P.; Terrill, N. J.; Shaw, S.; Benning, L. G., *Geochim. Cosmochim. Acta* **2010,** 74, (12).
(130) Spanos, N.; Koutsoukos, P. G., *Journal of Crystal Growth* **1998,** 191, 783-790.
(131) Katsifaras, A.; Spanos, N., *Journal of Crystal Growth* **1999,** 204, 183-190.
(132) Malek, J., *Thermochimica Acta* **1995,** 267, 61-73.
(133) Malek, J., *Thermochimica Acta* **2000,** 355, (1-2), 239-253.
(134) Malek, J.; Mitsuhashi, T., *Journal of the American Ceramic Society* **2000,** 83, (8), 2103-2105.
(135) Dorvee, J. R.; Veis, A., *J Struct Biol* **2013,** 183, (2), 278-303.
(136) Hasse, B.; Ehrenberg, H.; Marxen, J. C.; Becker, W.; Epple, M., *Chemistry-a European Journal* **2000,** 6, (20), 3679-3685.
(137) Luquet, G.; Marin, F., *Comptes Rendus Palevol* **2004,** 3, (6-7), 515-534.
(138) Koll, P.; Borchers, G.; Metzger, J. O., *Journal of Analytical and Applied Pyrolysis* **1991,** 19, 119-129.
(139) Betts, F.; Blumenthal, N. C.; Posner, A. S.; Becker, G. L.; Lehninger, A. L., *Proceedings of the National Academy of Sciences of the United States of America* **1975,** 72, (6), 2088-2090.
(140) Noel, E. H.; Kim, Y. Y.; Charnock, J. M.; Meldrum, F. C., *Crystengcomm* **2013,** 15, (4), 697-705.
(141) Verch, A.; Morrison, I. E. G.; van de Locht, R.; Kroger, R., *J Struct Biol* **2013,** 183, (2), 270-277.
(142) Du, L. W.; Bian, S.; Gou, B. D.; Jiang, Y.; Huang, J.; Gao, Y. X.; Zhao, Y. D.; Wen, W.; Zhang, T. L.; Wang, K., *Crystal Growth & Design* **2013,** 13, (7), 3103-3109.
(143) Dorozhkin, S. V., *Acta Biomaterialia* **2010,** 6, (12), 4457-4475.
(144) Meyer, J. L.; Eanes, E. D., *Calcified Tissue Research* **1978,** 25, (1), 59-68.
(145) Astala, R.; Stott, M. J., *Chemistry of Materials* **2005,** 17, (16), 4125-4133.
(146) Eliassi, M. D.; Zhao, W.; Tan, W. F., *Materials Research Bulletin* **2014,** 55, 114-120.
(147) Fulton, J. L.; Heald, S. M.; Badyal, Y. S.; Suimonson, J. M., *J. Phys. Chem. A* **2003,** 107, (23), 4688-4696.
(148) Abbona, F.; Baronnet, A., *Journal of Crystal Growth* **1996,** 165, (1-2), 98-105.
(149) Rabadjieva, D.; Gergulova, R.; Titorenkova, R.; Tepavitcharova, S.; Dyulgerova, E.; Balarew, C.; Petrov, O., *Journal of Materials Science-Materials in Medicine* **2010,** 21, (9), 2501-2509.
(150) Pan, H. H.; Liu, X. Y.; Tang, R. K.; Xu, H. Y., *Chemical Communications* **2010,** 46, (39), 7415-7420.
(151) Morse, J. W., *Am. J. Sci.* **1974,** 274, (6), 638-647.
(152) Stoessell, R. K.; Moor, Y. H.; Coke, J. G., *Groundwater* **1993,** 31, (4), 566-575.
(153) Sariibrahimoglu, K.; Leeuwenburgh, S. C. G.; Wolke, J. G. C.; Li, Y. B.; Jansen, J. A., *Journal of Biomedical Materials Research Part A* **2012,** 100A, (3), 712-719.